CHALMERS

FE-modeling and validation of a washing machine

Using experimental modal analysis and spin up test

Master's Thesis in the Master's programme Solid and Fluid Mechanics

TOBIAS ANDERSSON

TOBIAS HANSSON

Department of Applied Mechanics
Division of Dynamics
CHALMERS UNIVERSITY OF TECHNOLOGY
Göteborg, Sweden 2009
Master's Thesis 2009:09

MASTER'S THESIS 2009:09

FE-modeling and validation of a washing machine

Using experimental modal analysis and spin up test

Master's Thesis in the Master's programme Solid and Fluid Mechanics

TOBIAS ANDERSSON

TOBIAS HANSSON

Department of Applied Mechanics
Division of Dynamics
CHALMERS UNIVERSITY OF TECHNOLOGY
Göteborg, Sweden 2009

FE-modeling and validation of a washing machine
Using experimental modal analysis and spin up test
Master's Thesis in the Master's programme Solid and Fluid Mechanics

TOBIAS ANDERSSON
TOBIAS HANSSON

Master's Thesis 2009:09
ISSN 1652-8557
Department of Applied Mechanics
Division of Dynamics
Chalmers University of Technology
SE-412 96 Göteborg
Sweden
Telephone: + 46 (0)31-772 1000

Cover:
An ASKO Appliances AB washing machine with an artistic view of a finite element mesh.

Chalmers Reproservice
Göteborg, Sweden 2009

FE-modeling and validation of a washing machine
Using experimental modal analysis and spin up test
Master's Thesis in the Master's programme Solid and Fluid Mechanics
TOBIAS ANDERSSON and TOBIAS HANSSON
Department of Applied Mechanics
Division of Dynamics
Chalmers University of Technology

ABSTRACT

In this master thesis the dynamics in the steel shell of a washing machine from ASKO Appliances AB has been studied. The thesis is the third in a series where the first studied the behavior of a side plate and the second studied the dynamics in half of the steel shell parts. In this work all parts are first studied separate and then assembled to the steel shell. Additionally a model will be made of the parts needed to simulate the spin up of a washing machine. The goal of the thesis work is to make a model of the steel shell that correlates well with the real steel shell and to be able to simulate the forces and accelerations in the shell that arises from a spin up in the drum of the washing machine.

Every detail has been modeled using finite elements and validated using experimental modal analysis. The parts already studied will also be modeled in order to match the results from the previous year's thesis works. The results show that each separate part correlates well in most modes when comparing mode shapes, eigenfrequencies and frequency response functions.

The models are assembled into the steel shell and validated in the same manner as each separate part. The result from these studies shows that a good correlation is obtained in the steel shell up to about 60 Hz. Above that, the mode shapes are getting more complex and harder to correlate. There are some differences in eigenfrequencies between the model and the real steel shell. The problem with the side plate correlation of previous thesis works have been found to have minor importance when the steel shell had been fully assembled.

The model used to calculate accelerations and forces in the machine during rotation of an unbalanced loaded drum showed a rather poor correlation. The reason is that higher order harmonics have more impact on the vibrations in the shell than first thought. The forces under the feet and the accelerations in the side plate were the results that matched the measured data best.

Key words: Washing machine, steel shell, dynamics, experimental modal analysis, EMA, finite element method, FEM, FE-model, spin up, spin up test.

FE-modellering och validering av en tvättmaskin
Med hjälp av experimentell modanalys och körtest
Examensarbete inom magisterprogrammet Solid and Fluid Dynamics
TOBIAS ANDERSSON och TOBIAS HANSSON
Institutionen för tillämpad mekanik
Avdelningen för dynamik
Chalmers tekniska högskola

SAMMANFATTNING

I detta examensarbete studeras dynamiken i plåtskalet till en tvättmaskin från ASKO Appliances AB. Examensarbetet är det tredje i en serie, där första arbetet undersökte dynamiken i en sidoplåt och det andra studerade dynamiken i hälften av delarna i plåtskalet var för sig och sammansatta. I detta arbete beaktas alla separata delar i plåtskalet, det sammansatta plåtskalet samt de delar som behövs för att köra tvättmaskinen. Målet med examensarbetet är att lyckas få en modell av skalet som överensstämmer med det verkliga skalet samt att kunna simulera accelerationer i skal och krafter ifrån fötter på ett tillfredsställande sätt.

Varje detalj har modellerats med finita element och validerats med hjälp av experimentell modanalys. De delar som behandlas för första gången analyseras med experimentell modanalys medan för de övriga delarna används tidigare resultat. Delarna får bra överensstämmelse i de flesta av moderna vid en jämförelse mellan modform, resonansfrekvens samt frekvensresponsfunktion. Dessa modeller sätts samman för att skapa den sammansatta modellen som valideras med hjälp av experimentell modanalys.

Resultatet visar att när samtliga delar i skalet är sammansatta fås en god överensstämmelse mellan det modellerade och det verkliga skalets modformer upp till 60 Hz. Dock finns det fortfarande vissa skillnader i resonansfrekvenser. Problemet som har observerats i tidigare examensarbete med att sidoplåtarna visar sämre överensstämmelse har mindre betydelse i samband med att fler delar används i plåtskalet.

Modellen som användes för att jämföra accelerationer och krafter mot resultat från experiment, där rotation av trumman med obalans användes som excitering, visade en relativt dålig korrelation. Anledningen är att övertoner har en större betydelse för vibrationerna i skalet än först trott. De bästa resultaten erhölls för accelerationerna i sidosvepen och krafterna under fötterna.

Nyckelord: Tvättmaskin, plåtskal, dynamik, experiment, experimentell modanalys, EMA, finita elementmetoden, FEM, FE-Modell, körtest.

Contents

Preface

This Master's Thesis has been performed during the spring semester of year 2009 at the division of Dynamics, department of Applied Mechanics, Chalmers University of Technology, Sweden. The project is carried out on behalf of the company ASKO Appliances AB in Jung and is the third master thesis in a series of modeling shell parts and the shell of a washing machine for dynamic analysis.

We want to thank our supervisor and examiner at Chalmers professor Thomas Abrahamsson for the help and contribution to the thesis. We also want to thank Peder Bengtsson and Anders Eriksson our mentors at ASKO Appliances AB for their help with information and ideas. Last but not least we want to thank Lic. Eng. Thomas Nygårds for the help and contribution with the spin up experiments of the entire washing machine.

Göteborg 2009-06-08

Tobias Andersson
Tobias Hansson

Abbreviations

CAD	Computer Aided Design
E	Young's modulus [GPa]
EMA	Experimental Modal Analysis
FE-Model	Finite Element Model
FEM	Finite Element Method
Inside Parts	Term describing the parts not belonging to the shell, for example engine and drum
LDV	Laser-Doppler Vibrometer
MAC	Modal Assurance Criterion
MP	Measurement Point
ν	Poison's ratio
ρ	Density [kg/m^3]
RPM	Rotations Per Minute
Steel shell	Term describing the parts that make up the assembled washing machine shell
STEP	Standard for the Exchange of Product model data, a file format
t	Thickness [mm]
VXI	VME eXtensions for Instrumentation

1 Introduction

This report is the result of a master thesis project at the institution of Applied Mechanics at Chalmers University of technology. The project was performed on behalf of ASKO Appliances AB, a white goods manufacturer.

1.1 Background

On washing machines manufactured today there is a possibility to centrifuge the clothes with a rotation speed of up to 2000 rpm. In future models their goal is to use rotational speeds even higher than that. To understand what happens with the steel shell and what kind of vibrations these rotational speeds gives rise to, accurate models of the washing machine needs to be created.

In previous master thesis, one or several pieces from the steel shell have been used for FE-models and validation. These works showed that it is possible to get a rather well correlating model of the parts in the washing machine shell, but there still are some problems to the side plate model due to the manufacturing process that leaves residual stresses in it. This has caused problems when trying to validate the side plate models.

1.2 Problem statement

The side plates still cause problems when trying to validate a not yet fully assembled steel shell of the washing machine. Therefore a model of the complete steel shell will be created in order to evaluate the model's performance during spin up.

1.3 Purpose

The purpose of creating these models is to evaluate if the model of the steel shell will correlate better when using all parts in the assembly instead of half. It is also to evaluate the dynamical response in the washing machine shell when the machine is running.

For ASKO Appliances AB, the results can be a base for creating a method for analyzing and validating upcoming models.

1.4 Goal

The goal with the thesis work is to, within the timeframe of 20 weeks, be able to create and validate both a finite element model of the washing machine steel shell and a finite element model of the entire machine. The entire model will include the steel shell, inside parts, and the parts that connect the drum to the steel shell.

1.5 Delimitations

The steel shell model will consist of all metal parts in the shell except for the pump protection cover and the beam supporting the lid. The pump protection shell is assumed to have a small effect on the end result. The beam is removed because of the problems to use it in a linear

model since it is not fixed to the rest of the steel shell and because it is consisting of foam rubber which will be in contact with the lid.

No experiments will be performed on the pieces examined in previous master thesis. The results from these analyzes are assumed to be correct and finite element models will be created to match their results. The remaining shell parts are analyzed using experimental modal analysis and finite element modeling.

The inside parts of the washing machine will be created using few degrees of freedom. This since the goal with these parts is not to determine the exact structural behavior but have them transfer loads and structural couplings to the steel shell. The computational time is also of consideration. If the inner parts mesh is too fine, this time will grow too unmanageable lengths. This since the steel shell is very rich in details to properly capture the dynamic effects.

All parts are assumed to have isotropic properties and to be linear elastic. The CAD-files supplied from ASKO Appliances AB are assumed to be the correct models of the different parts and will be used as sources for the finite element models.

2 Method and theory

The methods used to analyze and validate the structure and different parts are described in this chapter. To see more about the specific test setup for each experiment, see chapter 4.

The FE-models have been created in the program Femap which is a pre- and post processing software to prepare FE-models of complicated geometries and to view analysis results. The geometries were provided by ASKO Appliances AB and were all of solid type. For all the steel shell parts, the thickness of the geometry was small in comparison to the length and width and those were modeled as shell elements (Niels & Petersson, 2000). Some of the inner parts were modeled as solid linear tetrahedral elements. For more information on how the parts were modeled see chapter 3.

Within this thesis work, two different types of experiments have been used. The first type of experiment is the one used in experimental modal analysis (EMA), where the separate parts and the fully assembled steel shell have been excited at different frequencies to determine the modal properties (mode shapes, natural frequencies and damping factors). The modal properties can then be used to confirm the validity of the FE-model of the studied structure (Craig Jr. & Kurdila, 2006).

In the second type of experiment, the excitation of the machine will be the drum rotating at different rotational speeds with an unbalance. This is done by computer control of the engine speed. The response is then measured in form of accelerations in the steel shell and the reaction forces under the feet of the washing machine. By comparing the calculated force and acceleration with the measured data, the model can be verified.

The general working process in the thesis can be seen in Figure 2-1.

Figure 2-1: The working process in the thesis work.

2.1 Modeled parts

ASKO Appliances AB has contributed with CAD-models for all parts that are included in the analysis. All CAD-models came as solid models in the file format STEP. The considered parts can be divided in two groups, those parts that the steel shell consists of and those on the inside of the steel shell, the inside parts, for example engine, drum etcetera. This can be seen in Figure 2-2.

When manufactured, these parts are made from rolled sheet metal. When rolling the metal, unevenly distributed internal stresses can occur. This will cause the sheet to deform. This effect is known as oil canning and is characterized by the metal deforming easily and pops in our out of its shape, resembling the pushing action one experiences when using old-style oil cans or jelly jar lids. (Kirby, 2000)

Two of the parts in this thesis suffer from oil canning, the side plates and the back plate. The parts are thin and have large surface areas. The other parts are thicker or have more indentations or ripples in the materials making them stiffer. This reduces the effect of oil canning. The effect this has on the parts is that the eigenfrequency of the modes with a

deformation such as that of the oil canning is shifted since it is not as stiff as it should be. That makes proper modeling harder.

Figure 2-2: The steel shell to the right, and the inside parts placed on the bottom plate to the left.

The steel shell consists of ten different parts. Five of these parts were already analyzed in previous year's master thesis, Gustafsson (2007), and they can be seen in Figure 2-3. The remaining five parts, shown in Figure 2-4, will be analyzed and validated using finite element analysis and experimental modal analysis.

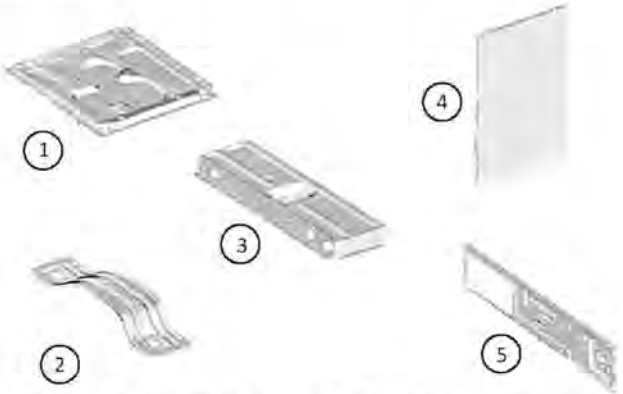

1	Bottom plate
2	Transport beam
3	Cross beam
4	Side plate
5	Front beam

Figure 2-3: Parts analyzed in previous master thesis.

The bottom plate acts as a base for the whole washing machine. Two side plates are mounted on the bottom plate and the three different beams are mounted between the two side plates. The front beam is mounted on the front side of the washing machine and the other two beams on the back side with the cross beam at the top.

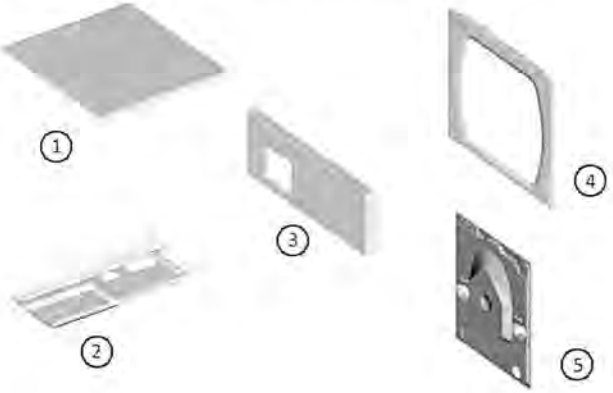

1	Lid
2	Electric bridge
3	Lower front plate
4	Upper front plate
5	Back plate

Figure 2-4: Analyzed steel shell parts in this master thesis.

Of the newer parts the lower front plate is mounted in both the bottom plate and the two side plates. The upper front plate is located directly above the lower front plate and the lid is mounted on top of the side plates, front and cross beam. The back plate is mounted on the bottom plate, side plates and cross beam. The electric bridge is located between the front and cross bream inside the steel shell. The entire steel shell, see Figure 2-5, will be treated the same way as the parts which haven't been analyzed before using EMA for validation.

Figure 2-5: The entire steel shell, left: front view, right: back view.

The entire shell structure will also be examined with the inside parts, which can be seen in Figure 2-6, mounted on the bottom plate. The inner parts are fixed to the bottom plate with four spring legs and to the cross and front beam at the top with two springs. The spring legs and the springs can be seen as black lines in figure 2-6.

Figure 2-6: The FE-model of the inside parts mounted on the bottom plate.

The models for the inside parts can be seen in Figure 2-7 and with corresponding names in Table 2-1. The inside parts assembly contains 19 different parts that were meshed using both solid tetrahedral elements and triangular plate elements. In order to reduce the degrees of freedom in the model, the original CAD models supplied by ASKO Appliances AB were simplified and some parts even removed as they were assumed not to affect the model. For more information about how the parts were modeled, see chapter 3.

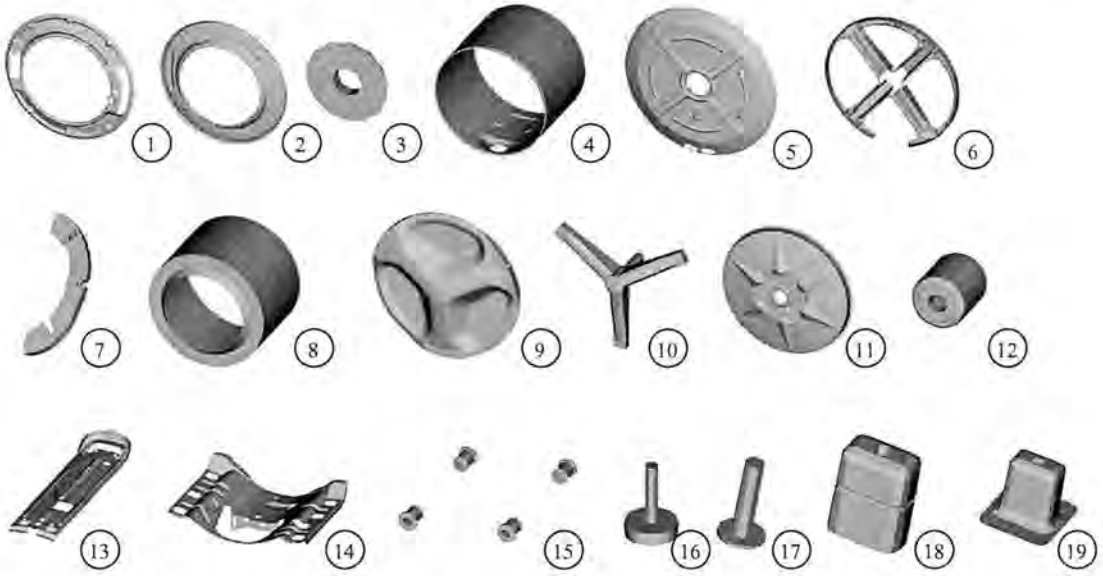

Figure 2-7: Models of details in the inside parts and feet with different scaling.

Table 2-1: Names of details in the inside parts and feet.

1	Cover plate
2	Front gable
3	Axle plate
4	Container
5	Container back piece
6	Back frame
7	Counterweight
8	Drum
9	Drum back piece
10	Convey
11	Belt pulley
12	Frame bracket bearing
13	Upper spring bracket
14	Lower spring bracket
15	Engine
16	Foot
17	Leg end
18	Rubber bushing
19	Bushing cup

2.2 Experimental modal analysis

The experimental modal analysis was conducted on the five new parts that was added to this thesis work, see Figure 2-4, and the assembled steel shell, see Figure 2-5. The method for creating a well correlating FE-model has been retrieved from the previous thesis work. The FE-models of the parts will have their material parameters and thickness updated until a good correlation is obtained with the experiment data (Gustafsson, 2007). The experimental modal analysis follows the algorithm in Figure 2-8.

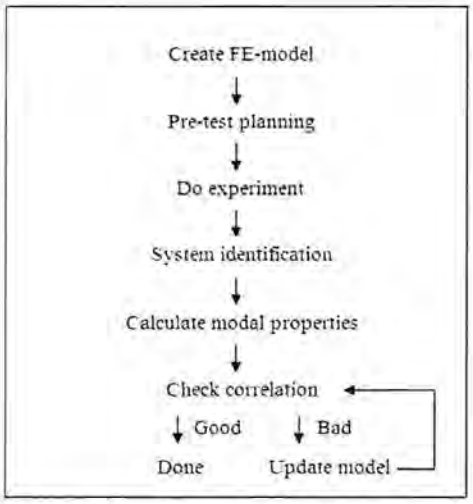

Figure 2-8: Algorithm showing the steps in experimental modal analysis in this thesis work.

2.2.1 Pre-test planning - Effective independence

Since there is only a few sensors available to use for measurement compared to the number of degrees of freedom from the FE-models, the degrees of freedom from the FE-models had to be reduced to match the number of sensors. In order to achieve the best representation of the modes using the limited number of sensors the method effective independence was used (Abrahamsson, 1999).

By using the mode matrix obtained from an initial FE-model of the structure, the method step by step removes the degree of freedom that gives the least information about the mode shapes. Eventually there is only as many measurement points on the structure as there are modes under consideration. The initial mode matrix is called the candidate matrix and contains only the translational degrees of freedom, this since the measurement devices used in this thesis only measure translational acceleration or velocity.

2.2.2 EMA Experiments

An example of the equipment used in the experiments can be seen in Figure 2-9. The data is collected on a computer using a program running in Matlab. This program controls the excitation of the structure, assembles data from the load cell and the vibration-measuring instruments. A schematic picture of the test setup and the data flow can be seen in Figure 2-10.

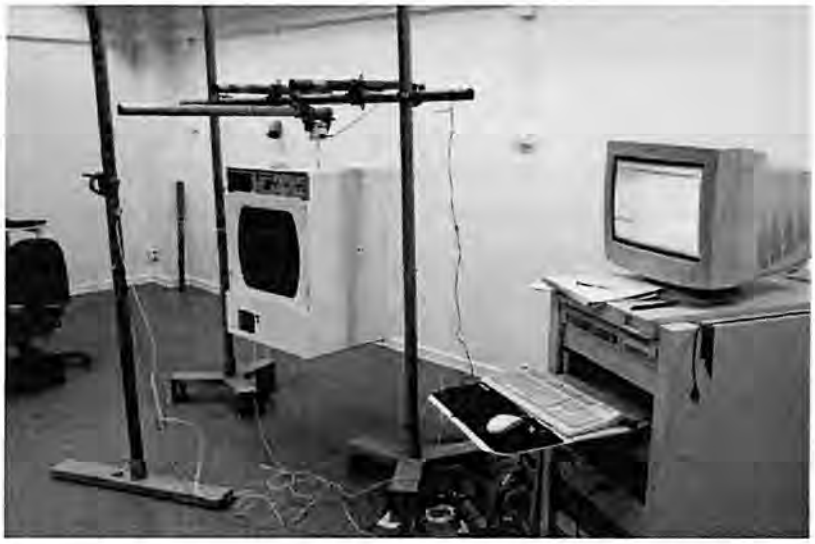

Figure 2-9: A complete experimental setup where the washing machine shell is fitted with accelerometers. Visible in the figure are the washing machine, shaker, accelerometers, amplifier, VXI and computer.

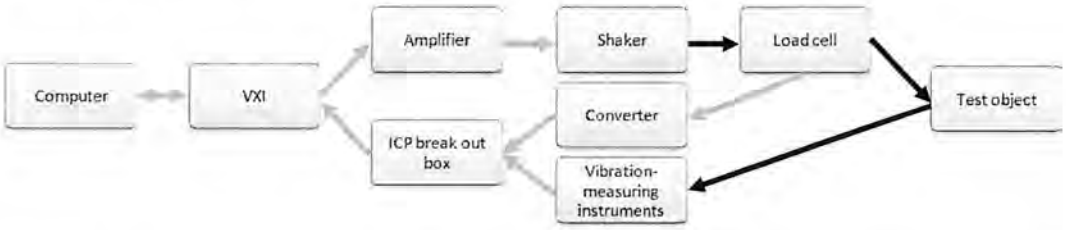

Figure 2-10: Schematic image of the measurement equipment and data flow. Gray lines are electronic signals and black lines are mechanical response.

As can be seen in Figure 2-10 the shaker converts an electric signal to mechanical vibrations whilst the load cell and vibration-measuring instrument does the opposite, converts the vibrations to electrical signals. For more information about model and serial number for the experimental equipment, see Appendix A.

The experiments are of SIMO type, single input multiple outputs. This means that the test object is subjected to a single input and gives multiple outputs as result. In this case, the single input is the force applied by the shaker and the multiple outputs are the data at the measurement points. (Craig Jr. & Kurdila, 2006)

2.2.2.1 VXI and ICP break out box

The VXI is connected to the computer via a FireWire interface. It collects multiple signal inputs and transmits them to the computer and the program that controls the VXI. It also forwards the computer signals, for example that to control the amplifier in order to control the shaker.

The load cell and the accelerometers react to the forces and the accelerations by a varying resistance. In order to convert that to voltage, a constant current is needed in the transducers. The break out box purpose is to supply that constant current to the devices and also collect the signals. (HP: Product Overview, 1998)

2.2.2.2 Amplifier, shaker, load cell and converter

To produce vibrations in the measured detail a shaker is used. Using a computer, the shaker can be controlled to create a harmonic load that is transmitted to the test piece through a force transmitting stinger and a load cell. The setup can be seen in Figure 2-11. An amplifier is connected between the computer and the shaker in order to get the signal strong enough.

Figure 2-11: The Shaker, stinger and load cell.

The applied force is controlled by feeding the shaker with a sinusoidal signal with a specified frequency and amplitude. The stinger is a thin steel rod that transmits axial load but no bending moment, in these experiments it is a piano wire. Between the stinger and the test piece a load cell is located so that the load applied can be recorded. The load cell gives a charge proportional to the load which is transformed to voltage through a charge-to-deltatron converter (Brüel & Kjaer, 2006), seen in Figure 2-12. The load cell is connected to the break out box so that its voltage can be measured and sent to the computer.

Figure 2-12: Charge-to-Deltatron converter for the load cell signal.

2.2.2.3 Vibration-measuring instruments

Two different types of measurement methods are used for these experiments, a laser Doppler vibrometer (LDV) and accelerometers. The LDV was used to measure the responses from the upper front plate and the lower front plate. The accelerometers were used to measure the responses from the lid, electric bridge, back plate and the assembled steel shell. Both types of instruments were connected through a break out box.

When measuring with the LDV, a laser beam scan over the structure and measures the velocity in the direction of the laser beam at predefined locations. The LDV equipment is of the brand Polytec. The Polytec system can measure, analyze and present the data, but here the

Polytec system is only used to measure the velocity and transmit that to Matlab through the VXI system. (Polytec, 2002)

The other way to measure the dynamic response is by attaching accelerometers at the measurement points. In this master thesis accelerometers from PCB Piezotronics and Dytran instruments, see Figure 2-13, were used. These came in different sizes weighing 4 grams, (PCB Piezotronics), down to a weight of 0.2 grams (Dytran Instruments Inc.). The accelerometers were attached to the structure using wax and most of them measure the acceleration in the direction normal to the surface to which they attach. Wax can be used to attach accelerometers for measuring vibrations up to 1000 Hz. Each accelerometer has a specific calibration constant in order to convert acceleration to voltage.

Figure 2-13: Picture of accelerometers used in the experiments. Figure sizes are not according to scale.

2.2.3 System Identification

Data from the experiments comes in the form of frequency response functions (Ewins, 2000). In order to get information about mode shapes from the experimental data, system identification is necessary. This means that using the information retrieved from the measurement points, a state-space model of the system is identified. In this case a linear state-space model is used according to the system equations seen in (2-1).

$$\begin{aligned} \dot{x} &= \boldsymbol{A}x + \boldsymbol{B}u \\ y &= \boldsymbol{C}x + \boldsymbol{D}u \end{aligned} \tag{2-1}$$

Here u is the stimuli, y the response and x is the systems state vector. The result from the system identification is the matrices A, B, C and D from which the systems eigenfrequency and corresponding eigenvectors can be calculated (Abrahamsson, 1999).

To do the system identification for each part, the System Identification toolbox in Matlab was used (The Mathworks). The toolbox imports the frequency response function and a vector containing the frequencies measured in the experiment. The estimation also requires that a model order is inserted. This model order should be at least twice the number of modes picked up by the model, but because of noise in the frequency response functions this is often too low. In this thesis, the model order used was found by trial and error. Different model orders were tried until finding the one that gave the best fit, but without picking up too much noise.

2.2.4 Correlation method and model update

To verify that the FE-model behaves like the real model, a measure of the correlation between it and the real detail must be found. This can be done by first establishing the Modal Assurance Criterion (MAC) numbers to see that the correct mode shapes has been obtained from the model. Secondly, when the mode shapes are to satisfaction, a calculated frequency response function using the FE-model is compared to the obtained frequency response function from the experiments.

The reason for calculating the frequency response function is that the MAC number considers neither the amplitude nor the eigenfrequency of the modes. When comparing the frequency response functions it is easy to see how well the frequency matches and if the damping calculated from the state-space model is accurate or not since the damping affects the amplitude of the response.

2.2.4.1 Modal assurance criteria

This method compares the mode vectors from the experiments to the mode vectors from the FE-model only containing the degrees of freedom obtained from the Pre-test planning (see 2.2.1). By calculating the angle between the experimental and the analytical mode vectors and taking the cosines squared of this angle, a value from zero to one can be obtained. This value is called a MAC value and indicates how well two modes correlate, the closer to one the value is the better the correlation. The correlation can be considered good if the MAC number is above 0.9 for corresponding modes. If it is below 0.8 the correlation can be considered poor. (Abrahamsson, 1999)

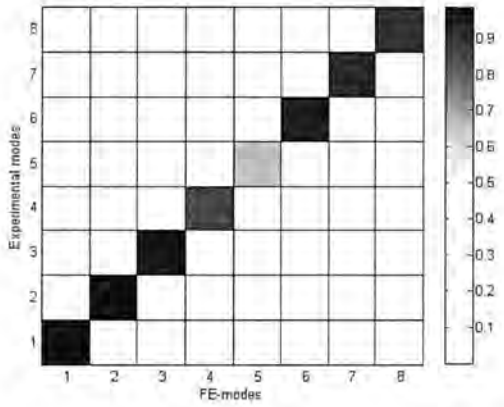

Figure 2-14: A visualization of a MAC-matrix.

Figure 2-14 shows an example of a graphical representation of a quite well correlated FE-model, only mode five is poorly correlated. Sometimes the matrix lacks large diagonal elements, then the conclusion can be made that there is something wrong in the FE-model since the modes appear in the wrong order. The model then has to be updated in order to get a more accurate model.

As mentioned before, the model order of the system is often much higher than twice the number of modes in the system. The calculations will then result in more eigenfrequencies and modes than there really are in the system. Using the MAC numbers, the correct modes

corresponding to the FE-model can be chosen and its modal properties can be used in further calculations.

2.2.4.2 Calculated frequency response function

To calculate the frequency response functions from the FE-model the Mode-Superposition Method is used (Craig Jr. & Kurdila, 2006). When using this method the damping for each mode has to be calculated as well. This is calculated using equation (2-2) where λ_r is the complex eigenvalue for each mode retrieved from the state space model.

$$\lambda_r \equiv \mu_r + jv_r = -\zeta_r \omega_r + i\omega_r \sqrt{1-\zeta_r^2} \tag{2-2}$$

Using equation (2-2) the modal damping for each mode can be identified as equation (2-3).

$$\zeta_r = -\frac{\mu_r}{\omega_r} \tag{2-3}$$

If the general shape of the curve calculated using the mode-superposition method do not match the measured frequency response function, the model needs to be updated.

2.2.4.3 Model update

In this thesis work, the four parameters updated are density, Young's modulus, Poisson's ratio and thickness of the elements used in the model. To update the FE-models, a script is used that assigns the above parameters, solves the eigenvalue problem in Abaqus and extracts the FE-mode vectors from the solution file. The script then calculates the frequency response functions and compares them to the measured frequency response function to give a measurement on the error. The script can be set to optimize either the material parameters or the modal damping and the error can be measured as either an error in eigenfrequencies or the amplitude at the eigenfrequencies.

The function fminsearch in Matlab is used to minimize the error from the script (The Mathworks). It does so by updating the parameters previously described. This results in the parameters which gives the smallest error. These parameters are assigned to the models which are used in the steel shell assembly.

For the assembled steel shell, the method from the previous year's thesis work is used. The modeled screws connecting the parts are created in sets to enable an individual property update of each set. Each set consists of modeled screws connecting two parts. By that theory, the correlation of the steel shell should be able to be adjusted by changing the connection properties between the individual steel shell parts. (Gustafsson, 2007)

2.3 Spin up test and correlation

With the drum and engine placed inside the steel shell, the engine was run at different rotational speeds to see the response in the steel shell and under the feet of the machine. To induce more forces from the drum, an unbalance was added inside. The response from the steel shell was measured using accelerometers and the response from the feet using load cells. This data were then compared with simulated accelerations and forces from the FE-model to see if a good correlation could be obtained.

The equipments used in these experiments are quite similar to those used in the experimental modal analysis, see 2.2.2. The main difference is the way the vibrations are induced on the machine. For these experiments, a computer program is used to control the engine speed which rotates the drum. From the program, tachometer data was obtained describing the speed curve during the experiment. This tachometer data also includes a timestamp at each data point so that the data from the accelerometers can be matched to a specific speed on the engine.

The accelerometers used are the same as in the previous experiments, see chapter 2.2.2.3. When measuring the reaction forces under the feet of the washing machine, one load cell is placed under each foot.

The unbalance weight was a 22 cm long brass rod which weighs 0.097 kg. The rod was attached with tape along one of the plastic carriers inside the drum. The reason for not using a heavier load is because the damping in the legs of the inside parts has been removed in order to have as much linear behavior of the machine as possible. When using a heavier load, the vibration of the drum becomes very large.

In all experiments using the engine and drum, measurements was performed at the same rotational speeds and during the same amount of time. The rotational speed was constant for 4 seconds at every 25th rpm up to 2000 rpm. These are the nominal values; the real rotational speeds are retrieved from the tachometer file after the experiments. This tachometer curve is then used in the force and accelerations plots from the experiments so that the data can be viewed against rotational speed instead of time.

The sample frequency used both for acceleration and force measurements were 2 kHz. Since the time it took to step through the rotational speeds using the above ramp function was almost 5 minutes, it would have been difficult using a higher sample frequency. The data files would have been too large to handle.

The measured acceleration and force signals were analyzed using so called Campbell diagrams. The diagram is basically a spectrogram used to check for coincidence of vibration sources with natural frequencies. In the diagram, the amplitude of the signal is represented by different shades of gray, a larger amplitude shows as a darker color. (Campbell Diagram, 2009)

The method used in the Campbell diagrams for comparing the frequency of the signals over spin up is done by using short-time Fourier transforms, (STFT, 2009). The number of frequency points and the size of the Hanning window, (The Hanning window, 2009), used to calculate the discrete Fourier transforms were 2048.

2.3.1 Correlation method and model update

The correlation was done by calculating the harmonic response using NX Nastran analyzing method modal frequency response. The load is considered harmonic since the drum where the unbalance is located is rotating. Modal frequency response analysis is an approach to computing the frequency response of a structure in Nastran. This method uses the mode shapes of the structure to reduce the size and uncouple the equations of motion. The mode shapes are calculated in an earlier analysis to determine the behavior of the structure at the natural frequencies. (Siemens PLM Software, 2008)

Because of the rotation of the drum, forces and moments are created which will not be present in a static model. Instead these loads need to be calculated and added to the model. Loads that

need to be added are a force from the unbalance, so called static unbalance, and moments for the unbalanced rotational axis of the rotating parts, so called dynamic unbalance.

An important part when trying to simulate the running machine is the spring leg. Since the time frame of this thesis will not allow any deeper studies of the spring leg and the rubber bushings attaching the spring leg to the bottom plate and inside parts, the parameters of these will be estimated by letting the observed modes of the inside parts occur at approximately the correct eigenfrequencies as by the measured data.

2.3.1.1 Unbalance force

The rotation of the drum gives rise to static and dynamic loads. These were applied in the nodal equivalent point P, see Figure 2-15 using a static equivalent transformation.

The static load consists of a force and a moment from the unbalance weight. The force is calculated using equation (2-4) and the transformation to point P give rise to the moment which is calculated using equation (2-5).

$$F = mr\omega^2 \tag{2-4}$$

$$M = Fd \tag{2-5}$$

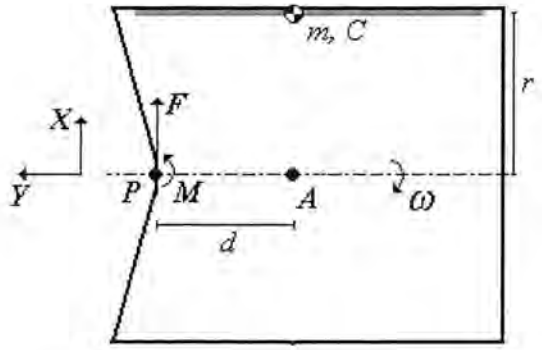

Figure 2-15: Schematic drawing of drum seen from above.

$m = 0.097$ kg	Mass of unbalance load.
$r = 0.221$ m	Radius from centre of drum to centre of mass in unbalance load.
$d = 0.096$ m	Distance between point P and A.
A	Point C projected on the rotational axis Y.
C	Centre of mass for the unbalance load.
P	Point where the load is attached.
F	Force from the unbalance load [N].
M	Momentum from the unbalance load [Nm].
ω	Rotational speed of the drum around the Y axis [rad/s].

Parts that rotate around another axis than their own rotational axis give rise to dynamic unbalanced moments, $\bar{\boldsymbol{M}}_{\boldsymbol{d}}$, which is calculated using equation (2-6), the angular momentum law, with respect to the center of mass of the rotating parts. The dynamic unbalanced moments were transferred to, and applied at the point P. When calculating $\bar{\boldsymbol{M}}_{\boldsymbol{d}}$ the time derivative of the angular momentum is needed, see equation (2-7) for the angular momentum, $\bar{\boldsymbol{L}}$, (Japp, 2003).

$$\Sigma \overline{M}_d = \dot{\overline{L}} = \frac{\delta \overline{L}}{\delta t} + \boldsymbol{\Omega} \times \overline{L} \tag{2-6}$$

$$\overline{L} = \overline{I}\boldsymbol{\Omega} \tag{2-7}$$

A bar over the symbols means that it is calculated with respect to the centre of mass. The rotating parts can be seen in Figure 2-16.

Figure 2-16: FE-model of the rotating inside parts, belt pulley, convey and axle, drum back piece and drum.

An average modal damping of 0.006 was calculated from the results of the EMA for the entire steel shell and was estimated to be 0.08 for the three first modes where only the inside parts moved due to compression and bending of the spring legs, see Appendix G1.

Three analyses are needed in order to get the results from these simulations. The first is a normal modes analysis using Nastran (FEMAP 10.0.1 Online Help, 2008), where the eigenfrequencies and the corresponding mode shape is calculated. This is then used to calculate the harmonic response for two cases when applying the load.

Since the drum rotates in reality and time dependent simulations would have taken a very long time, harmonic response simulations were done for two load cases, using the Nastran analysis method frequency/harmonic, and then summed over one rotation. For the first case the force from the unbalance was applied in the *X*-direction see left side of Figure 2-17 and the moments were applied according to the figure. In the second case the force was applied in the Z-direction and the moments according to the right side of Figure 2-17. Combining these two cases using equation (2-8) and (2-9) give the total acceleration and force for every degree of one drum revelation at every specific rotational speed.

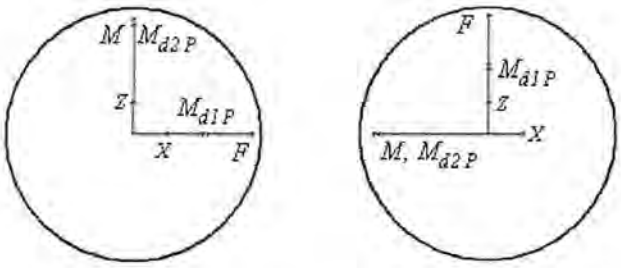

Figure 2-17: Drum seen from the front with forces and moments indicated in figure at two instances of time during one revolution. The left figure shows load case one and the right shows load case two.

$$a_{ij} = a_i^x \cos(\theta_j) + a_i^y \sin(\theta_j) \quad i = 0,25,50,...,2000rpm \quad j = 0,1,2,3,...360° \tag{2-8}$$

$$F_{ij}^R = F_i^{Rx} \cos(\theta_j) + F_i^{Ry} \sin(\theta_j) \quad i = 0,25,50,...,2000rpm \quad j = 0,1,2,3,...360° \tag{2-9}$$

The maximum acceleration and force at the discrete frequencies are plotted onto the respective measured curve to see how well the model correlates with the real washing machine. The model is judged to be well correlated if the peaks in the accelerations and forces are at approximately the same frequency and the amplitudes of the peaks are close. The model can be updated both through changing the average damping mentioned above, and by modifications in the different parts of the inside parts.

2.3.1.2 Spring legs

The spring legs are modeled as a circular bar elements in Nastran. The cross section area is determined to be the same as in the cross section of the spring leg housing. The housing which consists of a steel pipe is used as a reference when deciding the bending stiffness of the bar. The axial stiffness in the bar should be an approximate match to the spring stiffness of the spring currently in the spring legs. From this, Young's modulus can be determined. Using the original bending stiffness an updated moment of inertia can also be calculated. This can be seen in equations (2-10) and (2-11) where E_{upd} and I_{upd} are the properties used for the stiffness in the model.

$$\frac{E_{upd} A}{L} = k \Rightarrow E_{upd} = \frac{kL}{A} \tag{2-10}$$

$$E_{upd} I_{upd} = EI \Rightarrow I_{upd} = \frac{EI}{E_{upd}} \tag{2-11}$$

3 Modeling of parts and assembly

The CAD-models for the parts in the steel shell were supplied as a separate file for each part and the CAD-models for the inner parts came in assemblies where many parts were placed in the correct positions relative each other. Most of all the parts are thin and can be modeled with plate elements. In a previous master thesis (Henriksson & Melander, 2006) an investigation of element choice was made and it was determined that triangular plate elements of the size 5 mm was proper. Because of this, triangular plate elements of the size 5 mm were used as a basis. If smaller element size gave better results when comparing eigenfrequencies, those were used instead. The element size for every part can be seen in Table 3-1. Some simplifications have been done due to holes and areas with complex geometry, the extent of simplifications can be seen in Table 3-1 and is described in detail in Appendix B.

Most of the inside parts have been modeled with the same element type as the steel shell parts. For the parts that could not be considered thin, solid tetrahedral elements was used. The element size for the inside parts were bigger than for the steel shell parts (up to 20 mm) and the geometry were simplified to a larger extent. This since the use of these parts is not to determine the exact structural behavior but to transfer loads and structural motion to the steel shell. The computational time is also a consideration here, if the inner parts mesh is too fine the computational time will be too long.

When meshing the parts, no profound studies of the mesh have been made. This since the automatic meshing tool in Femap worked well according to previous years thesis work. The only check of the mesh was to look for narrow elements and manually remesh to avoid singularities when running the analyses.

All parts are listed in Table 3-1 with the quantity of every part in the entire assembly, the element types that have been used to model each part, the size of the elements, the number of elements and a comment on the extent of the simplification. The simplifications comment "None" implies that no changes have been made to the geometry before meshing. "Minor" implies that small holes, punched text, bulges and small areas of complex geometry are removed. "Modest" implies the same things as "minor" but the number of simplifications is higher. "Big" implies that larger areas of geometry have been modified or removed. "Total" implies that a new part has been made, either from two or more parts that have been merged into one, or a new part that has been made with one or more parts as references.

The names of the element types are NX Nastran standard names; CTRIA3 stands for triangular plate elements, CTETRA is tetrahedral 3D elements, CBAR stand for bar elements, CBUSH is spring elements, mass elem. stands for mass elements and RBE2 is rigid elements (FEMAP 10.0.1 Online Help, 2008).

Table 3-1: Properties for all parts in the modeled washing machine.

Part name	Qty	Element type	Element Size [mm]	#Elements	Simplifications
Shell structure parts					
Bottom plate	1	CTRIA3	4	63811	Minor
Side plate	2	CTRIA3	5	123360	Modest
Lid	1	CTRIA3	10	11714	Modest
Transport beam	1	CTRIA3	5	14945	Minor
Cross beam	1	CTRIA3	3	54455	Minor
Front beam	1	CTRIA3	2,5	17962	Modest
Electric bridge	1	CTRIA3	2	75336	Minor
Lower front plate	1	CTRIA3	3	37505	Modest
Upper front plate	1	CTRIA3	3	44790	Minor
Back plate	1	CTRIA3	5	44699	Minor
Bolts	1	CTRIA3	3	2770	Total, big
Feet and Spring parts					
Spring leg	4	CBAR & RBE2	10	48	Total, big
Leg end	4	CTETRA	3,5	2290	Total, none
Balance spring	2	CBUSH	-	2	Total
Foot	4	CTETRA	4	5020	Modest
Inside parts					
Container	1	CTRIA3	20	6570	None
Container back piece	1	CTRIA3	20	4373	None
Drum	1	CTRIA3	20	2880	Total, big
Drum back piece	1	CTRIA3	10	6012	Modest
Convey and axel	1	CTETRA	12	15353	Total, big
Axel plates	1	CTETRA	15	278	Total, none
Belt pulley	1	CTRIA3	15	1912	Total, big
Upper spring bracket	1	CTRIA3	10	3043	Modest
Lower spring bracket	1	CTRIA3	10	10412	Modest
Front gable	1	CTRIA3	10	8970	Modest
Front Cover plate	1	CTRIA3	10	7766	Modest
Counterweight	2	CTETRA	10	29914	None
Bushing cup	4	CTRIA3	8	1176	None
Rubber bushing	4	CTETRA	8	5438	Modest
Back frame	1	CTRIA3	15	5276	Total, none
Frame bracket and bearing	1	CTETRA	10	3591	Total, big
Engine	1	CTETRA, RBE2 & mass elem.	5	1974	Total, big
Total	**50**			**613645**	

3.1 Simplifications made on parts

Typical simplifications done on the steel shell parts are small holes that have been removed or small areas of complex geometry that was simplified. The holes and the text can be removed since the mass of the material used is small in comparison to the total mass, therefore it can be assumed to have a small impact on the results. To accurately model small geometries means that the element size has to be extremely small which is something best avoided.

The geometry simplification visualized in Figure 3-1 is a rivet that has been removed and replaced by a smooth edge. The material properties are homogenous in the area of the new geometry. These types of simplifications proved to have little effect in the modal analysis performed in previous years thesis work (Gustafsson, 2007). Without these updates, these areas would have been difficult to mesh. The rivets are present in several parts, to see how models and simplifications are connected, see Appendix B.

Figure 3-1: Original geometry to the left and simplified geometry to the right.

For the inside parts, larger holes were removed and less complex geometries were simplified. One example is the innermost drum that has a lot of small holes which was removed to be able to use a larger mesh size. Other examples are three axle plates which were modeled as one solid part to avoid the use of contact modeling between them and to keep the number of parts down.

3.2 Assembly of shell structure

Parts in the steel shell were assembled using the results from the individual analysis of the mesh, material and element properties. The parts are connected to each other by elements representing bolts used in reality. In a previous master thesis, see Gustafsson (2007), the rivets used to assemble some of the parts were replaced with bolts when the real steel shell was assembled. The assembly of parts proceeds from where previous master thesis left. Parts that have been added in this work are back plate, lid, upper front plate, lower front plate and electric bridge.

The connecting bolts are created by the same type of plate elements used on the parts. Element and material properties are assigned to every set of bolts connecting two parts. The possibility of modifying the bolt properties is used to check what effect the bolt properties have on the behavior of the shell structure.

3.3 Assembly of entire machine

The CAD models of the inside parts were delivered preassembled in six files. The only parts not preassembled were the spring legs and balance springs. All the inside parts have been meshed and assembled into one file. The parts are connected to each other using a connection property called glue in Femap. The glue connection property connects two parts to each other in defined regions using glue elements. A glue element consists of a stiff spring element that connects two parts and prevents relative motion (FEMAP 10.0.1 Online Help, 2008). This connection type is also used to connect the feet to the bottom plate of the steel shell.

The inside parts are mounted in the steel shell on four spring legs attached to the bottom plate and using two supporting balance springs at the top to keep the drum balanced in the direction of the rotational axis. Each spring leg consists of one helical spring and one friction damper which can be seen in Figure 3-2. The friction damping consists of a ring in foam rubber sliding against the wall producing friction. To keep the system as linear as possible, the damping in the spring legs has been removed.

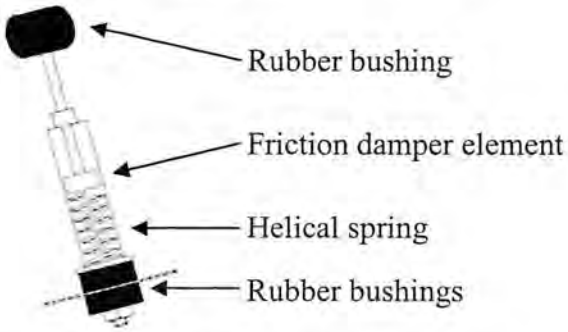

Figure 3-2: A spring leg with ingoing parts.

Removing the damping in the spring legs was done by drilling a hole in the leg wall and then compressing the spring until the foam ring aligned with the hole, see Figure 3-3. The foam ring was then dragged out through the hole and the hole was covered with duct tape.

Figure 3-3: Compressed spring leg during removal of damping foam.

4 Experimental setup

Measurements have been performed on parts and assemblies that haven't already been tested in previous thesis works. The results on the previous tested parts were reproduced in order to save testing time. The results from the EMA performed in previous thesis work and the calculated eigenfrequencies are compared in Appendix C.

The experiments can be divided in two primary types; those for validating FE-models (EMA), and those for analyzing the effects that an unbalance load in the drum has on the steel shell (Spin up tests).

4.1 EMA experiments

Two different experimental setups have been used where the difference between them was how the vibrations were measured, either with a LDV or with accelerometers. These methods are described under chapter 2.2.2.3.

The general implementation of the experimental setup starts with rigging the experiment. The test subject is suspended in a steel pipe frame with fishing-line in two suspending points or more if necessary. The load cell is glued on the test subject and the stinger is aligned with the normal to the surface where the load cell is attached. Accelerometers are attached, or measurement points in the LDV are assigned, to pre-calculated locations using effective independence, see chapter 2.2. The test subject is excited using the shaker and acceleration or velocity is registered and stored together with the load on the load cell. A frequency range is covered by a stepped sine procedure. The data from the experiments comes in the form of frequency response functions.

In Table 4-1 a summary over experimental properties can be found. These properties are the name of the detail, the frequency range, the attachment points of the fishing lines, what measuring system that has been used (accelerometers or LDV) and how many measurement points that has been used. In all experiments a frequency step size of 0.05 Hz has been used.

Table 4-1: EMA experimental properties.

Detail	Range [Hz]	Suspension	System	#MP	#Stinger positions
Lid	7 – 155	2 corners	acc.	9	1
Electric bridge	35 - 347	2 corners	acc.	10	2
Upper front plate	11 - 394	2 corners	LDV	11	1
Lower front plate	15 - 360	2 holes	LDV	11	1
Back plate	19 - 198	2 corners	acc.	8	2
Steel shell	5 - 120	4 corners	acc.	9	3

4.1.1 Lid

Nine accelerometers, one stinger position and two suspension points have been used in the experiment which can be seen in Figure 4-1. All accelerometers measured in the Z-direction except accelerometer number seven which measured in the Y-direction.

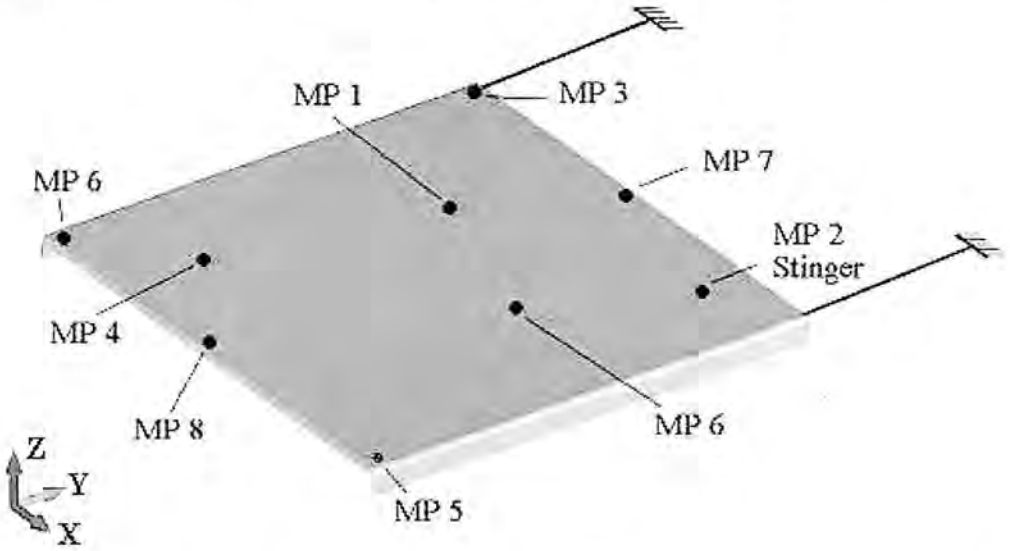

Figure 4-1: Accelerometer, stinger and suspension positions pointed out on the Lid.

4.1.2 Upper front plate

Eleven measurement points with the LDV have been used together with one stinger position which can be seen in Figure 4-2. All velocity measurements were done in the Y-direction, the same as the stinger direction. The test piece is suspended in the Z-direction at two mounting holes.

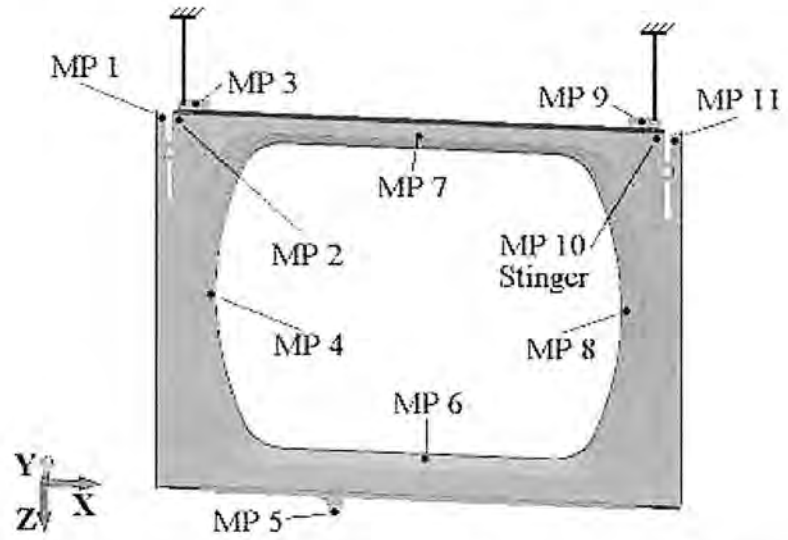

Figure 4-2: Measurement points, stinger and suspension positions pointed out on the upper front plate.

4.1.3 Lower front plate

In the experiment, eleven measurement points with the LDV have been used together with one stinger position and two suspension points. Positions for all these details can be seen in Figure 4-3. The measurement and stinger direction are in the Y-direction. The suspension was attached in two mounting holes at the bottom of the detail.

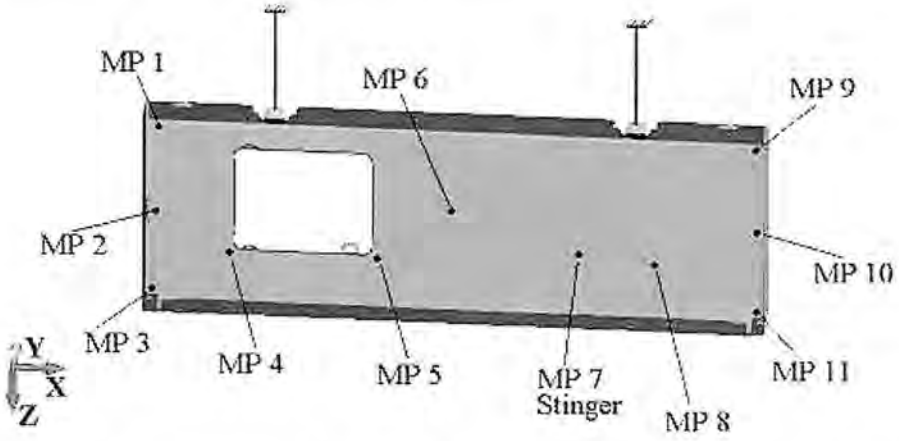

Figure 4-3: Measurement points, stinger and suspension positions pointed out on the Lower front plate.

4.1.4 Electric bridge

Ten accelerometers and two stinger positions were used which can be seen in Figure 4-4 and Figure 4-5. The detail is suspended in the X-direction, in two holes. All accelerometers measures in the direction normal to the surface they attach to, except accelerometer eight and ten, which measures in the Z-direction. Stinger one apply force in the Z-direction and stinger two on the edge perpendicular to the direction of measurement point two.

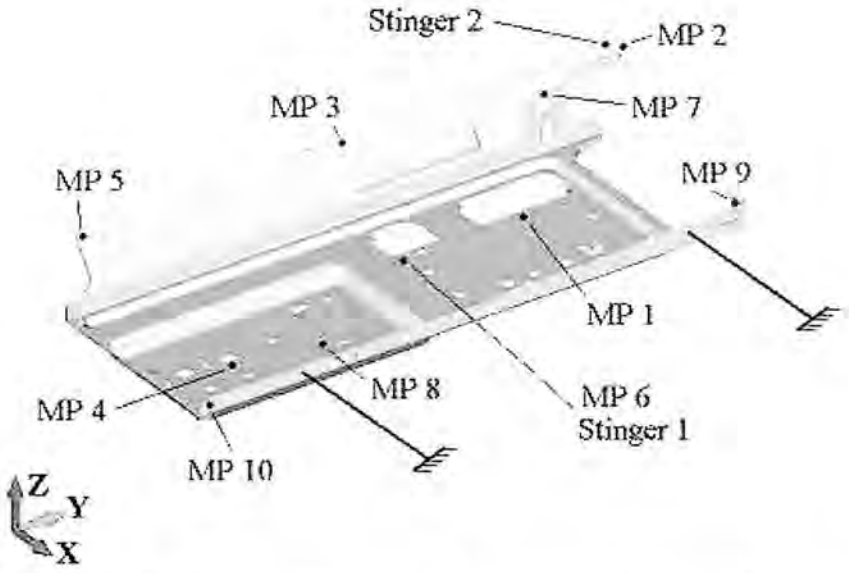

Figure 4-4: Accelerometer, stinger and suspension positions pointed out on the Electric bridge.

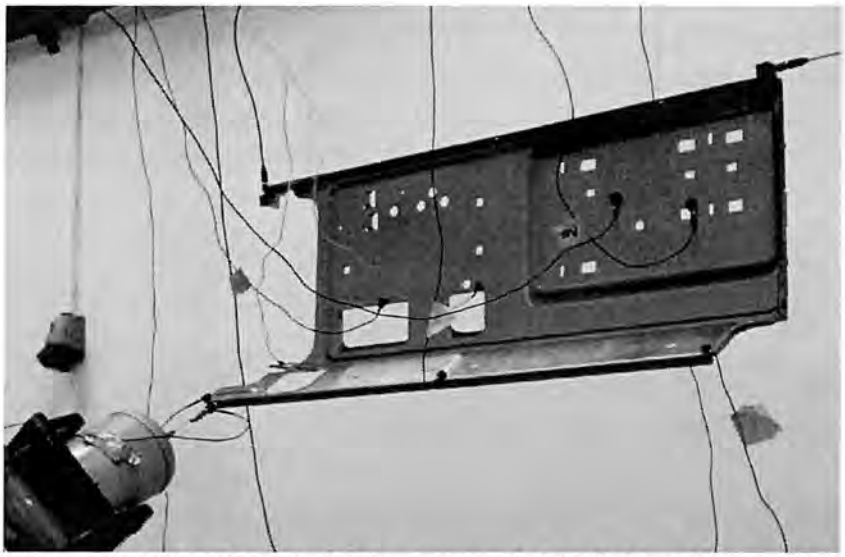

Figure 4-5: The Electric bridge suspended in fishing lines, with accelerometers and stinger attached in position number two.

4.1.5 Back plate

On this detail, eight accelerometers, two stinger positions and two suspension points were used which can be seen in Figure 4-6. All accelerometers measured in the Y-direction, the same as the stinger direction. The fishing-lines were attached in two mounting holes in the two upper corners.

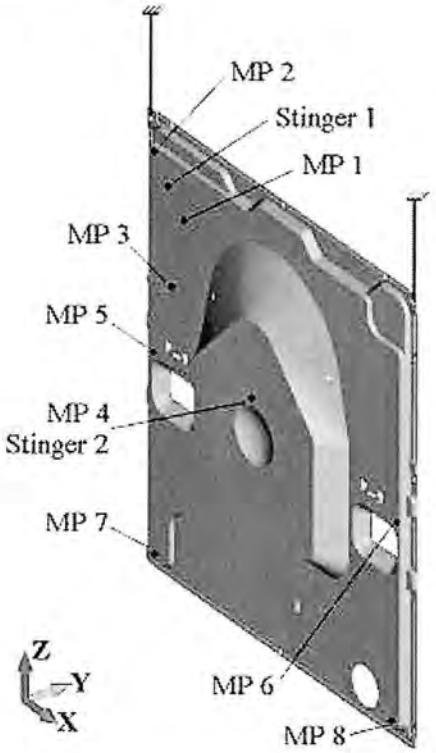

Figure 4-6: Accelerometer, stinger and suspension positions pointed out on the Back plate.

4.1.6 Steel shell

For the measurements on the steel shell, nine accelerometers, three stinger positions and four suspension points were used which can be seen in Figure 4-7. Because of the weight of the structure, multiple fishing lines in every suspension point had to be used. The suspension points were located in each top corner of the steel shell. Accelerometer number one, two and eight measured in the Z-direction, number three, four and six measured in the X-direction and number five, seven and nine measured in the Y-direction.

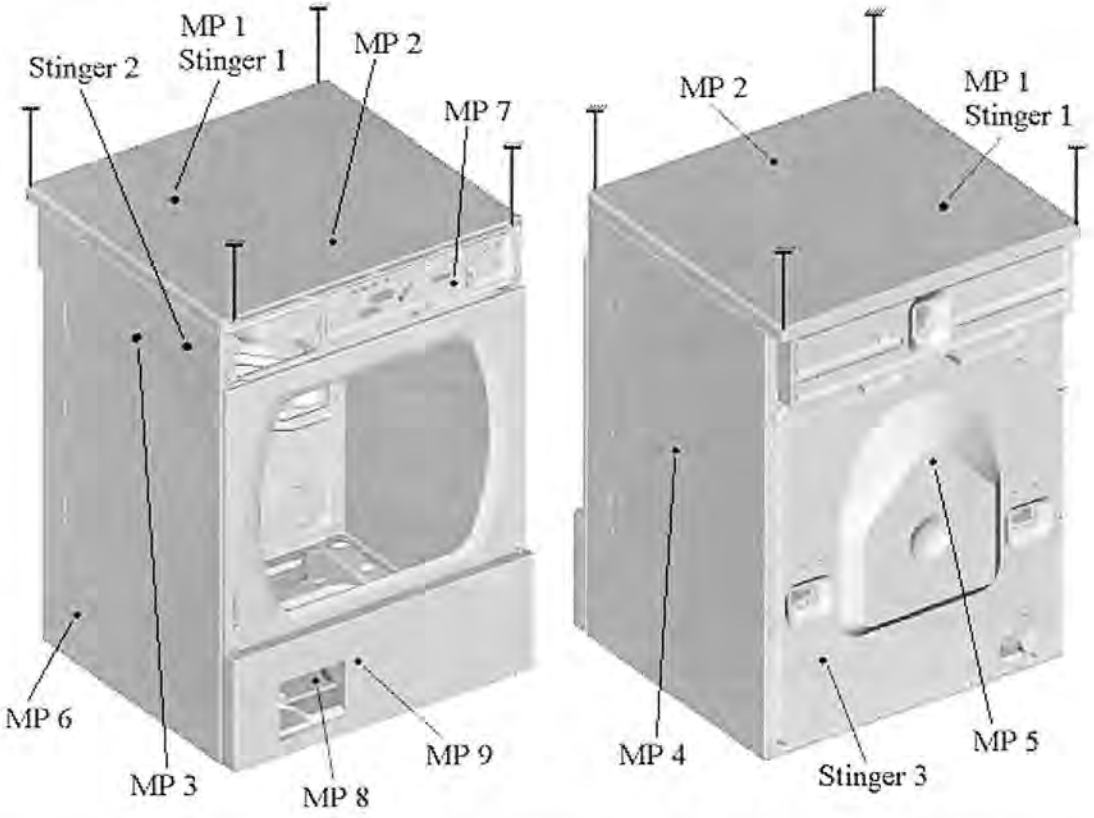

Figure 4-7: Accelerometer, stinger and suspension positions pointed out on the steel shell.

4.2 Spin-up experiments

The experiments on the entire washing machine, the steel shell with engine and drum, are done to compare the constraint forces under the feet and the accelerations at specified points. The excitation of the washing machine was done by running the drum and engine over a range of speeds with an unbalance weight attached in the drum.

Two different types of experiments have been performed; one type of experiment where only accelerations on the steel shell and drum container were measured and one where the forces under the feet and accelerations on the drum container were measured. The accelerations on the drum container were measured in three points, one in each of the three orthogonal directions. These three points were the same in all spin up experiments.

In both types of experiments, an unbalance has been added in the drum to simulate a wash load, the weight can be seen in Table 4-2. The load is a brass rod that is taped inside the drum. The speed of the drum is controlled by a program running on a PC connected to the engine.

The rotational speed is stepped between 25 rpm and 2000 rpm with increments of 25 rpm with speeds that are held constant for four seconds. Tachometer data from sweeping over the speed range is stored, specifying what speed the engine had at a specific time. The engine cannot hold a perfect constant rotational speed on the drum. The fluctuations of the speed get worse the faster the drum rotates. Speeds above 1950 rpm are impossible to reach. All equipment used for the engine steering and information on how to use it has been provided by Lic. Eng. Thomas Nygårds.

For the experiments where only accelerations were measured, the machine was placed on either a heavy steel table, as in Figure 4-8, or on a concrete floor. Because of the amount of collected acceleration data the rotational speed sweep is divided in five parts, each with a range of 450 rpm. The results from all parts are cut and pasted together after the experiment using the tachometer data as a reference. The speed range for every experiment can be seen in Table 4-2.

Figure 4-8: Acceleration measurements on whole washing machine, on steel table.

When measuring the forces under the feet and the accelerations on the drum container, the machine was placed on a rig which consists of a heavy steel block that four load cells were attached to. The machine was placed on the load cells and leveled using the measured forces under each foot. The feet under the heavy block can be changed between steel feet and feet with rubber soles (Nygårds, 2009). In this test rig, LabView is used for controlling the engine and collecting data.

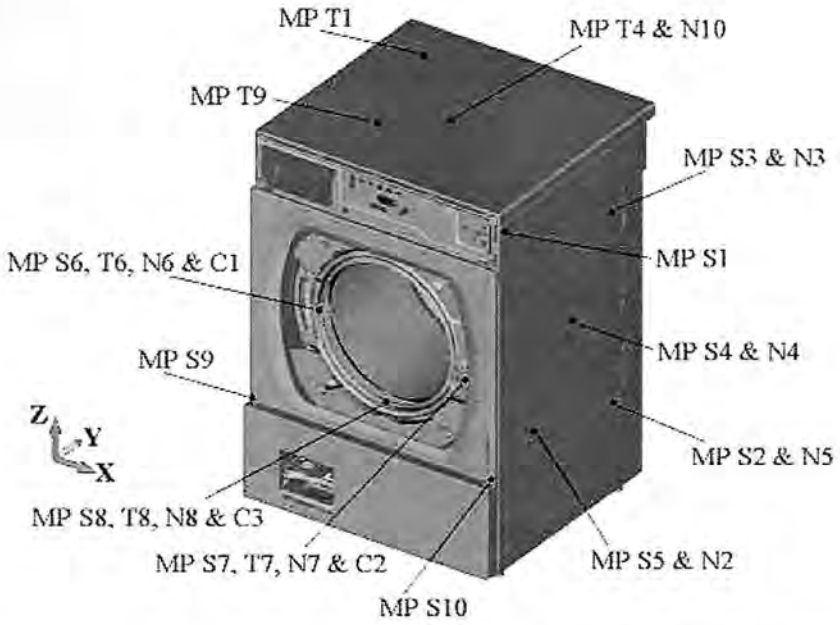

Figure 4-9: Accelerometer positions pointed out on the entire washing machine, seen from the front.

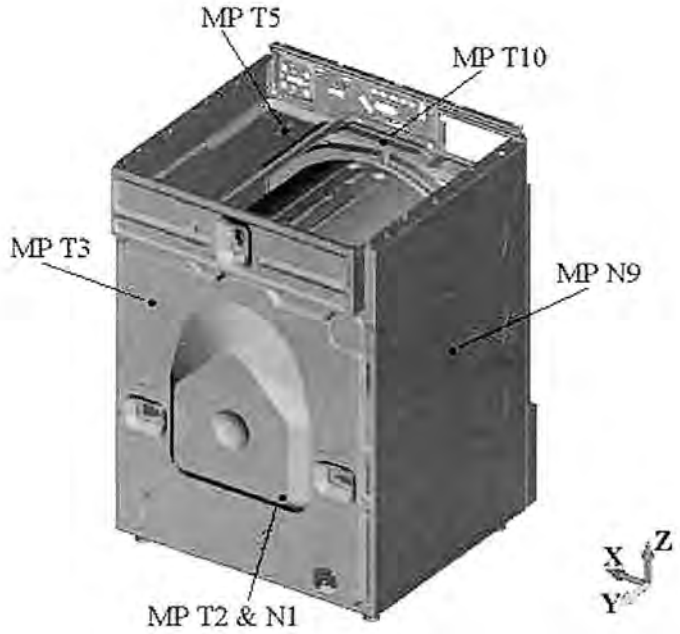

Figure 4-10: Accelerometer positions pointed out on the entire washing machine, seen from the back and with the lid taken off.

In Table 4-2, properties of the different experimental setups are listed. These are the experiment number, range of revolution speeds, weight of the unbalance load, what the machine was suspended on, what type of measurements that was done, which set of accelerometer positions that was used, how many measurement points that have been used and the type of bushing that has been used between the spring leg and the bottom plate. The letters in the Acc. Set column names the set of measurement points used, these sets can be seen in Figure 4-9 and Figure 4-10.

Table 4-2: Properties from the experiments on the entire washing machine.

Name	Range [rpm]	Weight [g]	Suspension	Measurement devices	Acc. Set	MP	Bushing
Exp 1a	25 - 1800	None	steel table	acc	S	10	steel
Exp 1b	25 - 1800	None	steel table	acc	T	10	steel
Exp 2a	25 - 1800	97	steel table	acc	S	10	steel
Exp 2b	25 - 1800	97	steel table	acc	T	10	steel
Exp 3	25 - 1800	97	steel feet rig	load cell, acc	C	4, 3	steel
Exp 4	25 - 1800	97	rubber feet rig	load cell, acc	C	4, 3	steel
Exp 5	25 - 2000	97	floor	acc	N	10	steel
Exp 6	25 - 2000	97	floor	acc	N	10	rubber

5 Results

In this chapter the results from the measurements and simulations will be presented. The chapter is divided in three sections, the separate parts, assembled steel shell and the inside parts assembled in the steel shell during spin up. The overall results shows that the model of the steel shell correlates well on most of the modes up to 60 Hz and that the model of the inside parts need more work in order to give better results.

5.1 Separate parts

The results from the separate models from previous years thesis work could be reproduced successfully. A comparison between the eigenfrequencies obtained from these reproduced models and the previously made EMA by Gustafsson (2007) can be found in Appendix C.

Most of the FE-models are correlating well with the real parts, but for some modes there are still problems. In a few models, different areas was stiffened or softened depending on the eigenfrequency or the shape of the altered mode.

A general observation was that the first mode in almost all models had a rather poor correlation when comparing the eigenfrequencies. A possible explanation is residual stresses built in during manufacturing.

The calculated modal damping factors can be found in Appendix D for all separate parts mentioned below.

5.1.1 Lid

The result from the experiments is visualized in Figure 5-1 where the frequency response is shown for all accelerometers used in the experiment. For the individual response of each accelerometer, see Appendix E1.

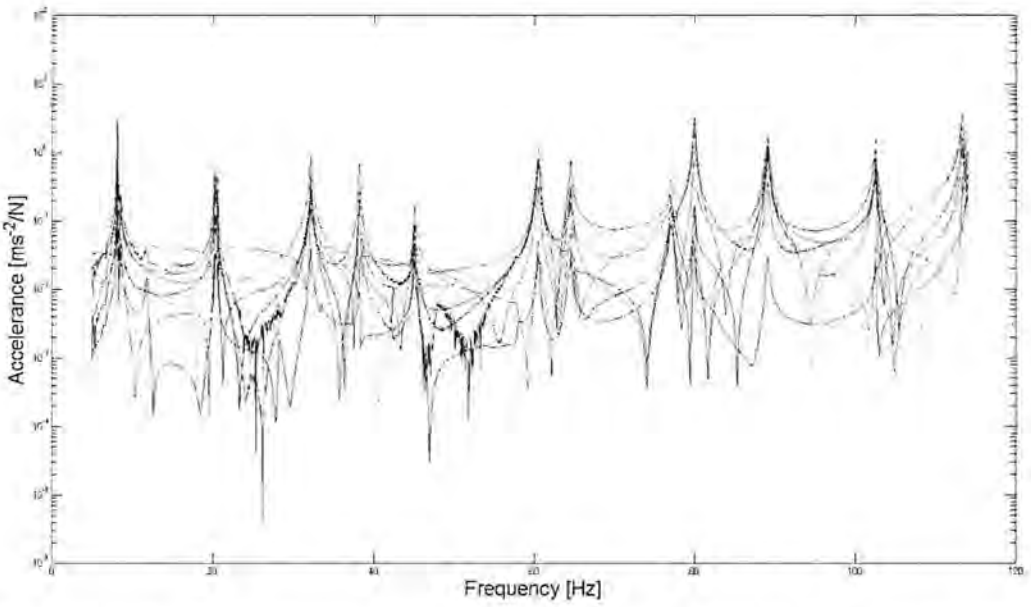

Figure 5-1: Frequency response plot for the lid for all measurement points used in EMA experiments.

As can be seen in Figure 5-1, there are a lot of modes within a short frequency range. A small peak shortly after the first clear resonance peak indicates that it is a mode at approximately 13 HZ. This mode could not be explained or found in the FE-model and is possibly from the

support condition. According to the MAC-numbers, mode one from the FE-model is the first mode measured in the experiment. Mode two in the FE-model correlates well with the measured mode at 20 Hz, see Figure 5-2.

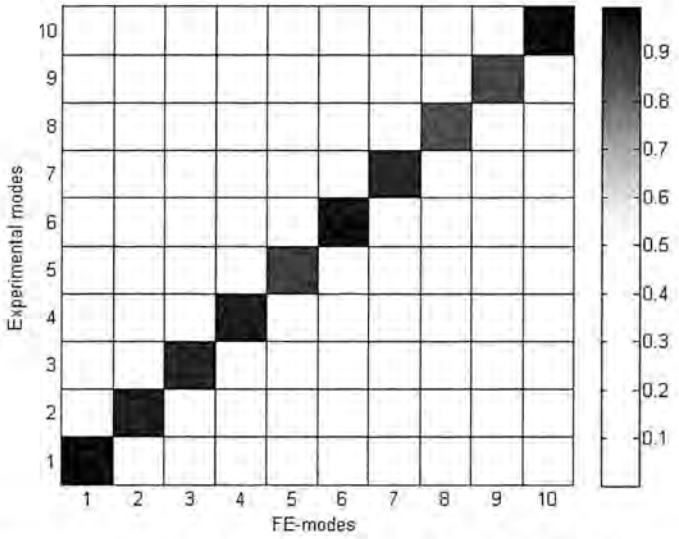

Figure 5-2: Graphical representation of the MAC-matrix for the lid.

In Figure 5-3, the direct accelerance is shown together with the calculated frequency response using modal superposition.

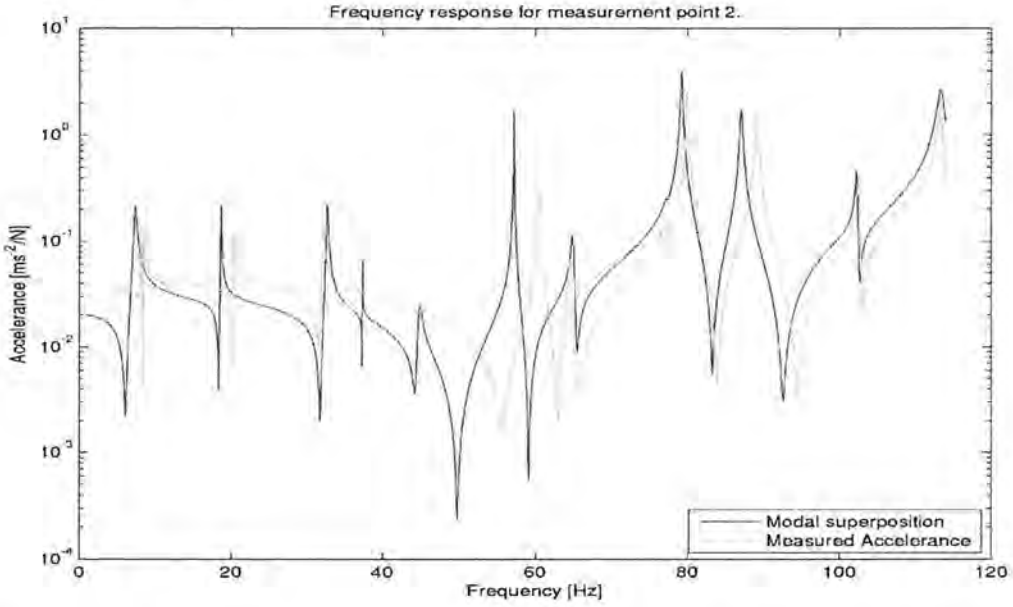

Figure 5-3: Frequency response from experimental and calculated data for measurement point number two, the direct accelerance.

The modes correlate quite well, except for contribution to the amplitudes of modes four to six, as seen in Figure 5-3. The responses for mode four and five fit the measured curve much better for the other measurement points, see Appendix E1. Mode six seems to contribute too much, indicating that its damping factor should be increased. Mode six is also the mode which has the worst correlation seen to the eigenfrequency, which is off with about 3 Hz, see Table 5-1.

Table 5-1: Measured and calculated eigenfrequencies for the lid.

Mode	1	2	3	4	5	6
EMA [Hz]	8.50	19.70	32.40	37.70	44.60	59.60
FEM [Hz]	7.41	18.72	32.32	37.54	44.96	56.57
Diff [%]	12.82	4.97	0.25	0.42	0.81	3.24
Mode	**7**	**8**	**9**	**10**	**11**	**12**
EMA [Hz]	64.55	77.45	79.60	88.70	102.20	114.35
FEM [Hz]	64.27	77.99	79.48	87.89	103.01	114.50
Diff [%]	1.19	0.70	0.15	0.91	0.79	0.13

The thickness and material properties used for the FE-model can be seen in Table 5-2.

Table 5-2: Updated material properties and thickness for the lid.

E [GPa]	ν	ρ [kg/m^3]	t [mm]
191	0.27	8055	0.806

5.1.2 Upper front plate

The result from the experiment is visualized in Figure 5-4 where the response from the upper front plate is shown for all measurement points. For the individual responses of each measurement point, see Appendix E2.

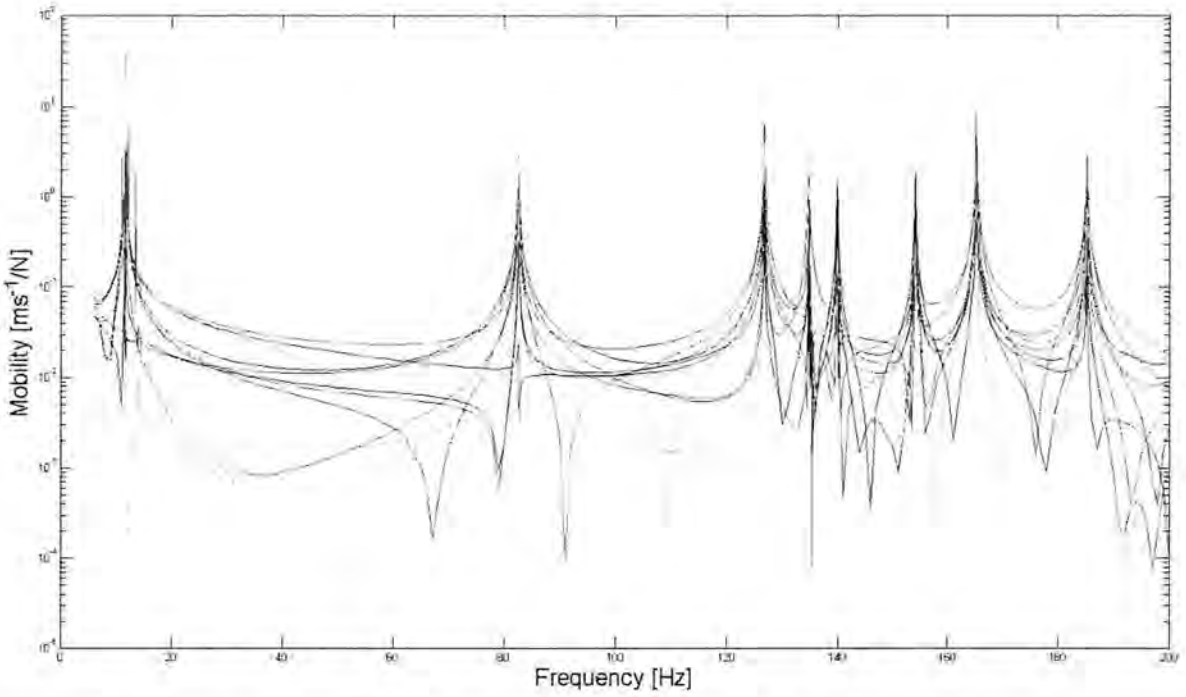

Figure 5-4: Frequency response plot for the upper front plate for all measurement points used in EMA experiments.

The correlation of the upper front plate was poor for the nominal FE-model. This can be seen in Figure 5-5 where the FE-model mode shapes are compared using MAC numbers before and after updates. The model was updated by changing thickness and material properties in different areas, where it would make a big impact on the modes which was altered.

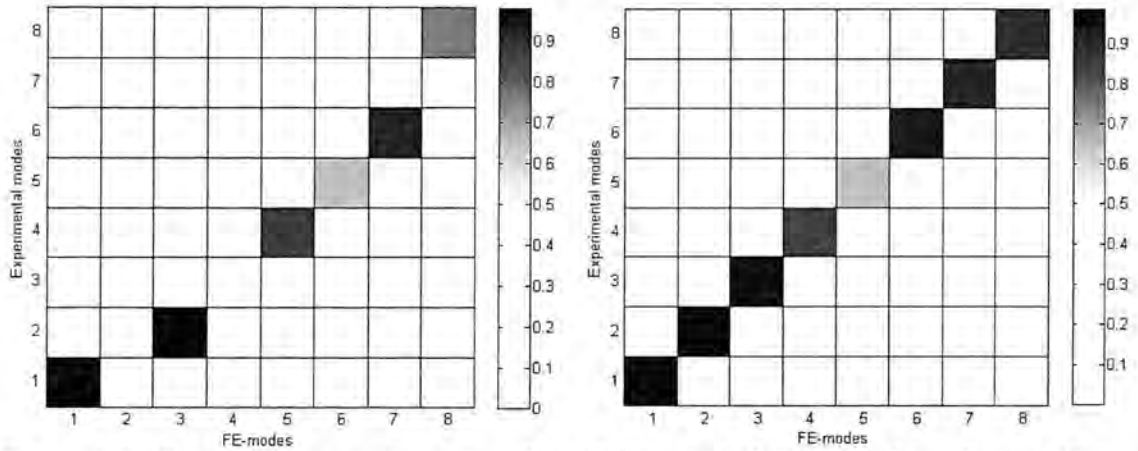

Figure 5-5: Graphical representations of the MAC-matrix before (to the left) and after model updates (to the right) for the upper front plate.

The updated areas can be seen in Figure 5-6 where the dark gray areas, pointed out as Zone 2, in the model have got new material parameters and thickness. Zone 1 which is the rest of the detail is kept constant. The result of the updates can be seen in Table 5-3.

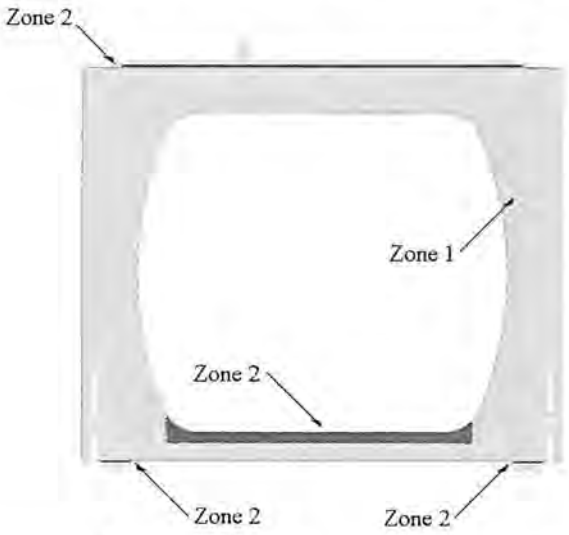

Figure 5-6: The upper front panel with dark gray areas, Zone 2, which shows where the material parameters and thickness were updated.

Table 5-3: Updated material properties and thickness for the upper front plate.

	E [GPa]	ν	ρ [kg/m^3]	t [mm]
Zone 1	210	0.32	7800	1.000
Zone 2	190	0.32	7900	0.800

Mode one and fives eigenfrequency did not correlate very well, as can be seen in Table 5-4 and Figure 5-7. Apart from mode one, mode five also had a low MAC number, only about 0.6. But since the mode shapes and the eigenfrequencies correlated well for mode two to four, it was decided not to do anything about the correlation of mode five since it was well above the range of interest (0-110 Hz).

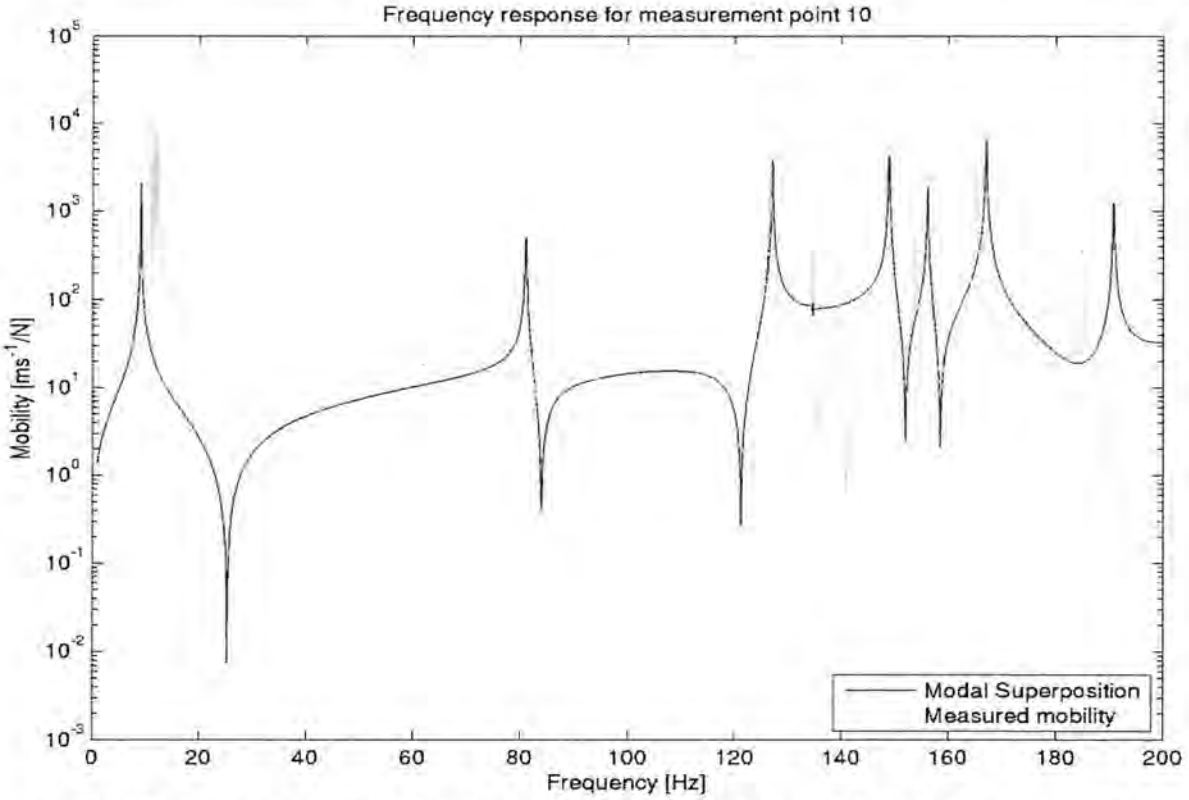

Figure 5-7: Frequency response from experimental and calculated data for measurement point ten, the direct accelerance of the upper front panel.

Table 5-4: Measured and calculated eigenfrequencies for the upper front plate.

		Initial model			Updated model		
Mode	**EMA [Hz]**	**Freq. [Hz]**	**Diff [Hz]**	**Diff [%]**	**Freq. [Hz]**	**Diff [Hz]**	**Diff [%]**
1	11.59	9.12	-2.47	-21.3%	8.98	-2.61	-22.5%
2	82.51	80.66	-1.85	-2.2%	80.59	-1.92	-2.3%
3	126.72	126.04	-0.68	-0.5%	126.08	-0.64	-0.5%
4	134.76	134.17	-0.59	-0.4%	134.13	-0.63	-0.5%
5	139.87	148.99	9.12	6.5%	148.61	8.74	6.2%
6	154.11	156.70	2.59	1.7%	155.67	1.56	1.0%
7	165.19	169.45	4.26	2.6%	166.30	1.11	0.7%
8	185.09	197.45	12.36	6.7%	189.39	4.30	2.3%

5.1.3 Lower Front plate

The result from the experiments is visualized in Figure 5-8 where the response is shown for all measurement points. For the individual response of each point, see Appendix E3.

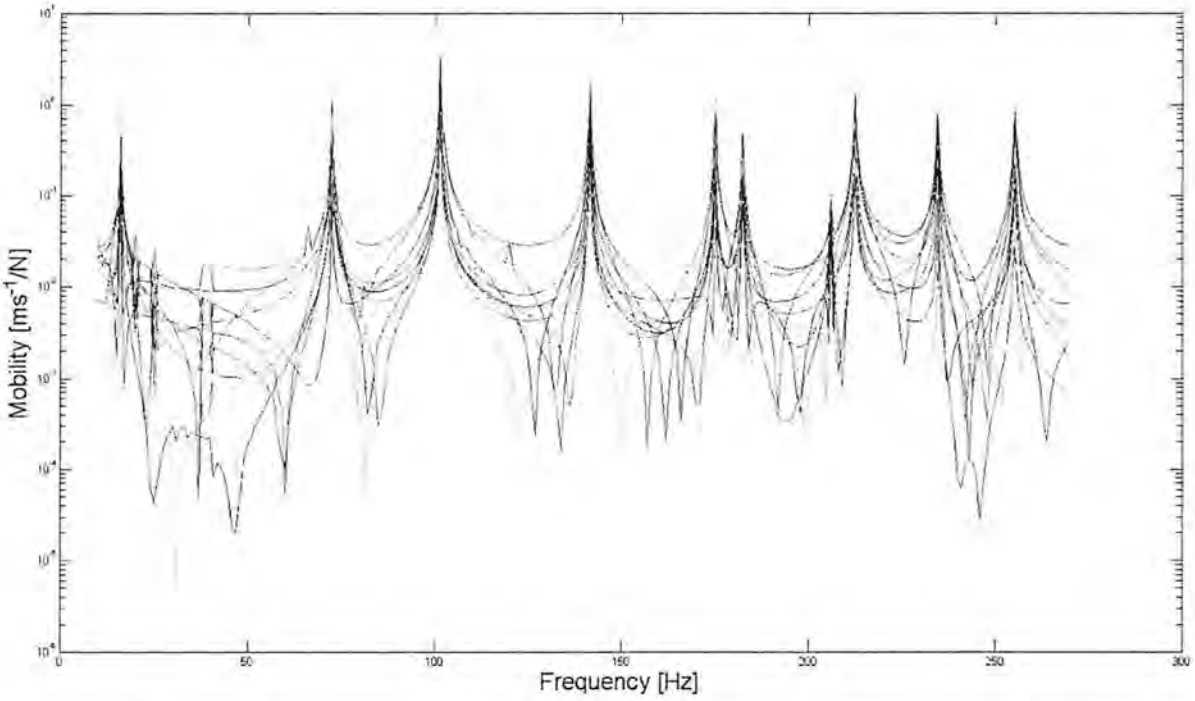

Figure 5-8: Frequency response plot of the lower front plate for all measurement points used in EMA experiments.

As can be seen there is some irregularities to the response around 30Hz and on some other places where the curve spikes. This does not indicate eigenfrequencies at those places, but rather that there has been noise introduced by the LDV equipment. The MAC-matrix, see Figure 5-9, indicates that all FE-modes up to 260 Hz has been properly identified.

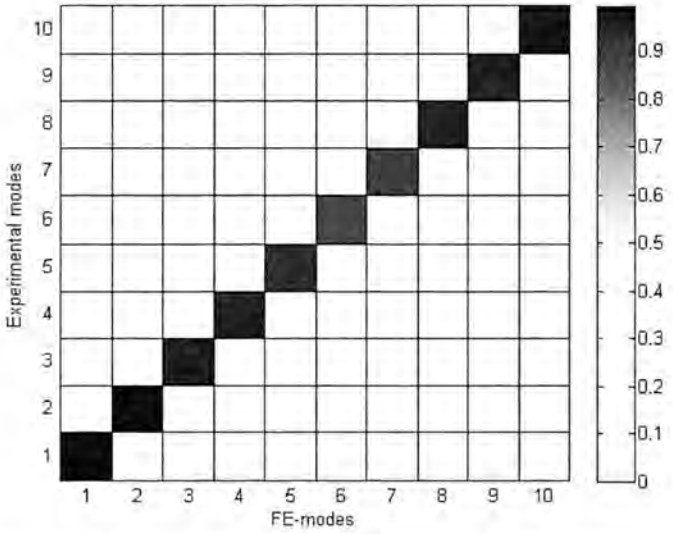

Figure 5-9: Graphical representation of the MAC-matrix for the lower front plate.

The eigenfrequencies of the updated model is compared to the real part in Table 5-5. The resulting frequency response plot compared to the measured response in measurement point five is visualized in Figure 5-10.

Table 5-5: Measured and calculated eigenfrequencies for the lower front plate.

Mode	1	2	3	4	5	6	7	8	9	10
EMA [Hz]	15.96	72.40	101.37	141.67	175.03	182.31	206.03	212.40	234.47	255.32
FEM [Hz]	17.78	70.39	98.55	140.84	176.82	182.69	205.63	213.25	234.81	255.20
Diff [%]	11.40	2.78	2.78	0.59	1.02	0.21	0.19	0.40	0.15	0.05

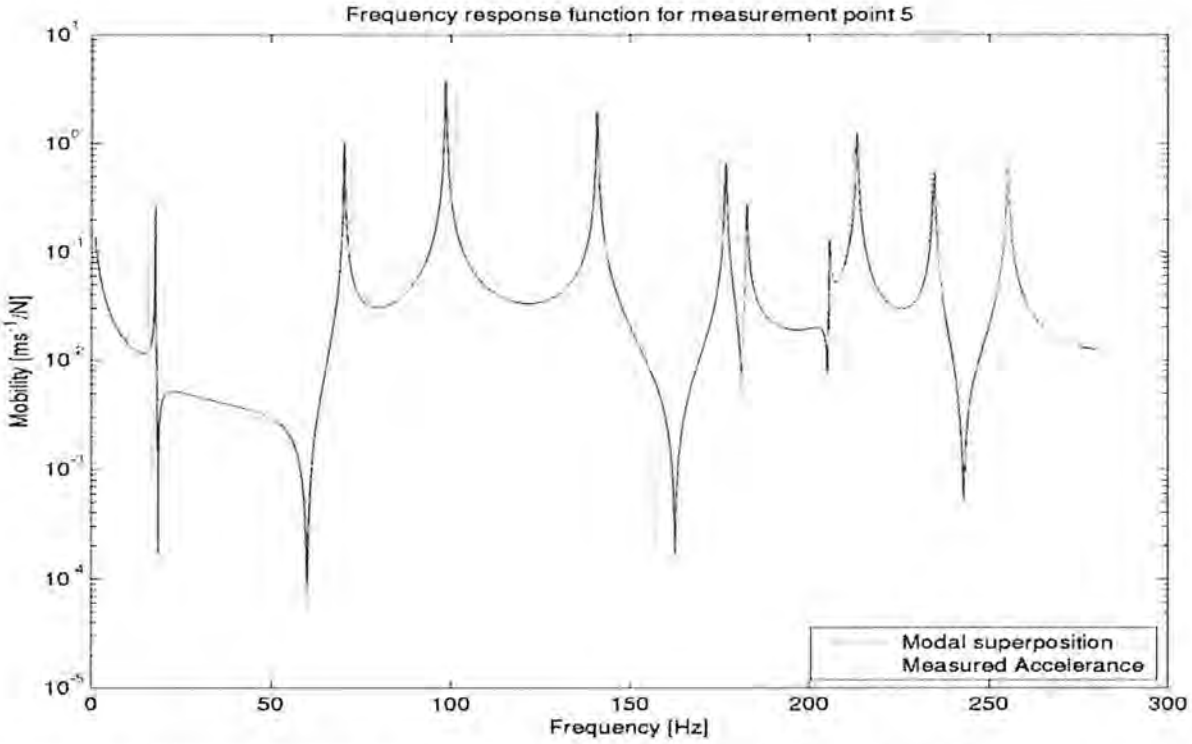

Figure 5-10: Frequency response from experimental and calculated data for measurement point number five, the direct mobility of the lower front plate.

The first eigenfrequency is, as with most of the other parts, quite badly correlated with the FE-model. The rest of the eigenfrequencies correlates well with the FE-model. The thickness and material properties used for the model can be seen in Table 5-6. The curve created using modal superposition fits very well as can be seen for measurement point five in Figure 5-10. The other measurement points frequency response and the corresponding calculated curves can be found in Appendix E3.

Table 5-6: Updated material properties and thickness for lower front plate

E [GPa]	ν	ρ [kg/m^3]	t [mm]
267	0.25	8122	0.723

5.1.4 Electric bridge

The result from the experiments is visualized in Figure 5-11 where the response is shown for all measurement points. For the individual response of each measurement point, see Appendix E4.

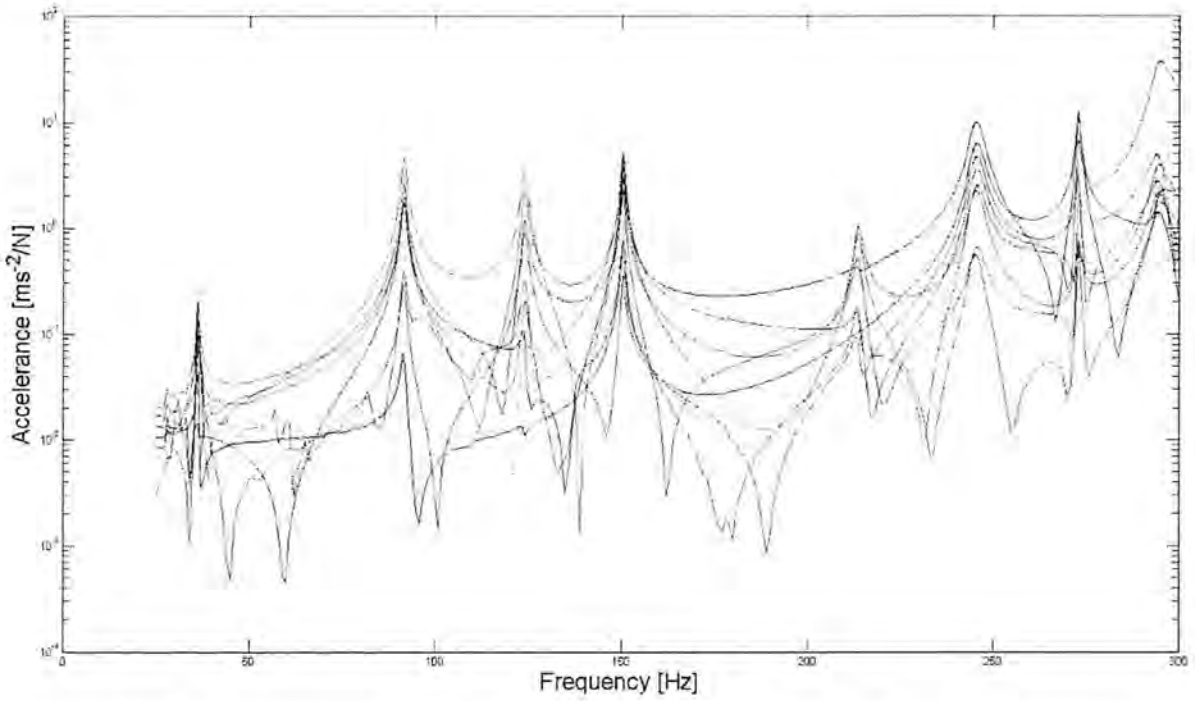

Figure 5-11: Frequency response plot for all measurement points on the electric bridge.

This turned out to be one of the most difficult models to get a good correlation to the test subject. For the initial model the MAC matrix, see Figure 5-14, showed that the mode shapes correlated well, but the eigenfrequencies did not. In order to lower some eigenfrequencies and raise others, the model had to be updated using different thicknesses in different areas of the model. The areas are highlighted with different tones of gray and pointed out in Figure 5-12 as different zones. The original properties are Zone 1.

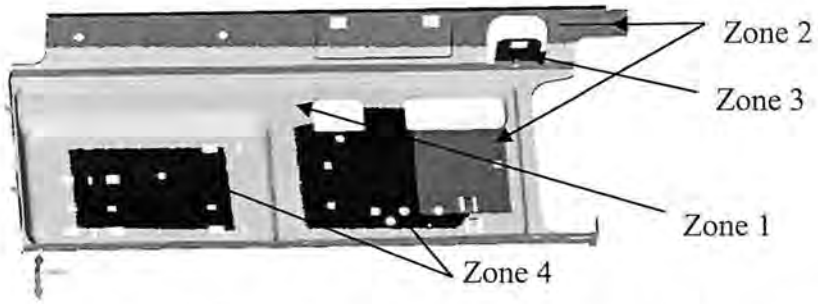

Figure 5-12: The electric bridge with different shades of gray areas showing where the plate thickness was updated.

Modes four and six were quite similar regarding which areas the model displaced, see Figure 5-13. This meant that it was very hard to get a good correlation of the eigenfrequency for both of these modes at the same time, since changing the thickness always affected both modes in

dissimilar ways. The best overall results were obtained using the material parameters and thickness as described in Table 5-7.

Figure 5-13: Iso surfaces showing the mode shape of the electric bridge. Mode four to the left and mode six to the right.

Table 5-7: Updated material parameters and thickness for the different zones in the electric bridge.

	E [GPa]	ν	ρ [kg/m^3]	t [mm]
Zone 1	176	0.27	8300	0.909
Zone 2	176	0.27	8300	1.150
Zone 3	176	0.27	8300	1.070
Zone 4	176	0.27	8300	0.600

As can be seen in Figure 5-14 and Table 5-8 the updates have given better correlation, both for the mode shapes and the frequencies at which they occur.

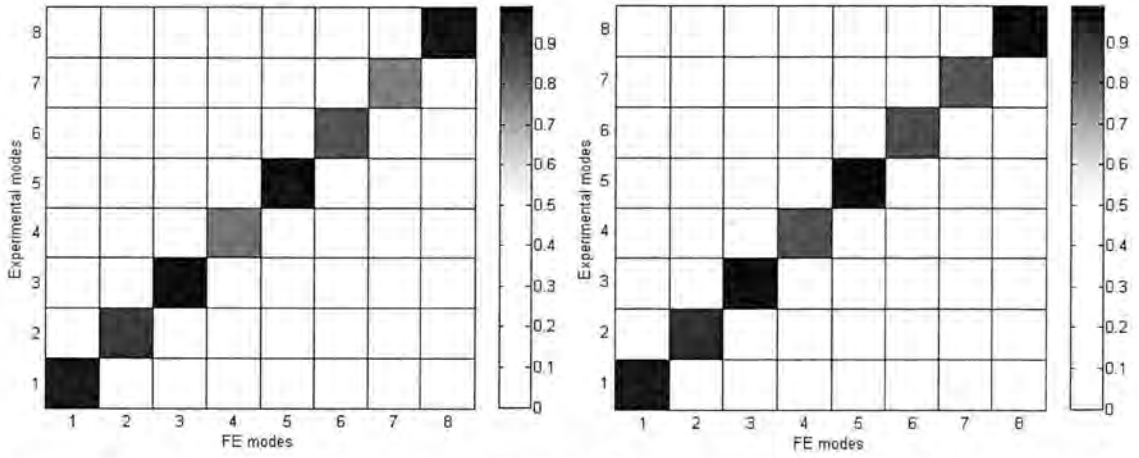

Figure 5-14: Graphical representations of the MAC-matrix before (to the left) and after model updates (to the right) of the electric bridge.

In Figure 5-14 for the updated model, the poorest MAC correlation is between the seventh pair of modes at about 270 Hz. This mode contributes most to the poor fit of the calculated frequency response as can be seen in Figure 5-15. This is also the case for the rest of the measurement points for this mode, see Appendix E4.

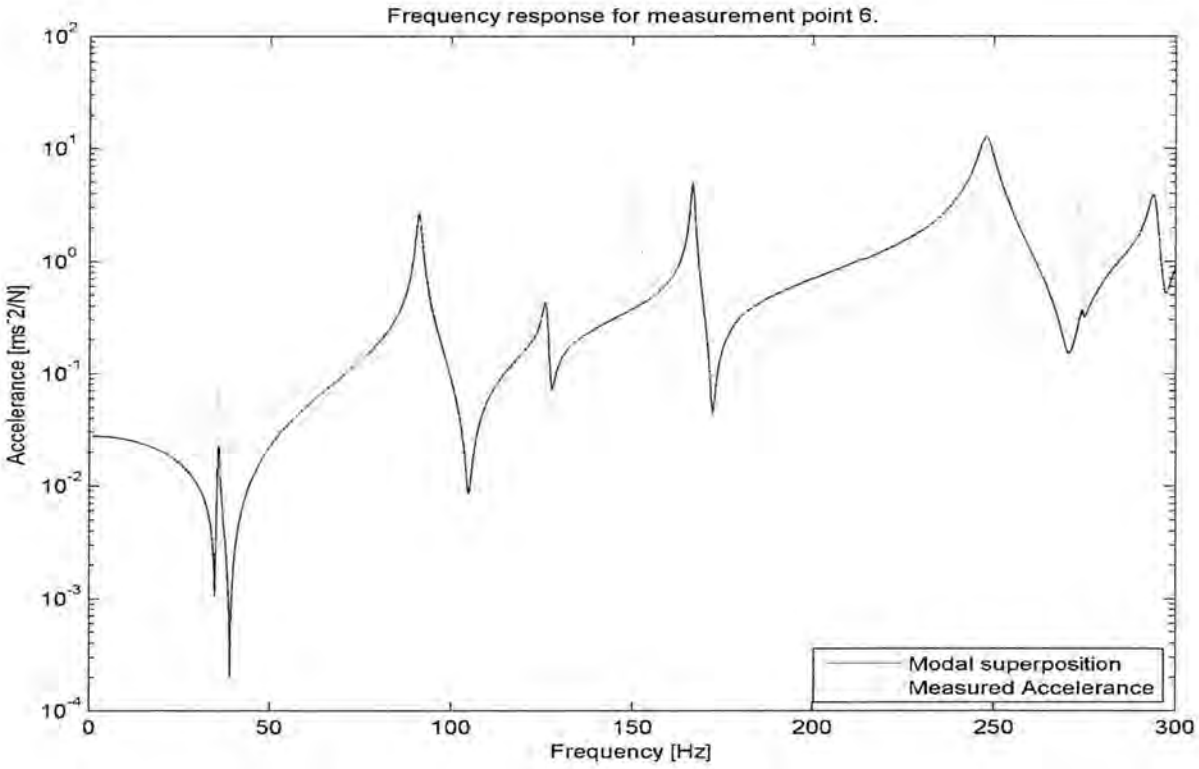

Figure 5-15: Frequency response from experimental and calculated data for measurement point number six, the direct accelerance of the electric bridge.

Table 5-8: Measured and calculated eigenfrequencies for the electric bridge.

Mode	EMA [Hz]	Initial model			Updated model		
		Freq. [Hz]	Diff [Hz]	Diff [%]	Freq. [Hz]	Diff [Hz]	Diff [%]
1	36.23	36.86	0.63	1.7	35.82	-0.41	-1.1
2	91.65	96.77	5.12	5.6	91.06	-0.59	-0.6
3	124.09	128.95	4.86	3.9	126.11	2.02	1.6
4	150.43	178.91	28.48	18.9	166.57	16.14	10.7
5	213.64	216.57	2.93	1.4	213.77	0.13	0.1
6	246.55	255.61	9.06	3.7	247.79	1.24	0.5
7	273.00	298.43	25.43	9.3	274.30	1.30	0.5
8	293.58	306.60	13.02	4.4	294.20	0.62	0.2

5.1.5 Back plate

The result from the experiments is visualized in Figure 5-16 where the response from the back plate is shown for all measurement points. For the individual response of each measurement point, see Appendix E5.

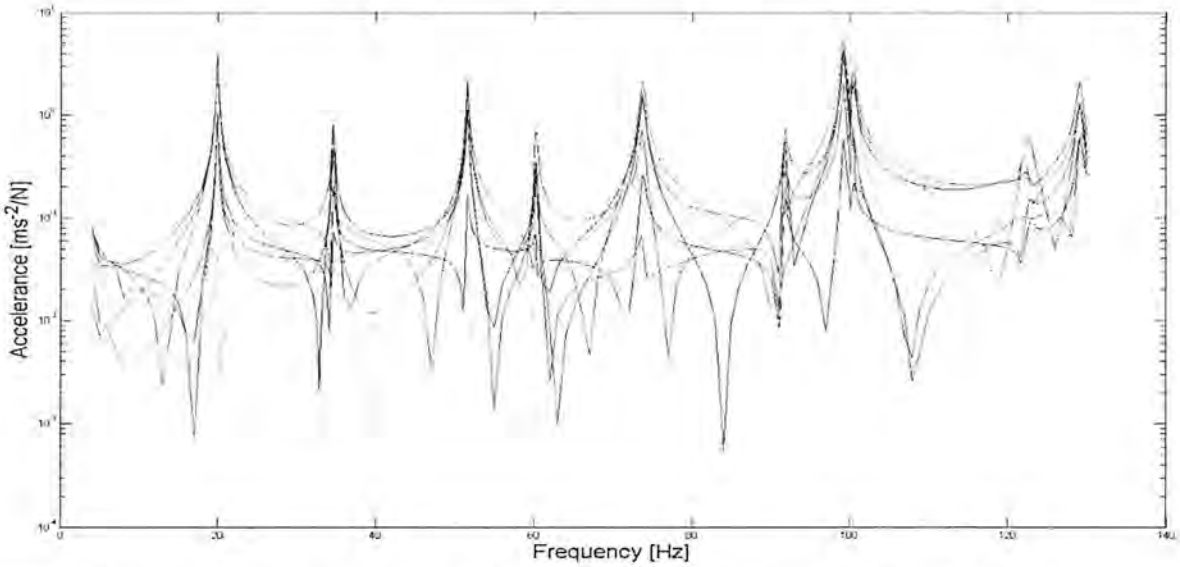

Figure 5-16: Frequency response plot for all measurement points on the back plate

Also for the back plate individual areas of the model had to be updated with different thicknesses in order to get a good correlation of the eigenfrequencies. All these areas can be seen in Figure 5-17 where they are highlighted in different tones of darker grey and have been pointed out as zones. The changes in nominal thickness of these areas can be seen in Table 5-9.

Table 5-9: Material parameters and thickness for the different zones in the back plate.

	E [GPa]	ν	ρ [kg/m^3]	t [mm]
Zone 1	188	0.3	8416	0.500
Zone 2	188	0.3	8416	0.460
Zone 3	188	0.3	8416	0.680

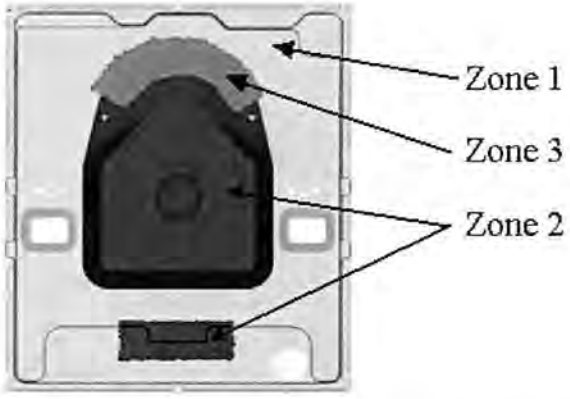

Figure 5-17: The back plate with dark gray areas which shows where the plate thickness was changed.

A problem with this model is the poor correlation of the first two modes as can be seen in Figure 5-18 and Table 5-10. According to the MAC correlation, see Figure 5-19, the mode

shapes correlates well. As mentioned before, the first mode often correlates poorly, but the second mode usually correlates better. It could be that this part also is affected by the oil canning effect, see chapter 3. This was unknown prior to the experiments and since the data from the first shaker position looked really bad, see Appendix E5, most of the data from that measurement was not considered.

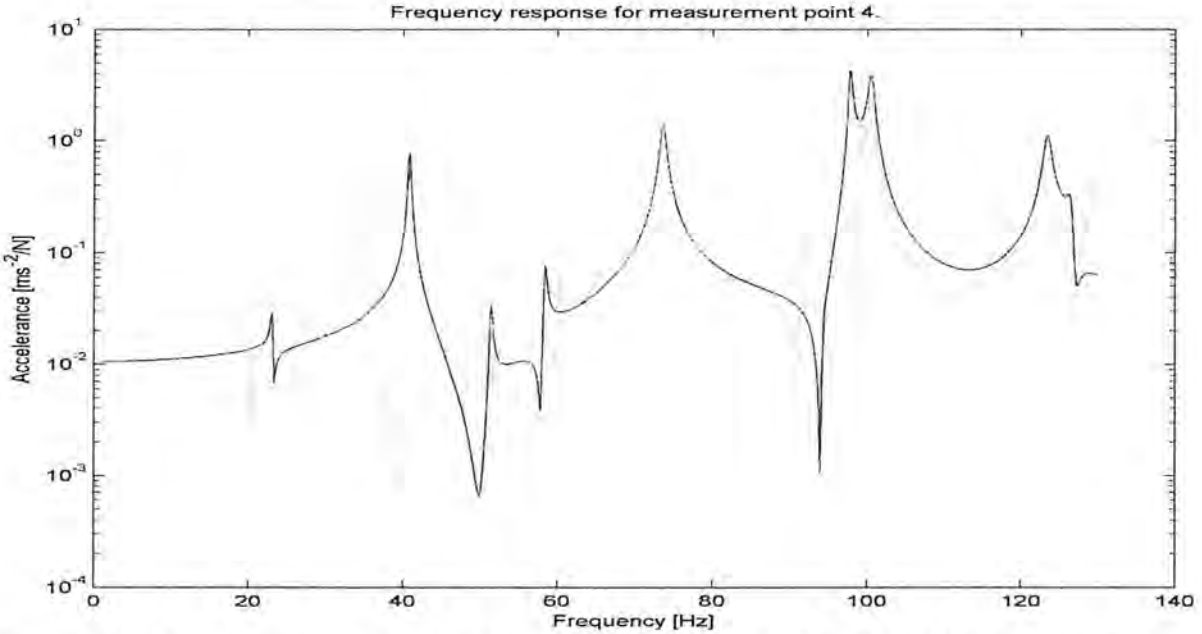

Figure 5-18: Frequency response from experimental and calculated data for measurement point number four, the direct accelerance of the back plate.

Table 5-10: Measured and calculated eigenfrequencies for the back plate.

		One property			Two properties		
Mode	**EMA [Hz]**	**Freq. [Hz]**	**Diff [Hz]**	**Diff [%]**	**Freq. [Hz]**	**Diff [Hz]**	**Diff [%]**
1	19.95	22.76	2.81	14.1%	23.90	3.95	19.8%
2	34.65	40.83	6.18	17.8%	40.73	6.08	17.5%
3	51.55	52.29	0.74	1.4%	51.17	-0.38	-0.7%
4	60.25	57.81	-2.44	-4.0%	58.22	-2.03	-3.4%
5	73.70	70.75	-2.95	-4.0%	72.25	-1.45	-2.0%
6	91.80	81.10	-10.70	-11.7%	94.34	2.54	2.8%
7	99.30	94.42	-4.88	-4.9%	98.35	-0.95	-1.0%
8	100.60	97.78	-2.82	-2.8%	100.28	-0.32	-0.3%
9	122.60	112.67	-9.93	-8.1%	122.49	-0.11	-0.1%
10	129.20	119.99	-9.21	-7.1%	127.70	-1.50	-1.2%

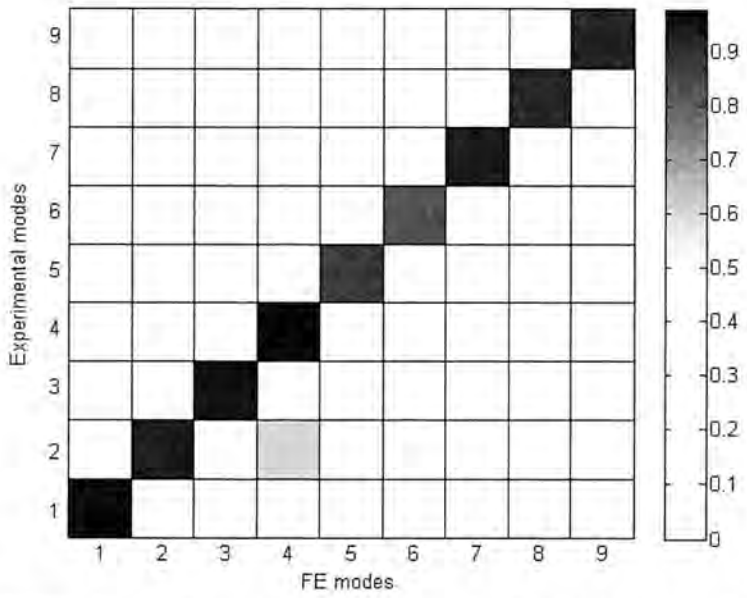

Figure 5-19: A graphical representation of a MAC-matrix of the back plate.

5.2 Assembled steel structure

The result from one of three experiments is visualized in Figure 5-20. The response of the steel shell when applying the force on the lid in stinger position one, see Figure 4-7, is shown. The individual responses for each measurement point and for other stinger positions can be found in Appendix E6.

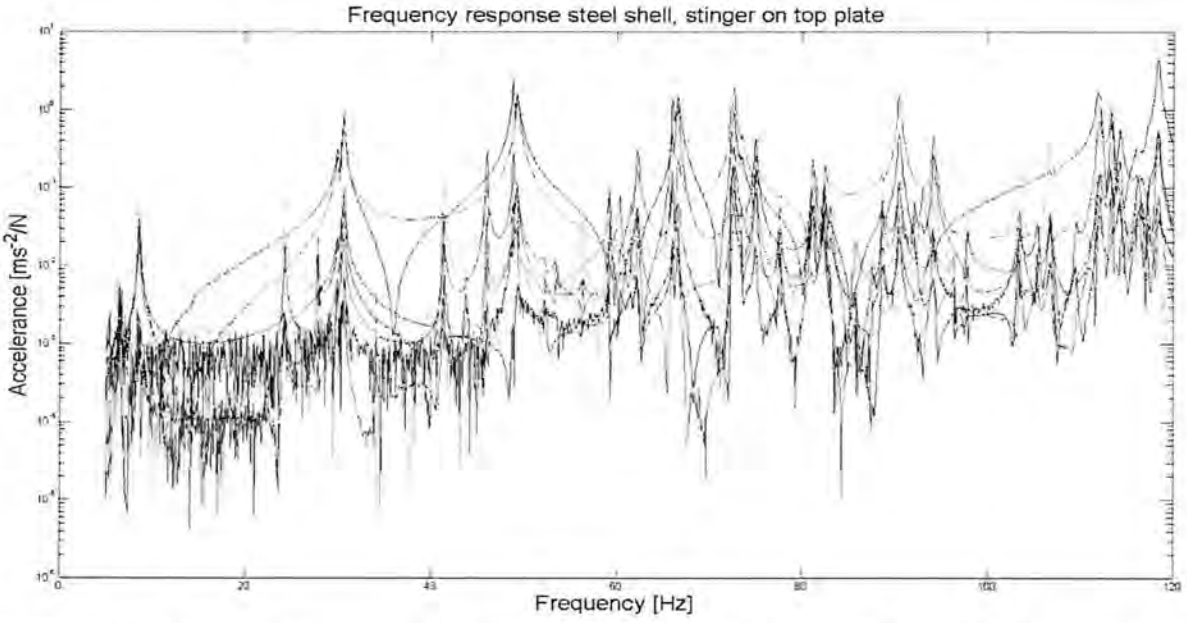

Figure 5-20: Frequency response plot for all measurement points on the steel shell when applying force in stinger position one.

Since the steel shell was heavy, more fishing lines were used to suspend the structure than for each separate part. This made the highest rigid mode visible around 6 HZ, see Figure 5-20. To assure that it was a rigid and not an elastic mode, the fishing lines were modeled as springs

attached to the suspension points on the model. An analysis based on that model showed that the rigid modes could indeed reach 6 Hz.

Since there were as many as 41 modes between 15 Hz and 110 Hz, the system identification had to be done in steps of 30 Hz for practical reasons. The resulting MAC correlation numbers between the FE-model modes and the modes found using EMA can be found in Table 5-11 that includes comments about why certain modes cannot be properly identified.

The validation shows that it correlates rather well for the modes up to around 60Hz. After that complex mode shapes start to form which makes it harder to identify the modes. However, well correlating modes can also be found at higher frequencies. These are the more stiff parts in the structure that deforms locally, with the rest of the steel shell more or less stationary.

There are modes that cannot be identified at all when doing the modal analysis. These are modes 1, 8, 12, 15, 22, 23, 24, 36 and 41. By inspection, some conclusions can be drawn to why these cannot be identified in the model.

Mode 22, 23, 36 and 41 are modes where the electric bridge and the upper front plate will deform locally while the rest of the steel shell will be stationary. On these parts there were no accelerometers placed, see Figure 4-7. This means that the machine is under-sampled and that the measurement points are far too few to properly identify all the modes. This is also the reason why the MAC-matrix is not as heavy on the diagonal as it should.

Mode 8 and 24 are modes, in which the model order in the system identification was set too low to properly identify them. Even though the order was up to 100, the noise in the measurement signal together with the weak response in the modes disturbed the identification. In order to identify these modes, the displacement mode vector from the experiment was by comparison with the displacement mode vector from the FE-model judged likely that these two modes are the ones stated in Table 5-11.

For mode one there is no explanation to why it cannot be identified. This mode should be easy to identify since it is a local mode in the lid, see Figure 5-21, but for some reason this has not even been excited at all in the experiments. When examining modes 12 and 15 it is realized that these modes could be missed due to the placements of the stinger.

Figure 5-21: Iso surfaces showing the first mode for the steel shell.

As can be seen in Table 5-11, the eigenfrequencies of the FE-model are not in very good agreement with those retrieved using EMA. An attempt was made to fix this using the modeled connectors between the parts. However these modifications turned out to have a very small effect on the shells behavior. In Figure 5-22 a comparison of analysis using the typical Young's modulus and half the typical Young's modulus can be seen. It shows that the only mode affected by this was mode ten, and the effect was small.

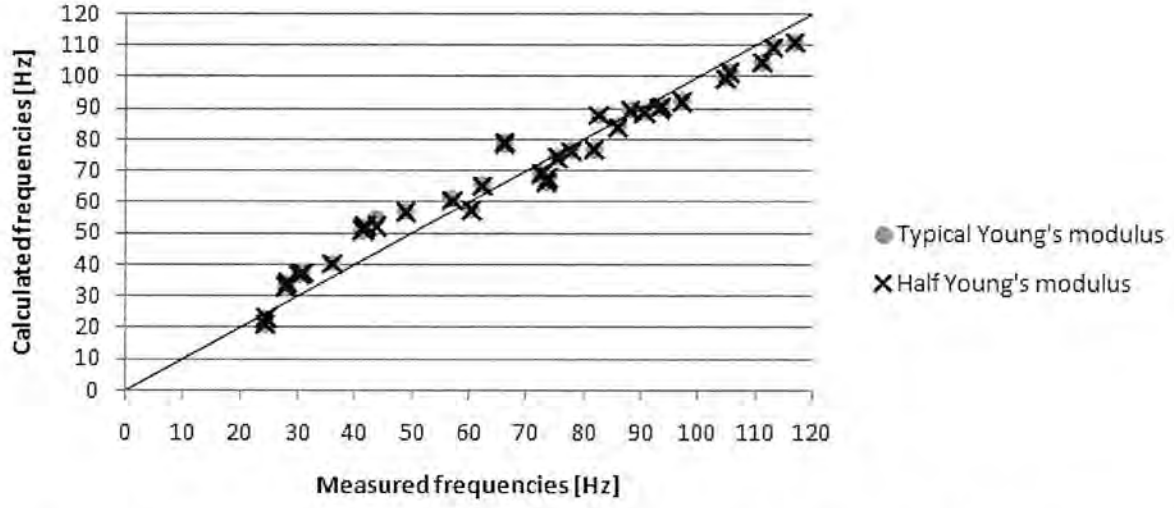

Figure 5-22: A comparison in frequencies between two sets of Young's modulus in connector properties between steel shell parts.

Table 5-11: Correlation between measured and calculated eigenfrequencies using MAC numbers.

Mode	Frequency EMA	Frequency FEM	MAC-number	Comments
1	-	18.43	-	No correlation
2	24.31	21.32	0.9982	
3	24.42	23.17	0.9981	
4	27.77	33.10	0.9901	
5	27.98	34.27	0.9934	
6	30.21	36.89	0.9914	
7	30.78	37.49	0.9879	
8	35.94	40.73	-	Too low order in system identification
9	41.33	50.98	0.9519	
10	41.62	52.12	0.9664	
11	43.70	54.75	0.5584	
12	-	55.47	-	No correlation
13	48.87	56.91	0.9417	
14	60.38	57.60	0.9636	
15	-	58.61	-	No correlation
16	56.96	61.33	0.7594	
17	62.34	65.69	0.7568	
18	73.35	66.33	0.6785	
19	73.79	68.13	0.6432	
20	72.48	69.07	0.8397	
21	72.58	69.35	0.8214	
22	-	72.33	-	Electric bridge deforming, too few MP
23	-	73.77	-	Upper front plate deforming, too few MP
24	75.20	74.24	-	Too low order in system identification
25	77.71	76.65	0.7237	
26	81.65	76.88	0.6627	
27	66.11	78.66	0.5909	
28	66.17	79.09	0.6016	
29	85.78	84.11	0.5226	
30	82.46	87.88	0.6213	
31	90.50	88.79	0.8431	
32	88.16	89.27	0.7003	
33	92.98	89.93	0.9519	
34	93.45	90.92	0.9924	
35	96.99	92.21	0.9118	
36	-	96.33	-	Upper front plate deforming, too few MP
37	104.72	99.57	0.5437	
38	105.33	101.62	0.5775	
39	111.10	104.67	0.6619	
40	113.03	109.67	0.8555	
41	-	110.13	-	Electric bridge deforming, too few MP

5.3 Spin up tests

A selection of results from the experiments and the simulations are presented here. To see all measured data compared with the simulated data for all measurement points and all experiment configurations see Appendix G.

5.3.1 Modal analysis

Frequencies and mode shapes are obtained when having the bottom of the feet fixed. These modes indicate where to expect resonance peaks in the shell during running of harmonic analysis. The three first modes are the drum moving up and down, back and forth and sideways. The eigenfrequency of these modes are decided by the bending and spring stiffness of the spring legs. The rest of the modes up to 33 Hz deforms the steel shell whilst the inside parts are stationary. The steel shell parts are unaffected by the change in bending and spring stiffness in the legs. In Table 5-12 the eigenfrequencies of the model can be found and in Appendix G the mode shapes is visualized.

Table 5-12: Eigenfrequencies for the entire machine fixed under the feet.

	Eigenfrequency [Hz]
Mode 1	2.93
Mode 2	6.88
Mode 3	7.55
Mode 4	17.49
Mode 5	18.55
Mode 6	21.29
Mode 7	26.51
Mode 8	29.50
Mode 9	33.12
Mode 10	33.77

5.3.2 Acceleration data

In all experiments the accelerometers placed on the drum container showed consistent data when the drum was loaded with an unbalance. From this it can be concluded that the different setups of the machine have little impact on the movements of the drum container. A comparison between the accelerations in measurement point N6, N7 and N8 for experiment five and six can be seen in Figure 5-23 as an example of the consistent acceleration data in the drum. These are points measuring in the X-, Y- and Z-direction, see Figure 4-9.

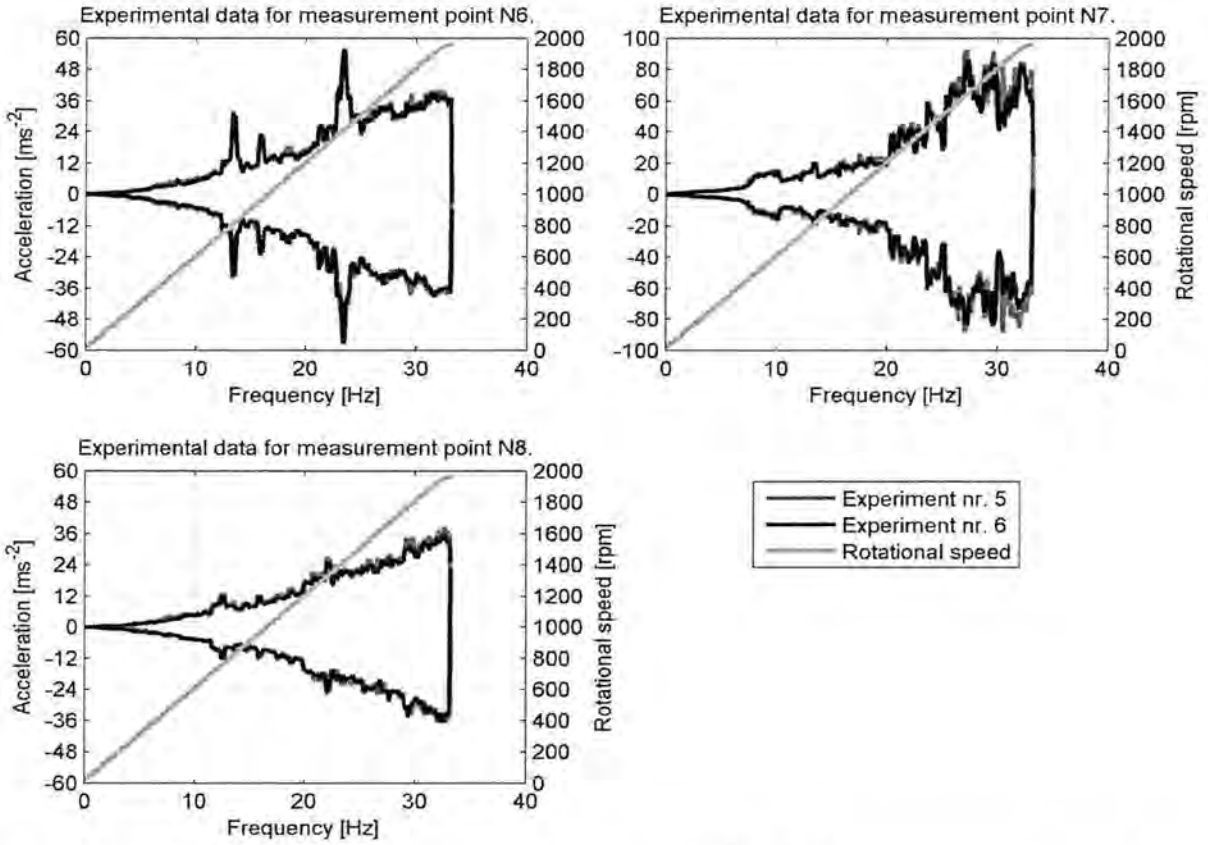

Figure 5-23: Accelerations in measurement point N6, N7 and N8 for experiment five and six.

In Figure 5-24, a comparison between experiment one and two shows the influence the unbalance weight has on the accelerations for measurement point T8. As expected the amplitude is higher in the drum when using the unbalance. Also the accelerations in the steel shell increases using the unbalance. The influence is not as strong as it is for the drum, but at the resonance peaks the difference is very clear as can be seen for measurement point T4 in Figure 5-25.

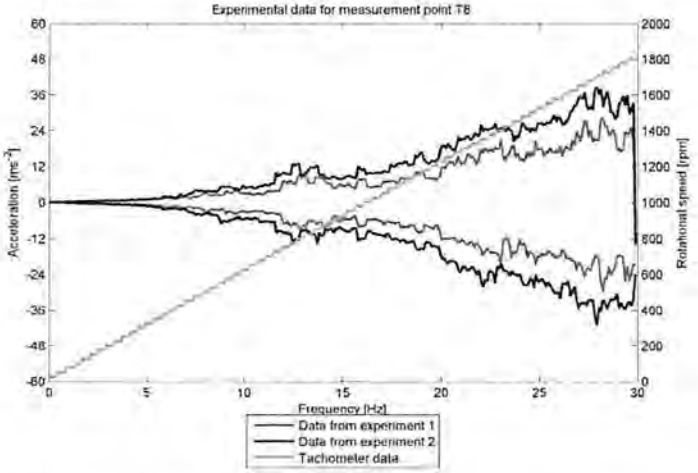

Figure 5-24: Accelerations in measurement point T8 for experiment one and two.

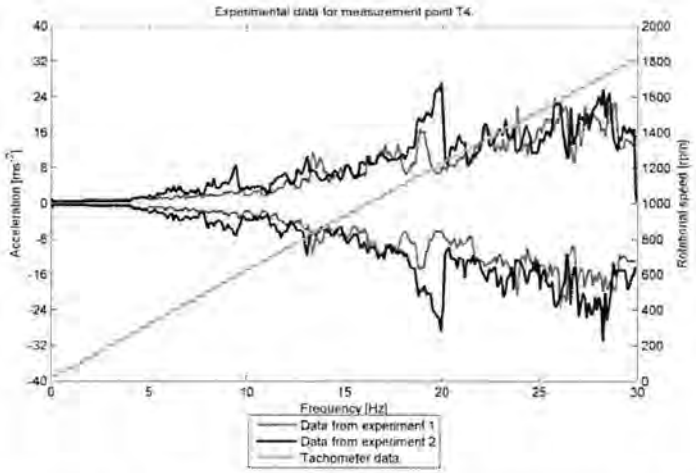

Figure 5-25: Comparison between experiment one and two in measurement points T4.

The second experiment was conducted on a table instead of the ground. This turned out to have a small effect on the acceleration curves when comparing them to the experiments conducted on the floor, see Figure 5-26. Therefore the results from this experiment are not covered here, instead see Appendix G. Also, an interesting speed range above 30Hz is not present in the data from experiments one and two since those were only run up to 1800 rpm.

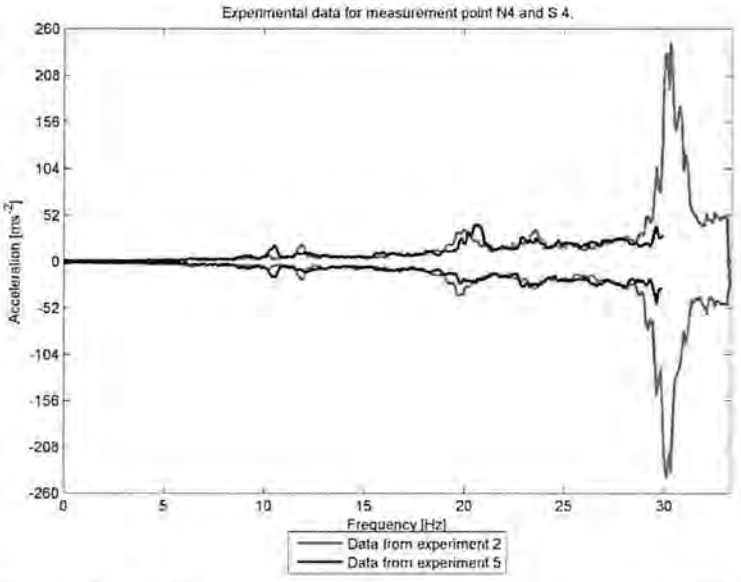

Figure 5-26: Comparison between experiment two and five for measurement point N4 and S4.

5.3.2.1 Difference between rubber and steel bushings under spring leg

The accelerations in the steel shell show that the main difference between using the rubber and steel bushings is that the amplitudes at resonance frequencies is higher when using the steel bushings. Also more resonances in the steel shell seem to be excited when using the steel bushings. This can be seen as peaks in the measured data at approximately 19 and 23 Hz in Figure 5-27.

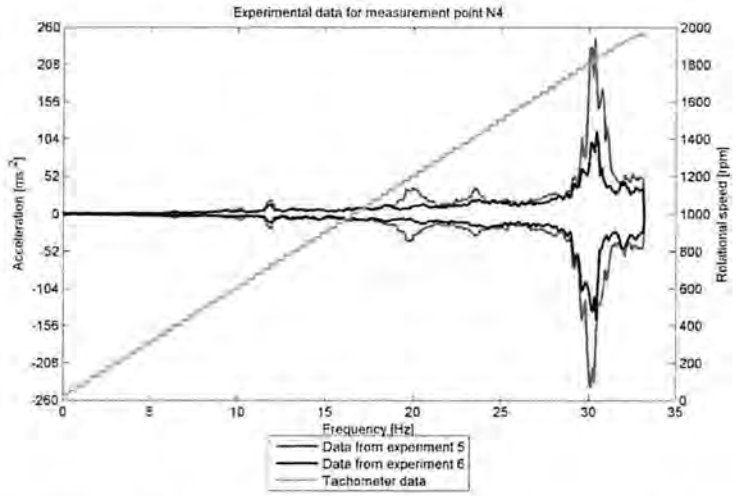

Figure 5-27: A comparison between measured data using rubber and steel bushings for measurement point N4.

5.3.2.2 Difference in forces under feet when changing damping under rig feet

The main difference between using steel and rubber soles under the feet of the steel rig when measuring the force, is that the peaks around 17 Hz has lower amplitude and is shifted upwards in frequency, see Figure 5-28. Also the peaks around 20 Hz shifted upwards in frequency, but the amplitude stayed at relatively the same value. The rest of the force curves are more or less unaffected by the change in rig feet.

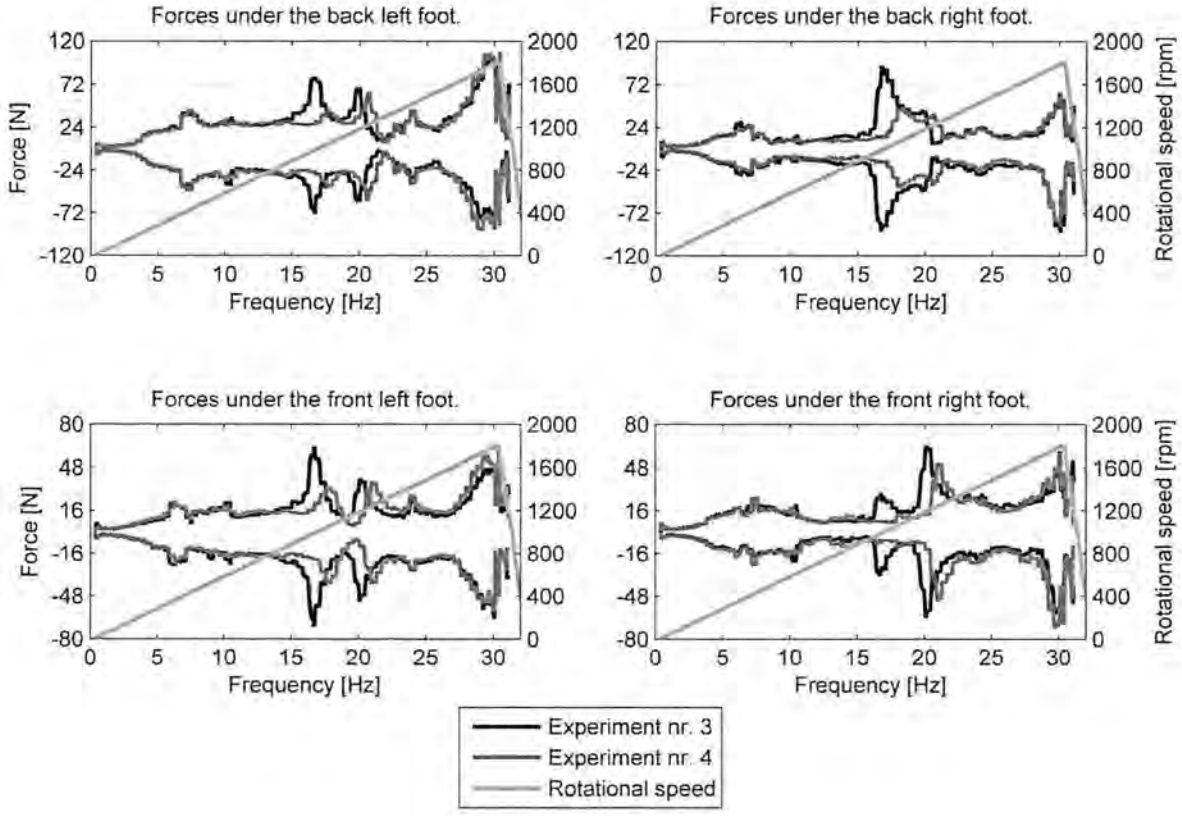

Figure 5-28: Forces under the feet of the washing machine in experiment three and four.

5.3.2.3 Accelerations in steel shell during spin up

Here the accelerations in the steel shell are presented for only a few measurement points. These points give a clear image of how the simulated data fits the measured. The rest of the acceleration points can be seen in Appendix G.

The simulated accelerations in the side plates capture two of the resonance peaks at approximately the correct position. The accelerations in the side plate were also the ones most similar to the measured data. In Figure 5-29 the acceleration for measurement point N4 from experiment six is presented together with the simulated data.

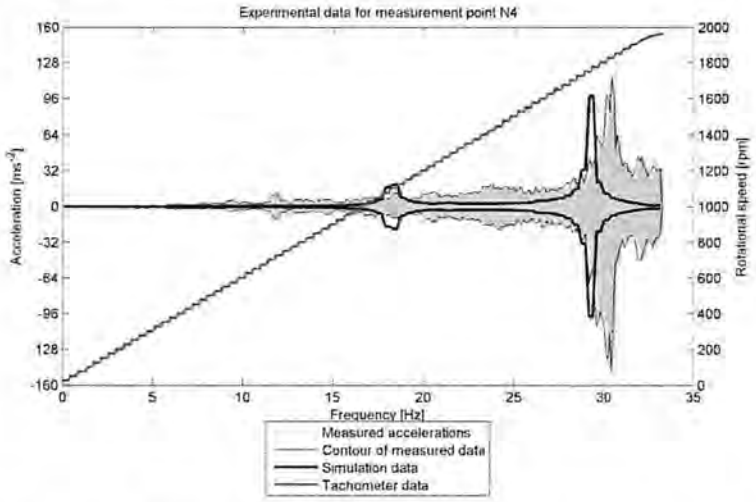

Figure 5-29: The acceleration curve from experiment six together with the simulated acceleration curve for measurement point N4.

Parts of the machine where the acceleration curve does not correlate well are the lid, back plate, and upper front plate. It seems as there are not enough forces transmitted from the inside parts through the contact points to all parts in the steel shell. In Figure 5-30 the acceleration curve for both a measurement point on the back plate, N1, and on the lid, N10, can be seen. The point in the back plate shows resonance peaks at some of the peaks in the measured data, but the amplitudes are too low. For the lid there is almost no response in the simulated acceleration curve.

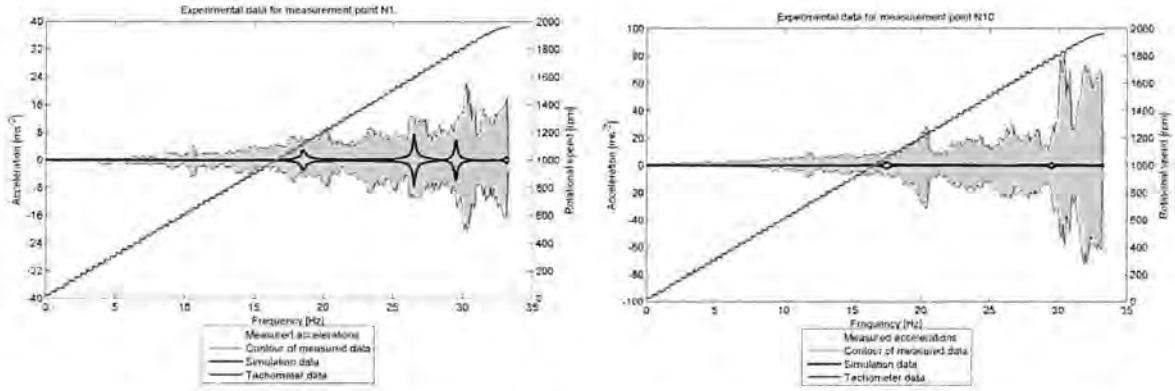

Figure 5-30: Acceleration in measurement points N1 (to the left) and N10 (to the right) for experiment six.

For all measurement points in the steel shell, the simulated accelerations amplitudes are too low in the range between resonance peaks. The measurement point N8, located on the

container and measuring in the Z-direction, can be seen in Figure 5-31. It can be seen that the simulated data follows the measured curve rather well, indicating that the forces applied in the model is correct, but that forces do not transmit properly to the shell parts.

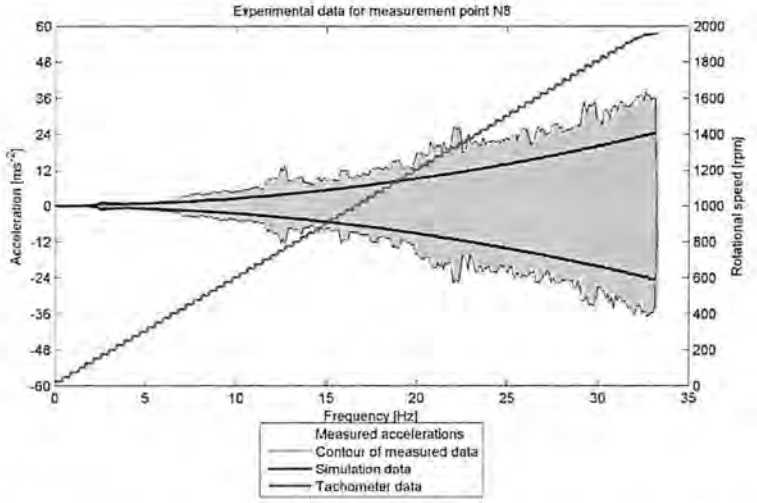

Figure 5-31: The acceleration curve from experiment five together with the simulated acceleration curve for measurement point N8.

5.3.2.4 Forces under feet during spin up

A comparison of the forces under the feet between experiments and simulations can be seen for experiment three in Figure 5-32 and for experiment four in Figure 5-33. The figures show that the correlation of the simulated data against the measured data is rather poor.

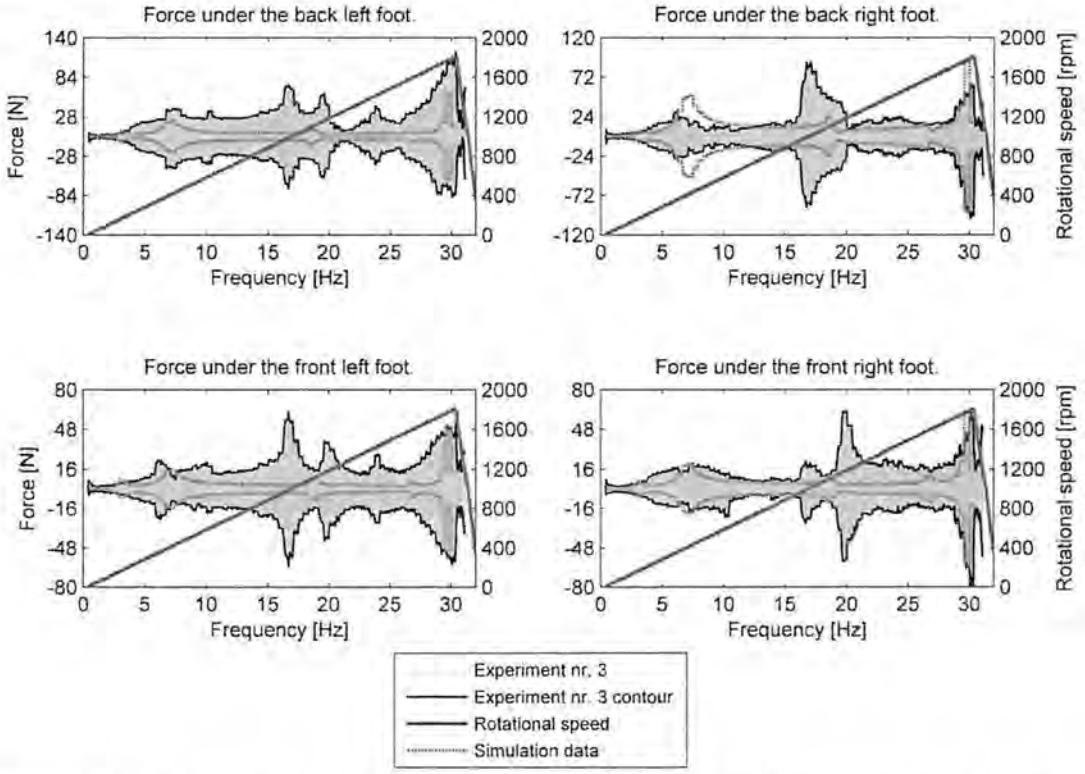

Figure 5-32: Forces under the feet for experiment number three versus simulated data.

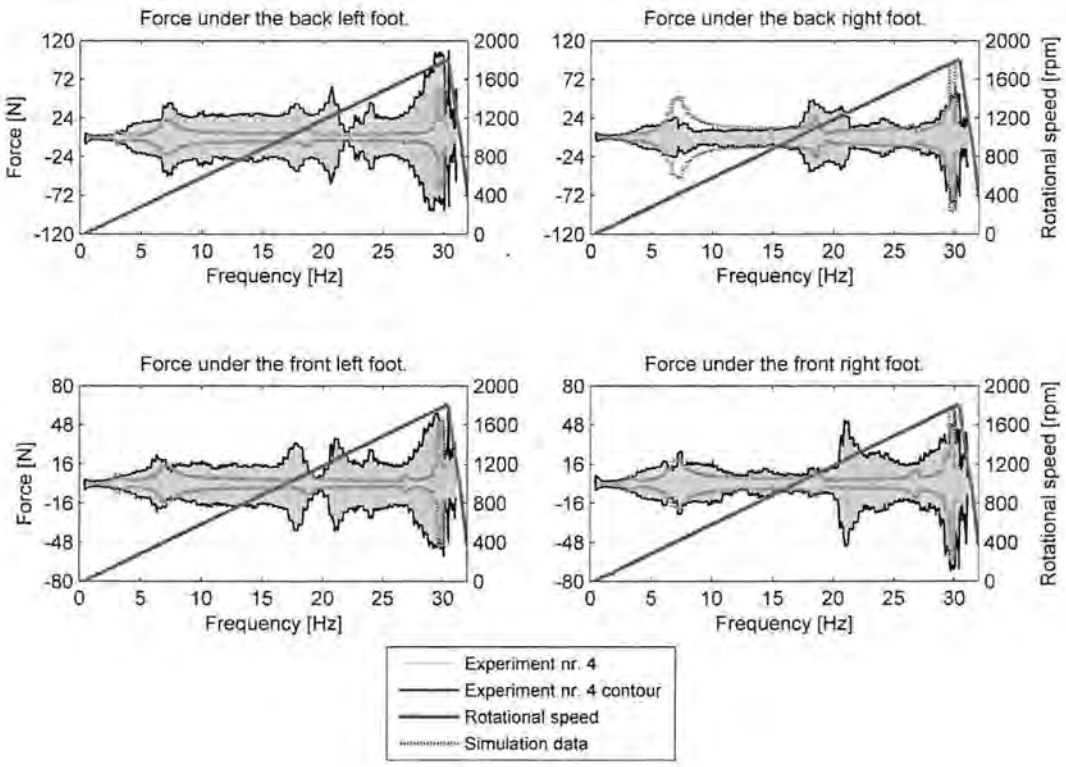

Figure 5-33: Forces under the feet for experiment number four versus simulated data.

The simulated curves shows resonance peaks at approximately the same rotational speeds as the measured data, but there are still some missing. The results are more or less the same for both experiments, but the simulated forces have a little better overall correlation with the fourth experiment performed with the rubber soles under the feet.

In both experiments it is noticed that the main amplitude is higher on the left feet then on the right feet. This can be explained by the fact that the drum rotates counter clockwise, seen from the front, the resulting forces in the belt moves the inside parts towards the left side and puts more weight on the left feet. This was also observed during the experiments, the drum tilts a few degrees in the counter clockwise direction at spin start and in the clockwise direction at spin stop which results in a higher force on the left feet during spin. The actual spinning is not modelled in the simulation and that is why the results do not capture this.

5.4 Investigation of acceleration and force signals

Since the simulations of the accelerations in the steel shell and the forces under the feet did not result in the coincident curves hoped for, an analysis of the measures signals was done using short-time Fourier transforms and visualized in Campbell diagrams.

The frequency of the fundamental dynamic load applied in the FE-model was in the range of 0-34 Hz. As can be seen in Figure 5-34, that load more or less only contributes to the amplitude of the acceleration above 15 Hz for measurement point N4. The rest of the accelerations arise from loads with higher frequencies than that of the fundamental load, these have not been added in the model.

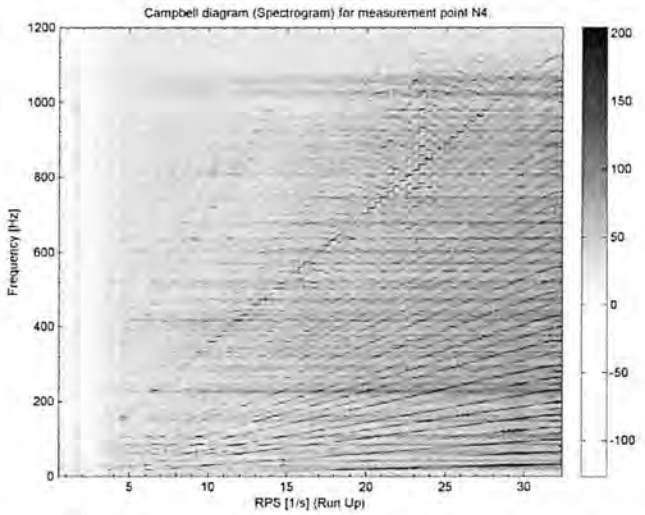

Figure 5-34: Campbell diagram for the acceleration signal on measurement point N4 in experiment six.

In Figure 5-35, the Campbell diagram for a measurement point on the drum container, shows that the accelerations are much more dependent of the fundamental dynamic loads, but that higher order harmonics also contributes. Campbell diagrams for each measurement point in set N for experiment six can be found in Appendix H.

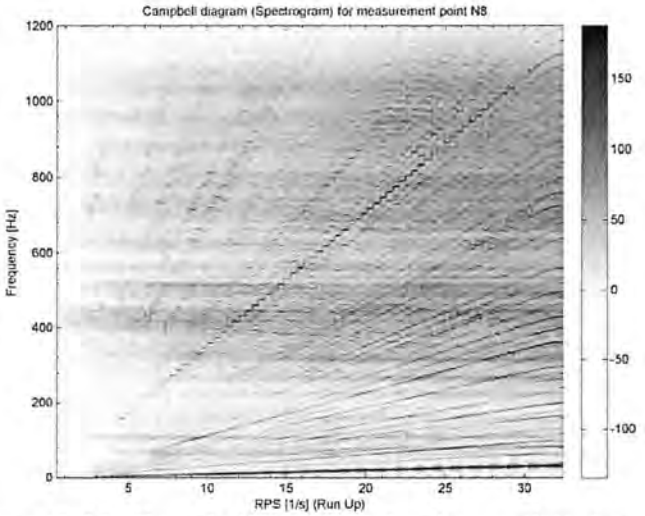

Figure 5-35: Campbell diagram for the acceleration signal on measurement point N8 in experiment six.

In both figures above it is clear that loads with frequencies much higher than that from the unbalanced drum, contributes to the accelerations. It can be seen that multiples of the fundamental frequency contributes strong to the acceleration up to as high as 35 times that of the fundamental frequency. These high frequency loads most likely arises from the engine itself. In the force signals, Figure 5-36, these higher multiple frequencies are not as dominant as in the accelerations in the shell.

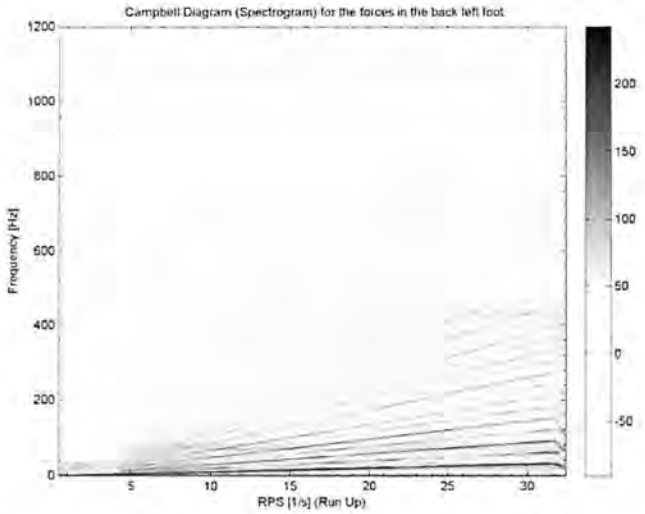

Figure 5-36: Campbell diagram for the force signal under the back left foot in experiment three.

As can be seen in Figure 5-36, higher order harmonic loads gives less contribution to the forces under the feet than to the accelerations in the steel shell. Still the contribution from higher frequency loads in the machine cannot be ignored.

6 Concluding remarks

To relate to the purpose of this master thesis the good correlation of the models with EMA will be a good basis for ASKO Appliances future work with creating a working-plan on how to model updates and new steel shell parts.

The goals of the master thesis are fulfilled to a quite large extent even if not all the correlations are very good. The good validation result of the steel shell models with EMA fulfills one part of the goals. The other part of the thesis work with the spin up of the machine did not show the results hoped for. However, the results are promising and probably only the lack of available time for model update made the correlation between analysis and experiment poorer than expected.

6.1 Separate parts

The models for the separate steel parts and the assembled steel shell correlate rather well with the measured data. The oil canning effect as observed in the side plates are not as strong when the parts are assembled in the entire steel shell as when it was analyzed individually or assembled with just a few parts.

Overall it is a problem trying to get the first mode to correlate well in almost all individual parts. The problem is worse if the parts have thin large flat surface areas. A probable explanation is that the stiffness in the deformed areas, due to manufacturing of the part, decreases which would affect parts with larger thin areas the most.

The side plates and the back plate are the parts that suffer from this problem the most. For the side plate it is the first mode that is hard to match by eigenfrequency, that mode has similar deformation patterns as the oil canning pattern on the plate. On the other hand, for the back plate it is the second mode that has the same deformation pattern to the oil canning patterns and therefore is very hard to match. Both the modes have strongly correlated mode shapes, but they do not occur at the correct frequencies.

All the calculated frequency response functions for the separate parts have a good overall shape. Although the contributions of some modes in almost all models are not correct. The best fitting curve is obtained in the lower front plate which is a part which was measured using the LDV. It was observed that parts measured using accelerometers showed a worse correlation to the measured response functions. This is probably an effect of the weight of the accelerometers not being added to the FE-model. This would most likely affect the results of the calculated frequency responses since the weight of the separate parts are not very high.

6.2 Assembled steel shell

The mode shapes of the assembled steel shell correlated well up to 60 Hz, after that the mode shapes became increasingly complicated. The problems with the side plate that was seen in previous thesis work were here avoided since the assembled steel shell using all parts was stiffer. This meant that the first natural mode of the side plate was never excited.

The problem with first mode which was not excited during the experiments of the steel shell is a bit worrying. Since there were enough accelerometers on the shell and at least one of the shakers position should have excited the mode. That it should be a fake mode from the FE-model or that it is a mode with a high damping is not considered likely since it was properly identified when correlating the separate part of the lid.

Problems that can occur when using as much fishing line as was needed when suspending the steel shell in the steel pipe frame. More vibrations from the surroundings can affect the measurements. This together with the steel pipe frame not being entirely steady could affect the measurements in a negative way.

Further problems which can cause bad MAC correlation is the system identification. For the assembled steel shell the identification was trickier than for each separate part. This since there was a lot modes at a short frequency range. Modes with a small response close to modes with larger response are hard to catch in the identification. The same problem occurs when trying to identify modes with low responses due to the placement of the shaker. To catch these small modes, high model orders are needed which results in a lot of false modes which has to be removed from the model.

6.3 Spin up tests

The spin up analysis suffers of poor results both for acceleration and force correlations. Much of the poor results can be explained by the accelerations depending more on higher frequency loads than those added to the model. These higher frequency loads has not been identified, but most likely it arises from the engine and unsymmetrical rotating parts. The Campbell diagrams show that the only areas where the fundamental frequency contributed to the accelerations in the steel shell were at three resonances at 19, 23 and 30Hz. Other than that, only load with higher frequencies contributed to the acceleration. This is a reason for why the simulated acceleration curves are almost zero in between the resonances.

The simulated accelerations on the drum container matched the measured data much better than those in the shell. This was because these accelerations were much more dependent of the fundamental dynamic load which could be seen in the Campbell diagram of those measurement points (N6, N7 and N8). The resonance peaks in the measured data indicates that higher frequency loads contributed to the acceleration in these points as well. The conclusion can be drawn that the load applied in the model are a good representation of the load that arises from the unbalanced drum. This since the acceleration, most dependent of this load, matched the simulated accelerations rather good.

The simulated force curves under the feet fits better than the acceleration curves to the measured data, but the amplitude of the resonance peak close to 20 Hz is too low compared to any of the measured resonance peaks occurring in the surrounding section. This low amplitude cannot only be explained by higher frequency loads which are not added to the model, but is instead believed to be a consequence of the modeled spring legs and bushings not transferring the correct loads. A deeper study on how to model the spring legs probably needs to be done to get better results, but that was not possible because of the limited time frame. In the end of this master thesis some work were done on improving the spring models and every update gave better results, so there is a potential to get better result with an better spring leg model.

The results also show that the accelerations in the shell are more or less unaffected of how the washing machine is placed when performing the experiments. What is important is that the rubber bushings are modeled accurately. However, the foundation of the washing machine is important when measuring the forces underneath the feet. This is something to have in mind in further work with getting a well correlating model of the washing machine.

6.4 Recommendations for future work

For future work, there are a few things that can be further examined, primarily an examination of the mode shapes in the resonances at spin up of the machine and the modeling of the spring legs.

It is important to get knowledge of how the steel shell deforms in the resonances, this in order to see if the modal properties, when the feet are fixed to the ground, is accurate or not. This is preferably done with the LDV from which a full-field picture of the deformation can be obtained rather easy. When all resonances up to 2000 rpm have been properly identified work can continue with either updating the model of the entire shell if the modes do not correlate well, or create a better model of the spring legs to get a better transfer of forces from the drum into the steel shell.

It is also important to find the primary causes of the higher frequency accelerations in the shell. A big improvement would be made in the simulated response of the shell by adding some of the high frequency loads. To find these loads would be a matter of analyzing all the rotating parts in the machine and find probable asymmetries or electromagnetically forces from the engine. Another probable effect can be from the driving belt oscillating at its eigenfrequency causing loads.

To further validate that the steel shell accelerations would match better if a valid model of the drum and spring legs was obtained; the forces and moments could be measured under each spring leg during a spin up of the engine. By applying these loads to the bottom plate in the contact point of the spring legs, should give an approximate value of the accelerations in the shell during a spin up. Although, this method should be used with caution since it is likely that the problem cannot be uncoupled like that. These forces could also be used to compare with the forces in the spring legs in the FE-model to see if similar forces are transferred through the inside parts down the spring legs.

Further investigations of the spring legs and the rubber bushings are needed to be done to see if it is possible to get a good linear model of the parts. Because even though the damping was removed from inside the spring legs, there are still plastic parts in the leg which causes friction damping. The current status of the model shows that the spring legs are not transmitting enough force to the bottom plate.

To reduce the solution times of the modal analysis there are three ways to go. Either gain access to a computation cluster to run the simulations on. This is a good solution since it means that the FE-models of the inside parts can be done more exact. The second possible solution is to use a reduction method for the modal analysis such as Guyan reduction. The last option is to decrease the number of degrees of freedom in the model.

7 References

Abrahamsson, T. (1999). *Linear system theory in vibrating engineering.* Göteborg: Chalmers.

Brüel & Kjaer. (2006, 09 06). Retrieved 05 15, 2009, from http://www.bksv.com/doc/Bp1874.pdf

Campbell Diagram. (2009, 05 09). Retrieved 06 15, 2009, from diracdelta.co.uk: http://www.diracdelta.co.uk/science/source/c/a/campbell%20diagram/source.html

Craig Jr., R., & Kurdila, A. (2006). *Fundamentals of Structural Dynamics* (2nd Edition ed.). New Jersey: John Wiley & Sons Inc.

Dytran Instruments Inc. (n.d.). *Product Details.* Retrieved 06 30, 2009, from http://www.dytran.com/go.cfm/en-us/content/product/611/ACCELEROMETERIEPE-3224A1/x?SID=

Ewins, D. (2000). *MODAL TESTING: Theory, Practice and Application 2 ed.* Baldock: Research Studies Press Ltd.

FEMAP 10.0.1 Online Help. (2008).

Gustafsson, M. (2007). *FE-modellering och experimentell validering av skalet till en tvättmaskin.* Göteborg: Applied Mechanics, Chalmers University of technology.

Henriksson, C.-J., & Melander, A. (2006). *FEM-modellering med experimentell validering av sidoplåt för tvättmaskin.* Göteborg: Applied Mechanics, Chalmers University of technology.

HP: Product Overview. (1998, 01 27). Retrieved 05 13, 2009, from HP: Product Overview: http://cp.literature.agilent.com/litweb/pdf/5966-3062E.pdf

Japp, M. (2003). *Formelsamling i mekanik.* Teknisk mekanik, Chalmers.

Kirby, J. R. (2000, 01 05). *Technical database search | NRCA, National Roofing Contractors Association.* Retrieved 06 04, 2009, from http://docserver.nrca.net:8080/technical/6771.pdf

Niels, O., & Petersson, H. (2000). Introduction to the finite element method. Lund: Prentice Hall.

Nygårds, T. (2009). *Modeling and Optimization of Washing Machine Vibration Dynamics During Spinning.* Chalmers University of Technology, Department of Applied Mechanics. Göteborg: Chalmers Reproservice.

PCB Piezotronics. (n.d.). *PCB Piezotronics, Inc.- Sensors that measure up!* Retrieved 06 02, 2009, from http://www.pcb.com/

Polytec. (2002, 11 05). *Dynamics and Vibration Research Group.* Retrieved 06 02, 2009, from http://www-mech.eng.cam.ac.uk/dynvib/lab_facilities/vibrometer_hardware_manual.pdf

Siemens PLM Software. (2008). FEMAP 10.0.1 Online Help.

STFT. (2009, 04 30). Retrieved 06 15, 2009, from Origin Lab: http://www.originlab.com/www/helponline/Origin8/en/Origin.htm#Signal_Processing/Short_Time_Fourier_Transform_Pro_only.htm

The Hanning window. (2009, 02 09). Retrieved 06 15, 2009, from DLI Engineering: http://www.dliengineering.com/vibman/thehanningwindow.htm

The Mathworks. (n.d.). *MATLAB - Documentation.* Retrieved 05 31, 2009, from http://www.mathworks.com/access/helpdesk/help/techdoc/index.html?/access/helpdesk/help/techdoc/

Appendix A – Experimental equipment

Accelerometers

PCB Piezoelectronics
Model: 352C22
Serial number: 24016
27328
27329
78795
97281
97282
Model: 333B32
Serial number: 14468
25156
25157
25158

Dytran Instruments Inc.

Model: 3224A1
Serial number: 204
205

Agilent VXI Mainframe

Hewlett Packard HP 75000 Seriec C
Model: E8408A
Serial number: US39000565

Amplifier

Cambridge Audio
Model: P500
Serial number: 211-P500-0799-0084

Charge-to-Deltatron Converter

Brüel & Kjaer
Type: 2647B
Serial number: 10023

Force transducer

Brüel & Kjaer
Type: 8203
Serial number: 10023

ICP/Voltage Digitizer

Hewlett Packard
Model: E1432
Serial number: US35373000
US35373001

Shaker

LDS Ling Dynamic systems LTD
Model: V201
Serial number: 69184-24

Polytec junction Box

Polytec GmbH
Model: PSV-Z-040
Serial number: 5 00 1405 0015

Polytec vibrometer controller

Polytec GmbH
Model: OFV-3001 SH6
Serial number: 5 00 1550

Polytec scanning head

Polytec GmbH
Model: OFV-056
Serial number: 6 00 1881

Appendix B – Simplifications made on parts

Typical simplifications done on the shell structure parts are small holes that are removed or small areas of complex geometry that is simplified. An example of simplified geometry can be seen in Figure B1 for the lid. For the inside parts larger holes are removed and less complex geometries are simplified. One example is the innermost drum that has a lot of small holes, which is removed to be able to use a lager mesh size. Even the CAD-model from ASKO Appliances AB did not have all the holes.

B.1 - Shell structure parts

A more detailed description of the modeling and simplification of each part in the shell structure are presented here.

Bottom plate

Not much is simplified on the bottom plate, only imprinted text and symbols has been removed.

Side plate

The modest simplifications done on the side plate is small holes, bulges and text that are removed.

Lid

The simplifications done on the lid is text that is removed and the geometry in the two back corners that are simplified, which can be seen for the right back corner, in Figure B1.

Figure B1: Original geometry to the left and simplified geometry to the right.

Transport beam, Cross beam and Electric bridge

The modest simplifications made on these three parts are of the same character. Small holes and text are removed.

Front beam

There are modest simplifications done on this part. Most of these are areas with complex geometry. Text and small holes are also removed.

Lower front plate

In all four corners simplifications a lot like those on the corners of the lid have been made, see Figure B1. Beyond those corners, areas of complex geometry and text have been removed.

Upper front plate

Almost no simplifications have been made on this part. Only some text has been removed.

Back plate

There are perforations preparing for a rather big hole at the lower part of the back plate. The part covering the hole was removed both in reality and on the model. Nothing else has been simplified.

Bolts

There are no actual bolt parts modeled, but elements have been created between mounting holes of parts that should be attached to each other in the shell structure. These elements acts as connections and are grouped in sets with separate properties. The connection properties can be changed between all parts separately.

B.2 - Inside parts

A more detailed description of the modeling and simplification of each inside part are presented here.

Container and Container back piece

No simplifications were made on the geometry before meshing. But since a rather large element size was used, small details in the geometry will vanish and there for not be modeled.

Drum

In reality the drum have a lot of small holes with craters. To make a mesh that considers these holes require a very dense mesh, probably a mesh size about 1 mm. Instead a whole new part was created with smooth surfaces, a simple drum with the same diameter, depth and thickness.

Drum back piece

Only some minor mounting holes are removed from the outer part of the back piece.

Convey and axle

Since the convey frame and the axle shaft in reality are mounted tight together and both parts needed tricky simplifications a new part containing them both was made. In the axle shaft tracks were removed. For the convey frame the geometry were over all simplified and mounting holes were removed.

Back frame

The part is a piece of the back frame of the container and consists of the arms and outer ring of the frame. The part is modeled with plate elements with a rather large thickness of 5 mm. The geometry has not been simplified before meshing; it is only the large mesh size that reduces the details of the part.

Frame bracket and bearing

This part consists of the centre of the back frame (the frame bracket) that is a piece of the back frame. The centre of the back frame is also the house of two bearings, which holds the axle shaft in place. The bearings are simplified as two hole-cylinders with the same thickness and diameter as the bearings. The geometry of the frame bracket has not been simplified before meshing.

Axle plates

Three different axle plates that were mounted closely together have been modelled as one part. Since they are small and thin and to minimize the degrees of freedom and connections.

Belt pulley

The centre area there the belt pulley is mounted on to the axle shaft is simplified. This area also consists of more than one part which is merged together. The outer parts of the belt pulley have no simplifications.

Upper spring bracket and Lower spring bracket

The upper and lower spring bracket is two different parts modeled separately, but they are simplified in the same way. Small holes, bulges and text are removed.

Front gable and Front cover plate

The front gable and front cover plate are two separate parts but they have similar geometry and simplifications. On both parts small holes and bulges are removed.

Counterweight

There have been no simplifications to a rather basic geometry and because of the relative big mounting holes; 10 mm is about the largest element size that can be used. This leads to a high number of elements.

Bushing cup

No simplification has been made on this part; it is rather small and the geometry is simple.

Rubber bushing

Only the text on the part has been removed from the part model.

Engine

Since the engine has a lot of small parts of different materials and is quite complex it has been modeled with one mass element and the mounting points. The properties of the mass element have been gathered through some studies of the real engine. The weight has been measured to 4.80 kg. The mass Centrum was decided through suspending the engine in different points and comparing where the vertical lines from the suspending point intersected, see Figure B2. Values for inertia where calculated in the CAD-model using the simplification that all ingoing parts have the same density. The mass element is connected to the mounting points using rigid elements.

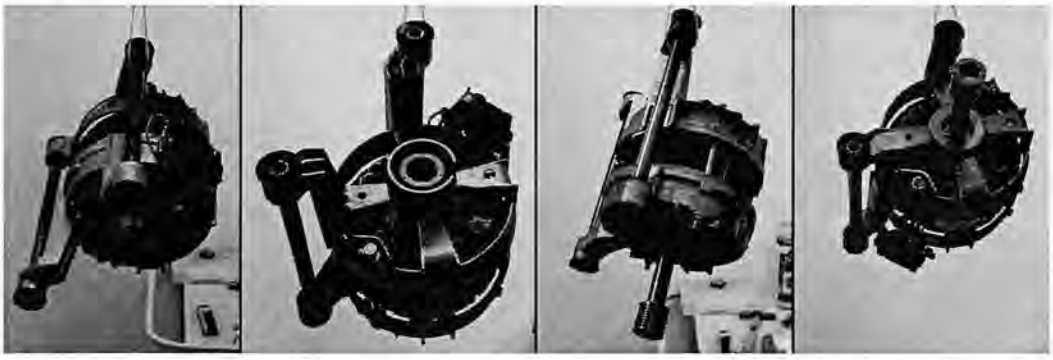

Figure B2: The engine suspended in different points.

B.3 - Feet and spring parts

A more detailed description of the modeling and simplification of feet and springs are presented here.

Spring leg

The spring legs have been modeled with rod elements since the spring elements in Femap did not transfer the forces in a correct way. The rod has properties corresponding to a rod with spring properties.

Leg end

This part is a piece of the real spring leg, the piece of the part that goes in to the rubber bushing. It has been created to have something solid to attach the spring leg model to. The model has been created from scratch using the real geometry as reference.

Balance spring

The part has been modeled with a spring element. There is no geometry left; only the length and properties of the spring are kept.

Foot

This part consists of two different materials; rubber and steel. On the end of the steel part that is screwed in to the bottom plate the thread has been removed and the end covered by the rubber part is approximated as a half circle from descriptions by Bengtsson & Eriksson, 2009. On the bottom surface of the rubber piece the grooves has been removed.

Appendix C – Previously modeled parts

In the table C1 the eigenfrequencies for the previous modeled parts are compared between previous EMA results, the FE-models and the previous FE-models, previous results come from Gustafsson (2007).

Table C1: A comparison between the EMA made in previous years thesis compared to the regenerated models

Bottom plate

Mode nr.	**1**	**2**	**3**	**4**	**5**	**6**	**7**
EMA [Hz]	40,1	117,7	145	189	233,3	256,9	278,2
FEM [Hz]	**43,22**	**115,5**	**147,9**	**188**	**235**	**251,9**	**275,5**
Diff [%]	**7,8**	**-1,9**	**2**	**-0,5**	**0,7**	**-1,9**	**-1**

E = 195 GPa **ρ = 7850 kg/m^3** **t = 1,5 mm** **ν = 0.30**

Pre. [Hz]	43,2	114,4	148,9	189,2	233,3	250,4	275,7
Diff [%]	7,7	-2,8	2,7	0,1	0	-2,5	-0,9

E = 195 GPa ρ = 7850 kg/m^3 t = 1,5 mm

Side plate

Mode nr.	**1**	**2**	**3**	**4**	**5**	**6**	**7**	**8**	**9**	**10**	**11**
EMA [Hz]	15,4	28,4	40,8	49,6	66,8	70,1	76	87,4	94	104,6	110,5
FEM [Hz]	**7,322**	**26,39**	**35,6**	**49,43**	**66,19**	**72,21**	**78,64**	**86,3**	**87,42**	**113,4**	**116,9**
Diff [%]	**-52,5**	**-7,1**	**-12,7**	**-0,3**	**-0,9**	**3**	**3,5**	**-1,3**	**-7**	**8,4**	**5,8**

E = 211 GPa **ρ = 7700 kg/m^3** **t = 0,9 mm** **ν = 0.321**

Pre. [Hz]	7,2	28,1	35,6	48,9	69,6	72,6	76,8	87,8	88,5	112,2	116,5
Diff [%]	-53,2	-1,1	-12,7	-1,4	4,2	3,6	1,1	0,5	-5,9	7,3	5,4

E = 225 GPa ρ = 7500 kg/m^3 t = 0,82 mm

Transport beam

Mode nr.	**1**	**2**	**3**	**4**	**5**	**6**	**7**
EMA [Hz]	67,1	122,1	207,8	323	409,6	556,6	654,4
FEM [Hz]	**65,18**	**121,6**	**208,5**	**326**	**409,8**	**561,8**	**666,3**
Diff [%]	**-2,9**	**-0,4**	**0,3**	**0,9**	**0**	**0,9**	**1,8**

E = 180 GPa **ρ = 7950 kg/m^3** **t = 1,5 mm** **ν = 0.30**

Pre. [Hz]	64,8	121,3	208,5	325,9	411,1	567,1	667,1
Diff [%]	-3,4	-0,7	0,3	0,9	0,4	1,9	1,9

E = 180 GPa ρ = 7900 kg/m^3 t = 1,5 mm

Cross beam

Mode nr.	**1**	**2**	**3**	**4**	**5**	**6**	**7**	**8**
EMA [Hz]	61,6	156,7	247,5	330,3	364,2	409,2	445,2	567,1
FEM [Hz]	**68,09**	**152**	**254,6**	**329,8**	**362,4**	**398,3**	**451,2**	**551,7**
Diff [%]	**10,5**	**-3**	**2,9**	**-0,2**	**-0,5**	**-2,7**	**1,3**	**-2,7**

E = 210 GPa **ρ = 7880 kg/m^3** **t = 1,0 mm** **ν = 0.32**

Pre. [Hz]	67,2	148,9	241	327,4	383,9	407,5	426,8	531,8
Diff [%]	9,1	-5	-2,6	-0,9	5,4	-0,4	-4,1	-6,2

E = 195 GPa ρ = 7950 kg/m^3 t = 0,97 mm

Front beam

Mode nr.	**1**	**2**	**3**	**4**	**5**	**6**	**7**
EMA	47,8	103,8	157,9	226,4	233,5	259,6	315,9
FEM	**47,87**	**103,8**	**154,4**	**217,7**	**225,9**	**262,8**	**316,5**
Diff [%]	**0,1**	**0**	**-2,2**	**-3,8**	**-3,3**	**1,2**	**0,2**

E = 180 GPa **ρ = 7900 kg/m^3** **t = 0,95 mm** **ν = 0.30**

Pre. [Hz]	48,2	104,6	160,4	225,7	227,9	255,6	309,9
Diff [%]	0,8	0,8	1,6	-0,3	-2,4	-1,5	-1,9

E = 180 GPa ρ = 7950 kg/m^3 t = 1,0 mm

FEM: Eigenfrequencies from FEM simulations.
EMA: Eigenfrequencies from previous master thesis EMA results, Gustafsson (2007).
Pre. : Eigenfrequencies from previous master thesis FEM solution, Gustafsson (2007).

Appendix D – Modal damping tables

Modal dampings for the first modes are presented for the separate parts.

Lid

Table D1: Calculated modal damping factors for the lid.

Mode	1	2	3	4	5	6
Modal Damping	0.0213	0.0018	0.0028	0.0003	0.0039	0.0002
Mode	7	8	9	10	11	12
Modal Damping	0.0026	0.0024	0.0012	0.0017	0.0011	0.0036

Upper front plate

Table D2: Calculated modal damping factors for the upper front plate.

Mode	1	2	3	4	5	6	7	8	9
Modal Damping	0.00039	0.00092	0.00012	0.00035	0.00037	0.00036	0.00024	0.00043	0.00033

Lower front plate

Table D3: Calculated modal damping factors for lower front plate

Mode	1	2	3	4	5
Modal Damping	0.0009	0.0013	0.0012	0.0010	0.0009
Mode	6	7	8	9	10
Modal Damping	0.0009	0.0007	0.0009	0.0009	0.0009

Electric bridge

Table D4: Calculated modal damping factors for the electric bridge.

Mode	1	2	3	4	5	6	7	8
Modal Damping	0.0059	0.0070	0.0053	0.0029	0.0046	0.0084	0.0017	0.0037

Back plate

Table D5: Calculated modal damping factors for back plate.

Mode	1	2	3	4	5
Modal Damping	0.0034	0.0033	0.0014	0.0008	0.0044
Mode	6	7	8	9	10
Modal Damping	0.0008	0.0010	0.0033	0.0037	0.0003

Appendix E – Frequency response function

Here frequency response functions are presented for all separate parts and the steel shell.

E.1 – Lid

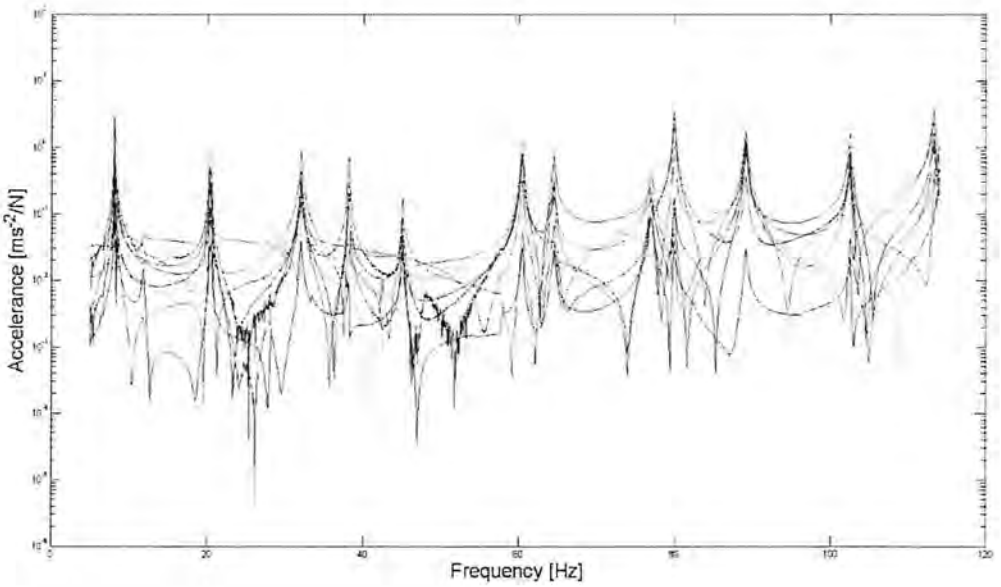

Figure E1: Frequency response function for the lid.

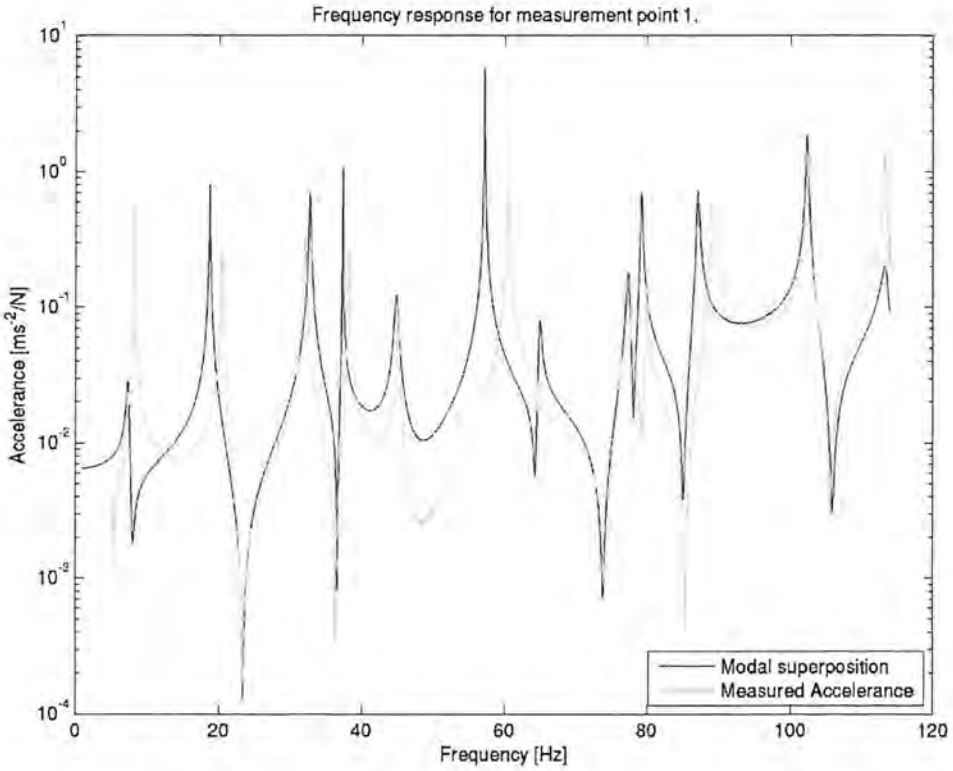

Figure E2: Frequency response for measurement point number one for the lid.

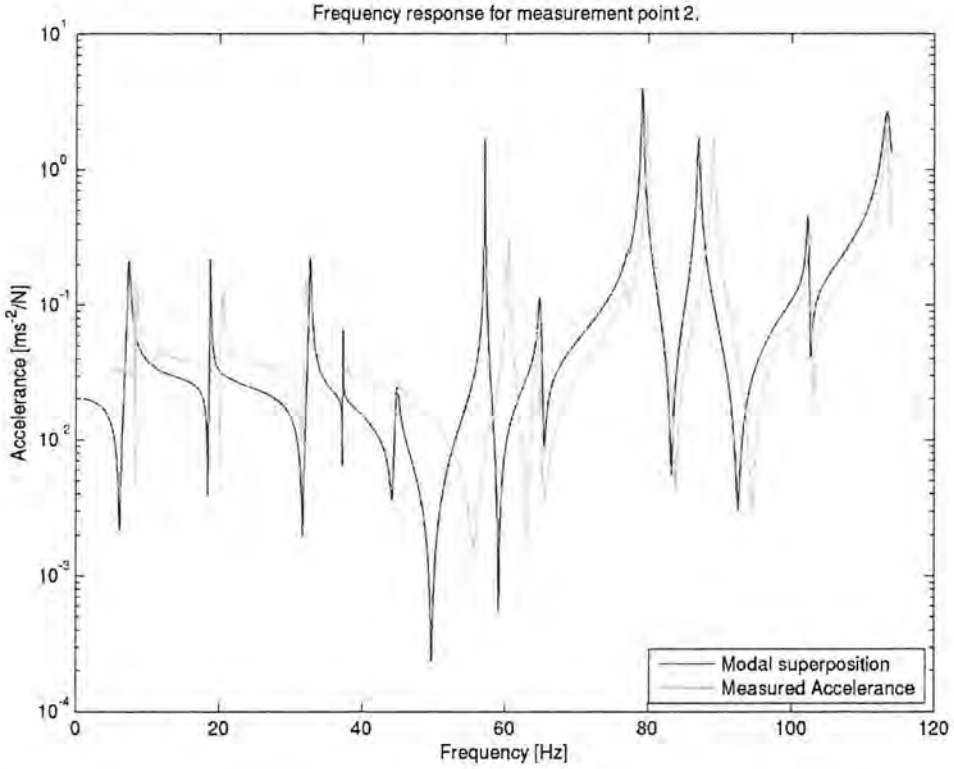

Figure E3: Frequency response for measurement point number two for the lid.

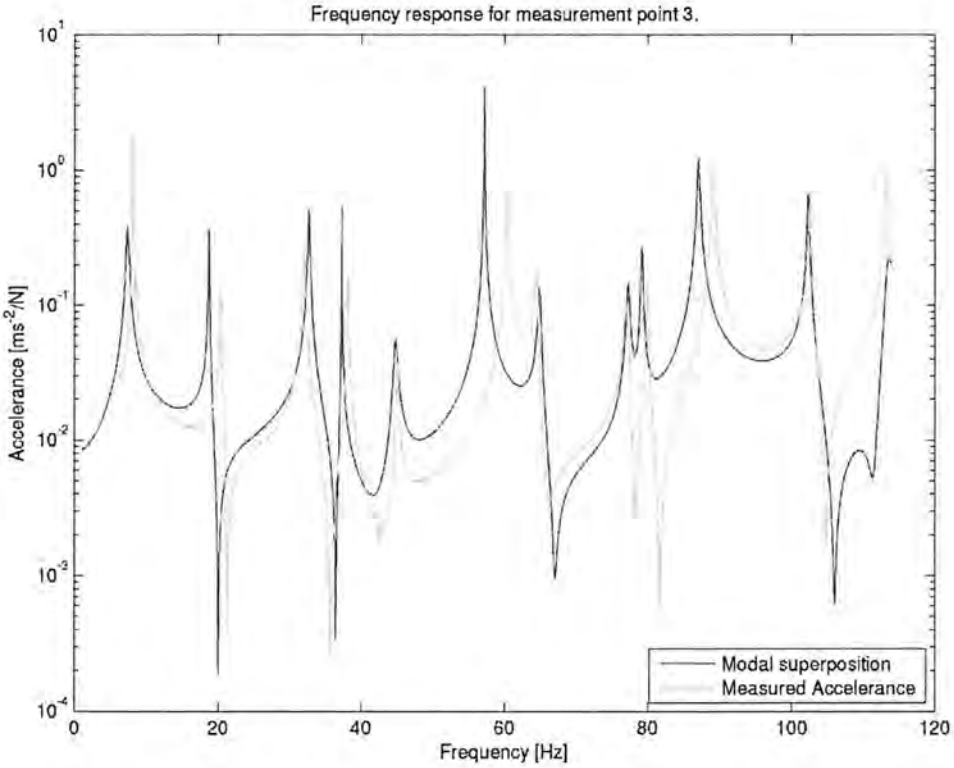

Figure E4: Frequency response for measurement point number three for the lid.

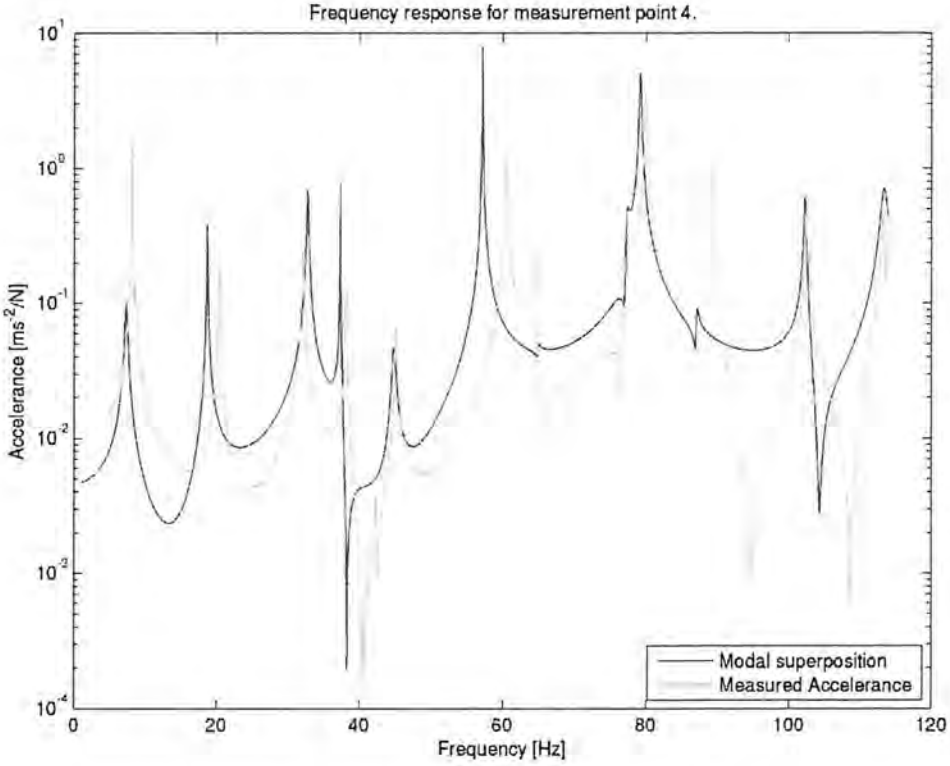

Figure E5: Frequency response for measurement point number four for the lid.

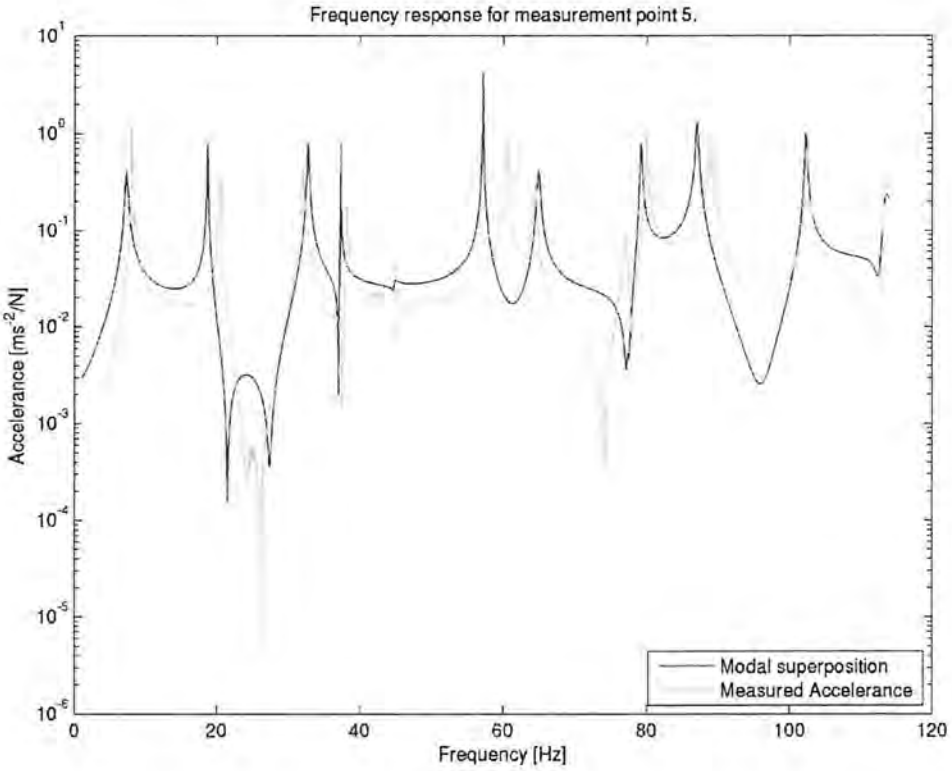

Figure E6: Frequency response for measurement point number five for the lid.

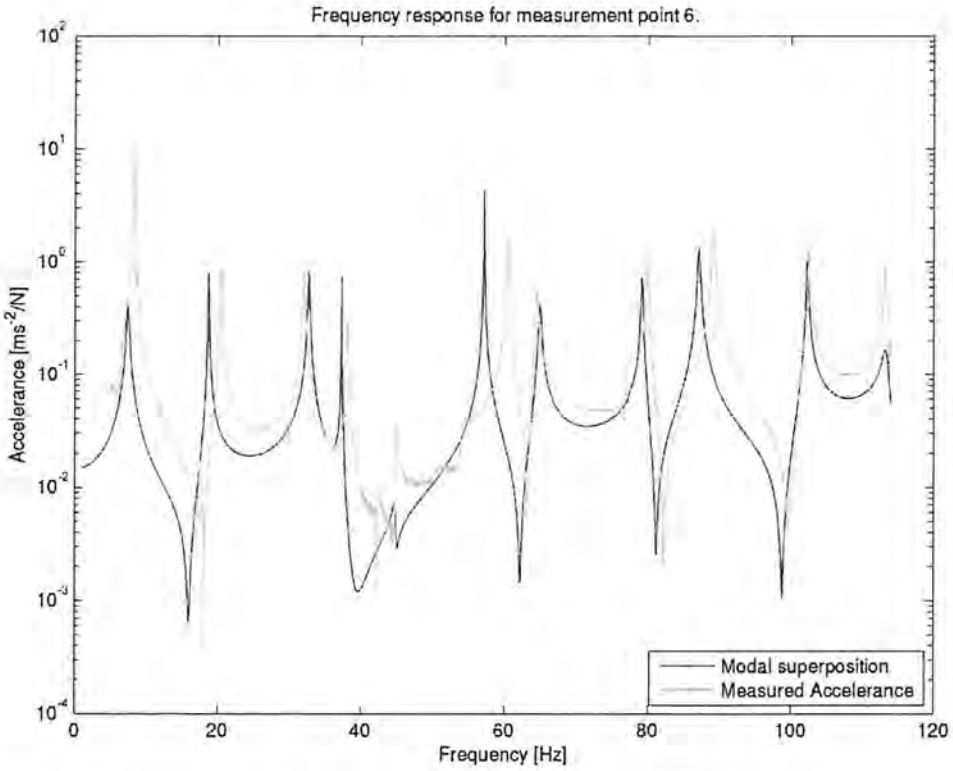

Figure E7: Frequency response for measurement point number six for the lid.

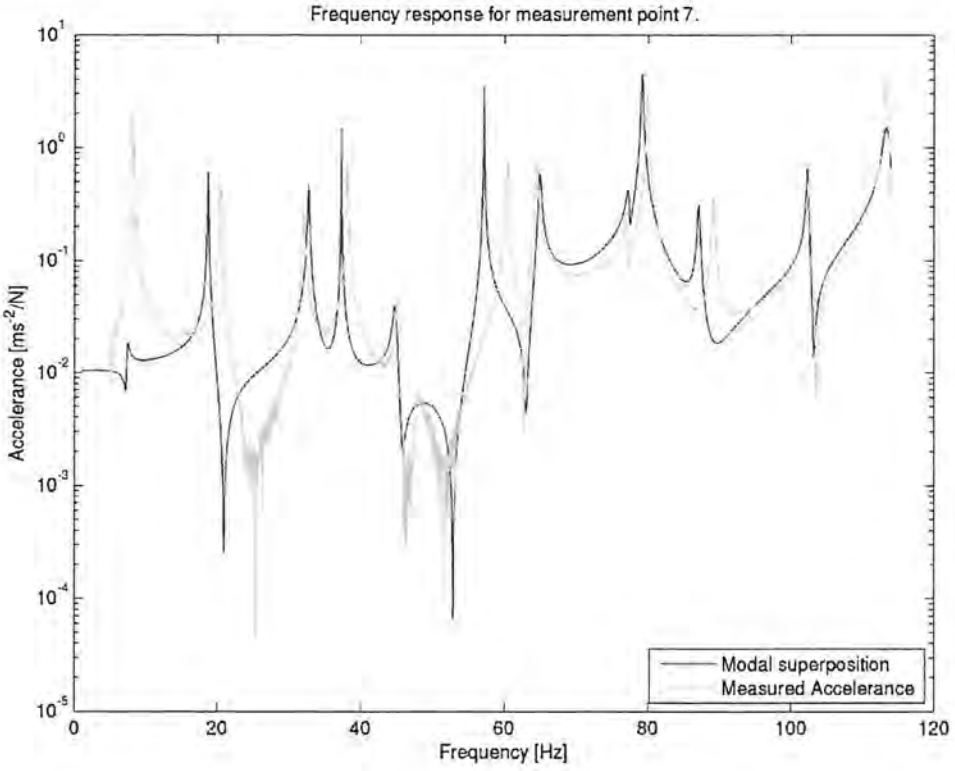

Figure E8: Frequency response for measurement point number seven for the lid.

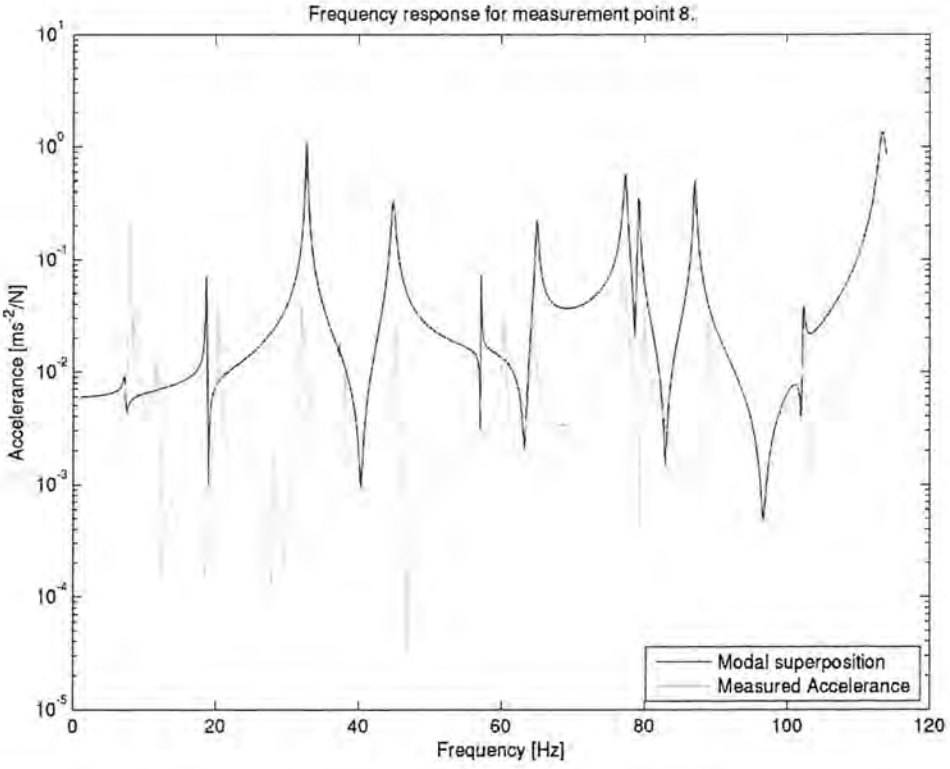

Figure E9: Frequency response for measurement point number eight for the lid.

E.2 – Upper front panel

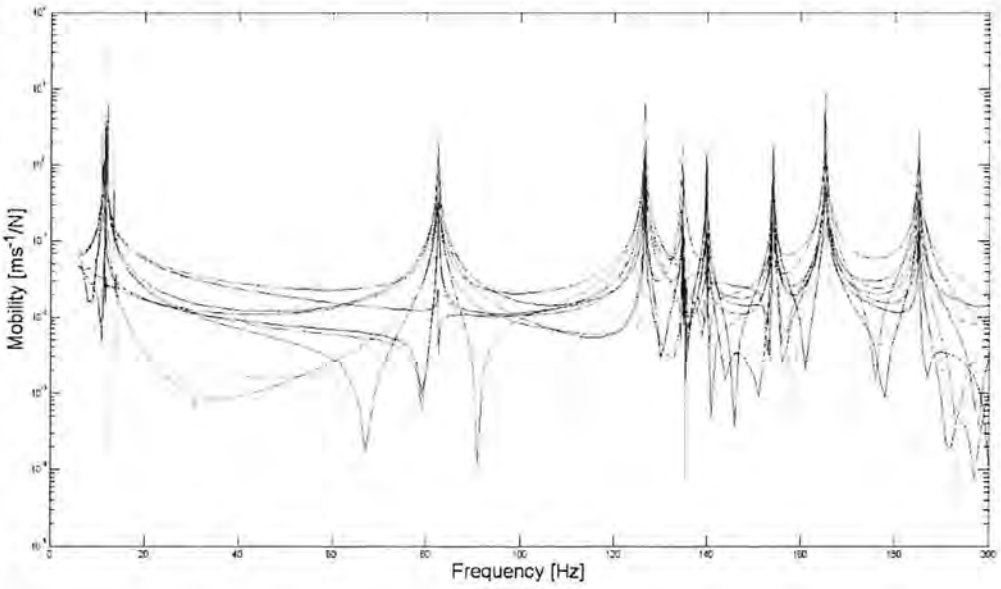

Figure E10: Frequency response function for the upper front plate.

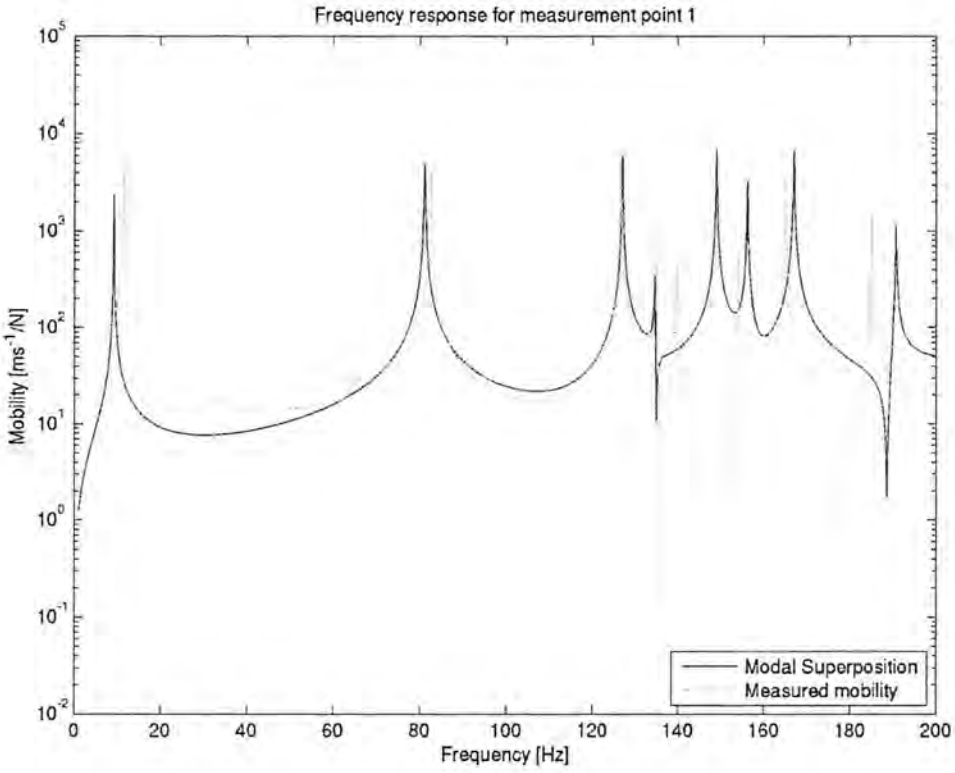

Figure E11: Frequency response for measurement point number one for the upper front plate.

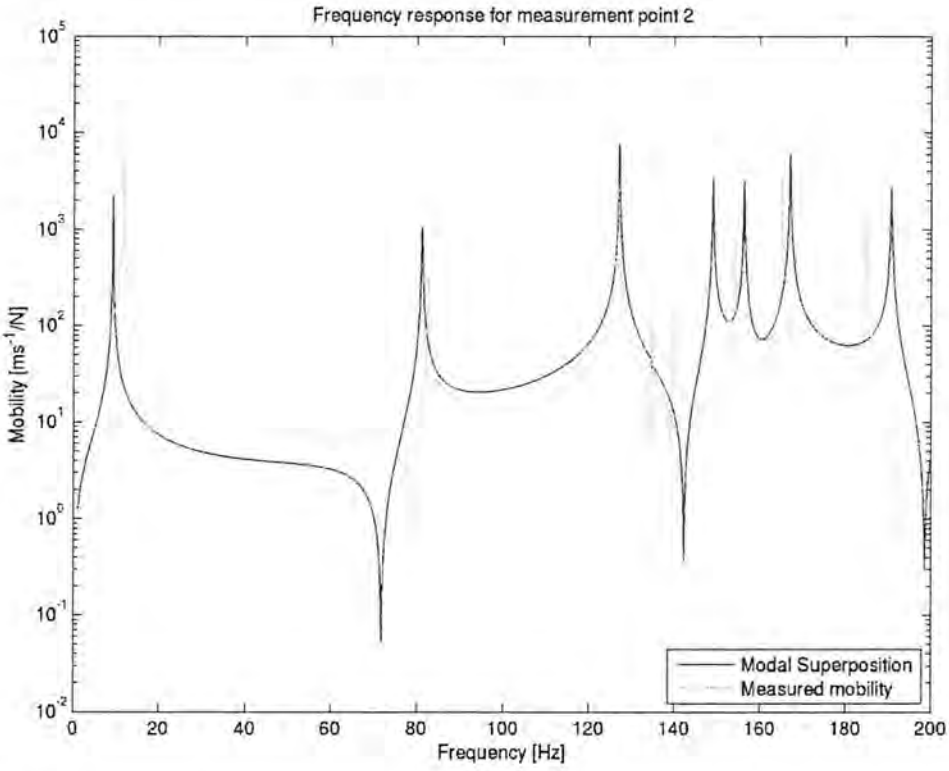

Figure E12: Frequency response for measurement point number two for the upper front plate.

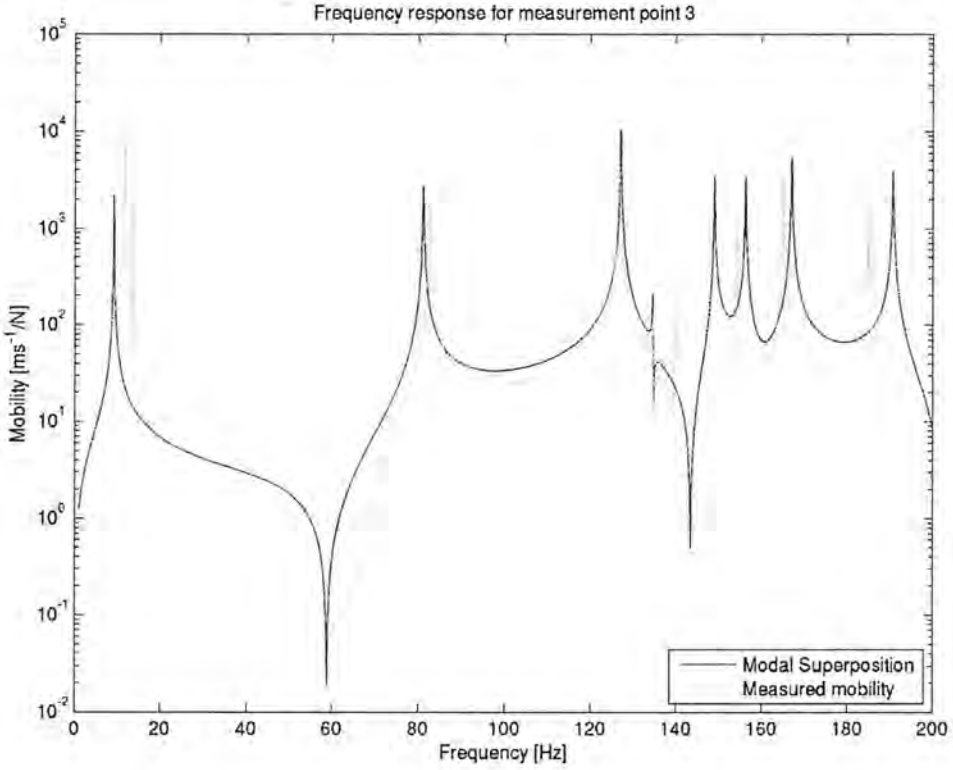

Figure E13: Frequency response for measurement point number three for the upper front plate.

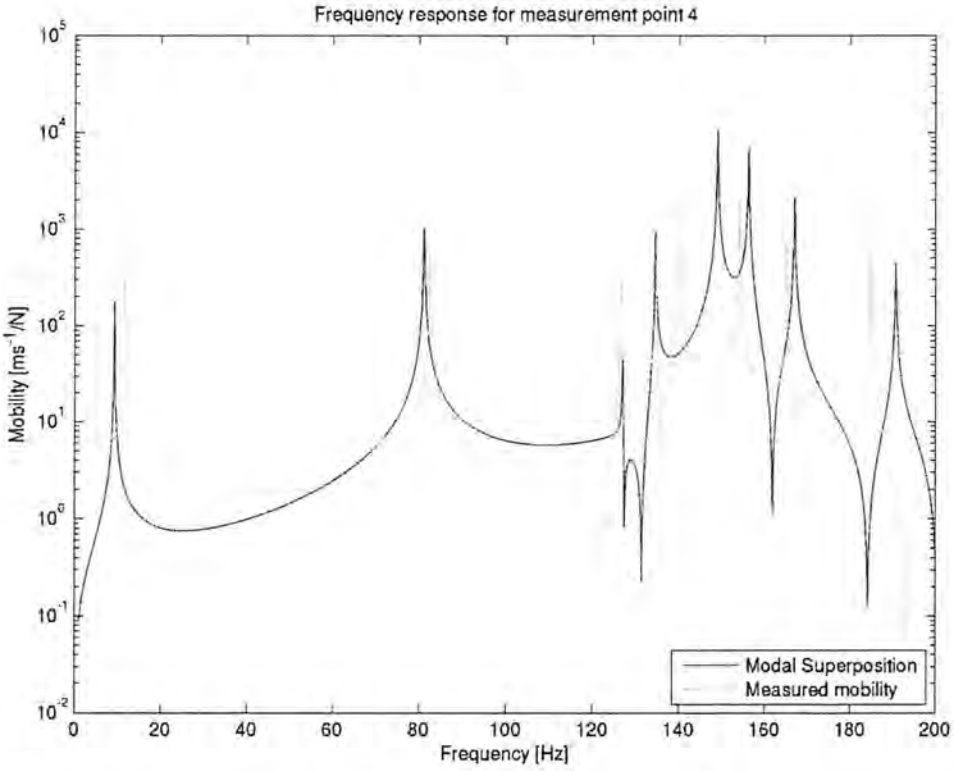

Figure E14: Frequency response for measurement point number four for the upper front plate.

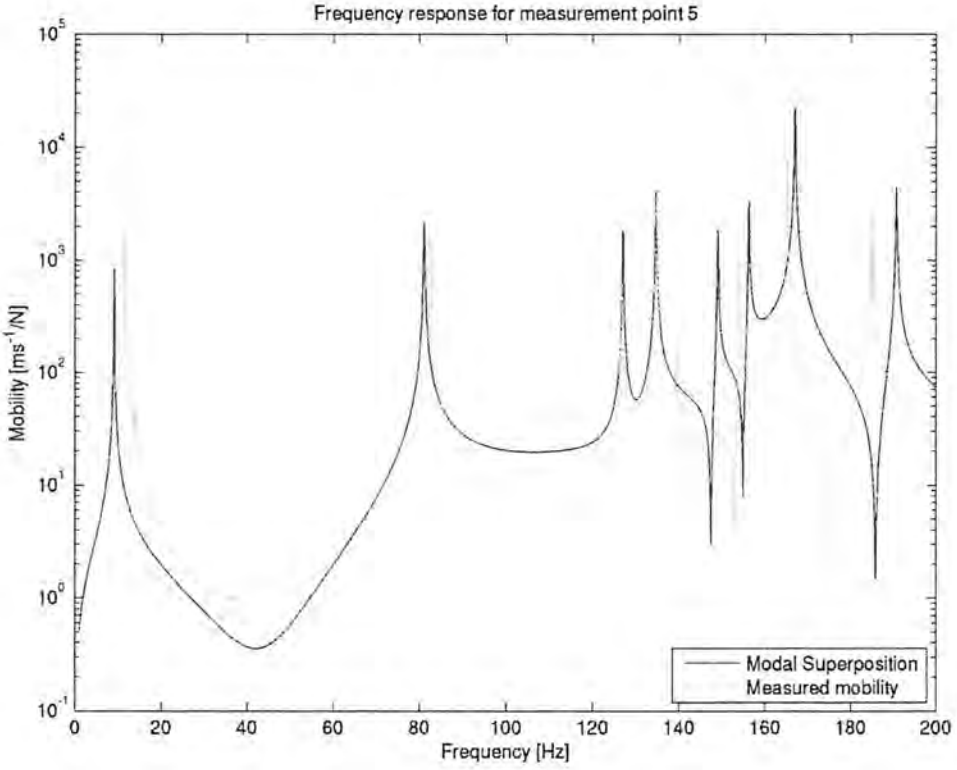

Figure E15: Frequency response for measurement point number five for the upper front plate.

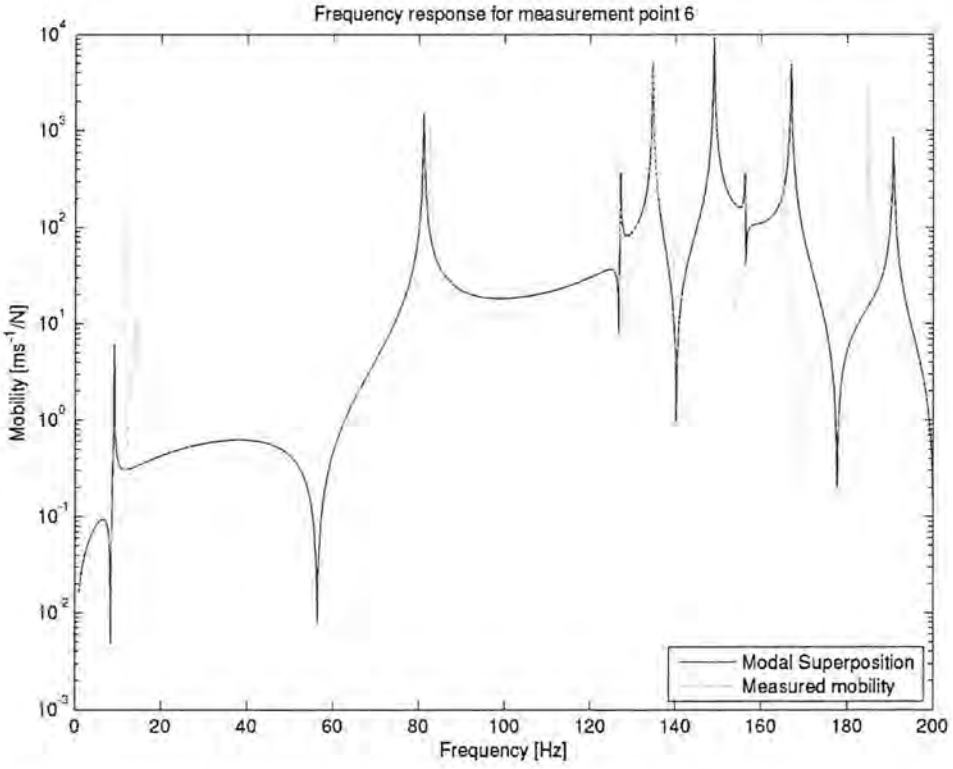

Figure E16: Frequency response for measurement point number six for the upper front plate.

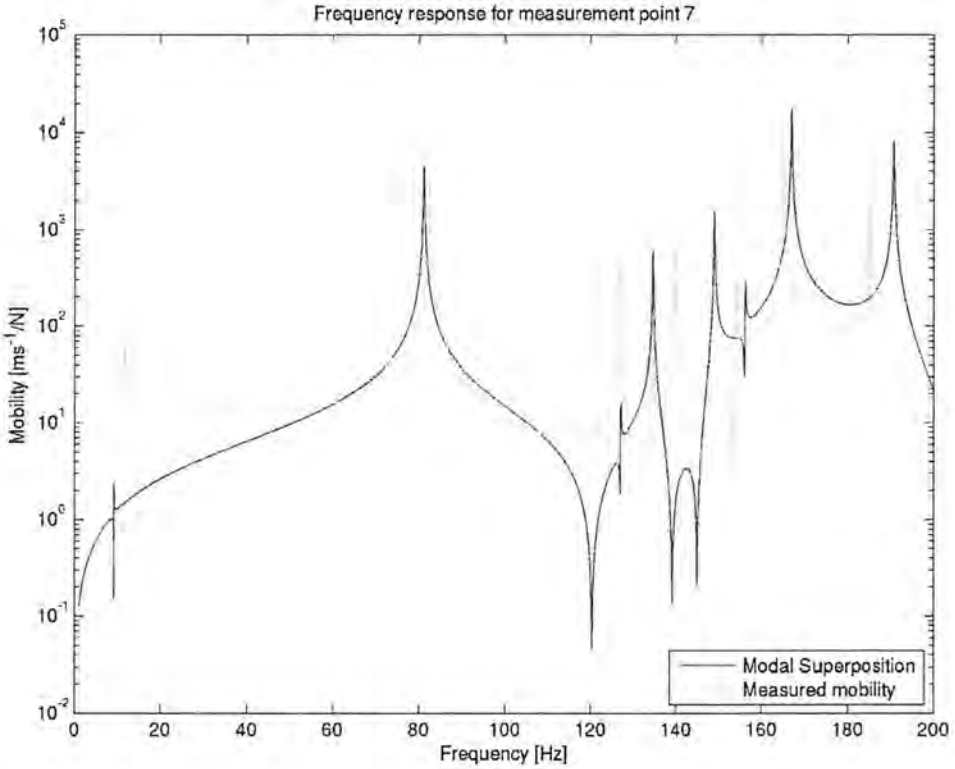

Figure E17: Frequency response for measurement point number seven for the upper front plate.

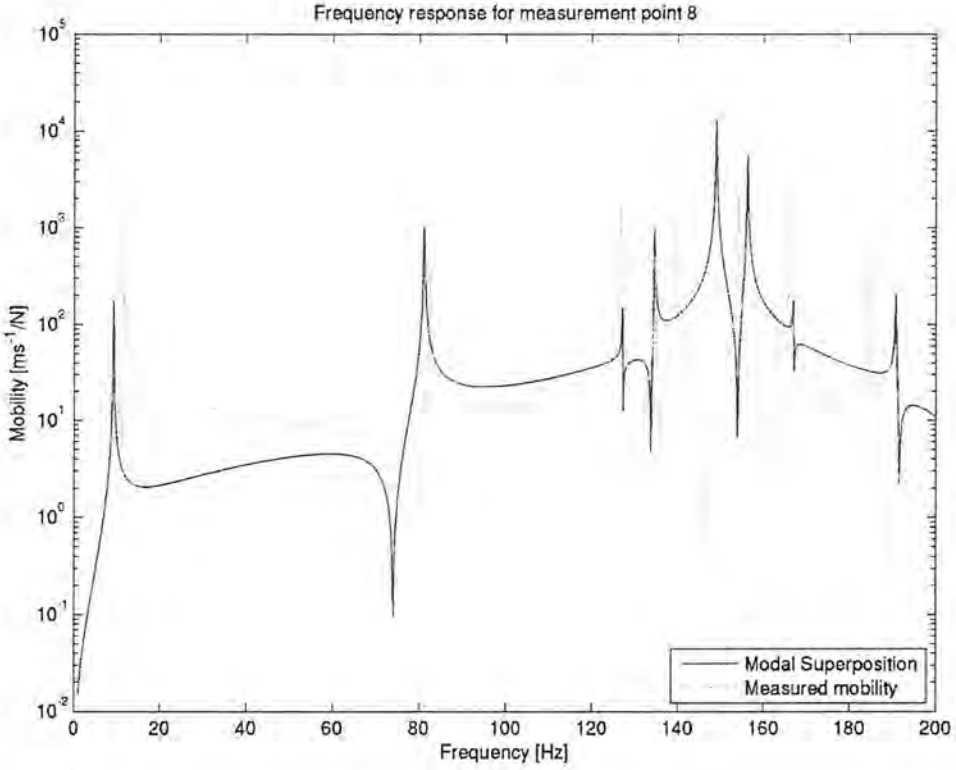

Figure E18: Frequency response for measurement point number eight for the upper front plate.

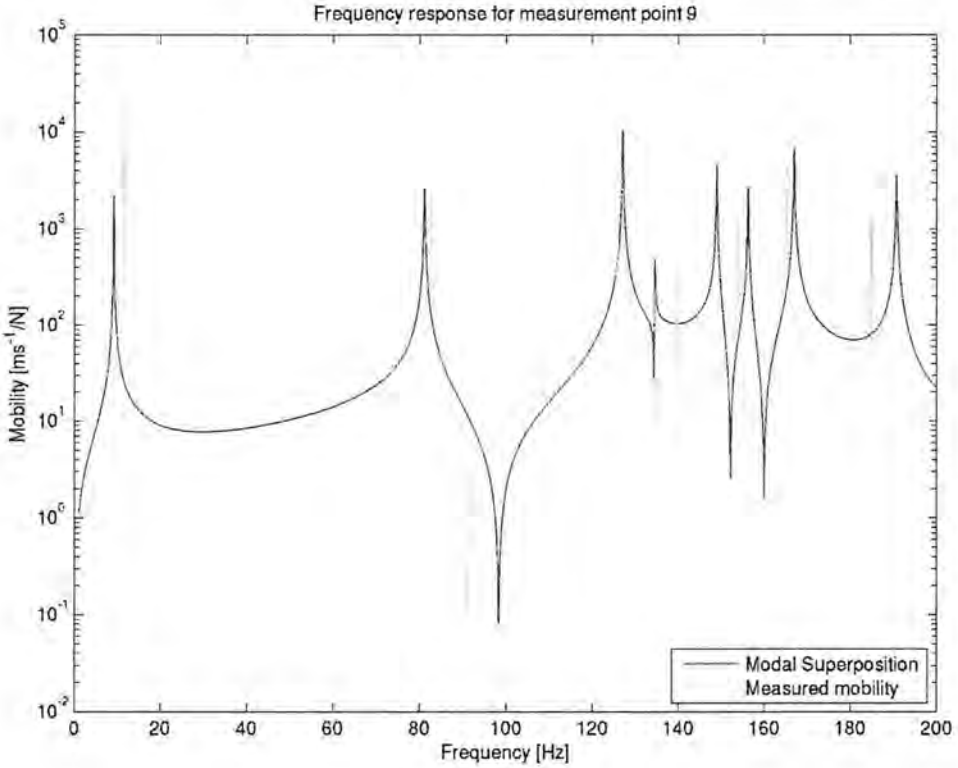

Figure E19: Frequency response for measurement point number nine for the upper front plate.

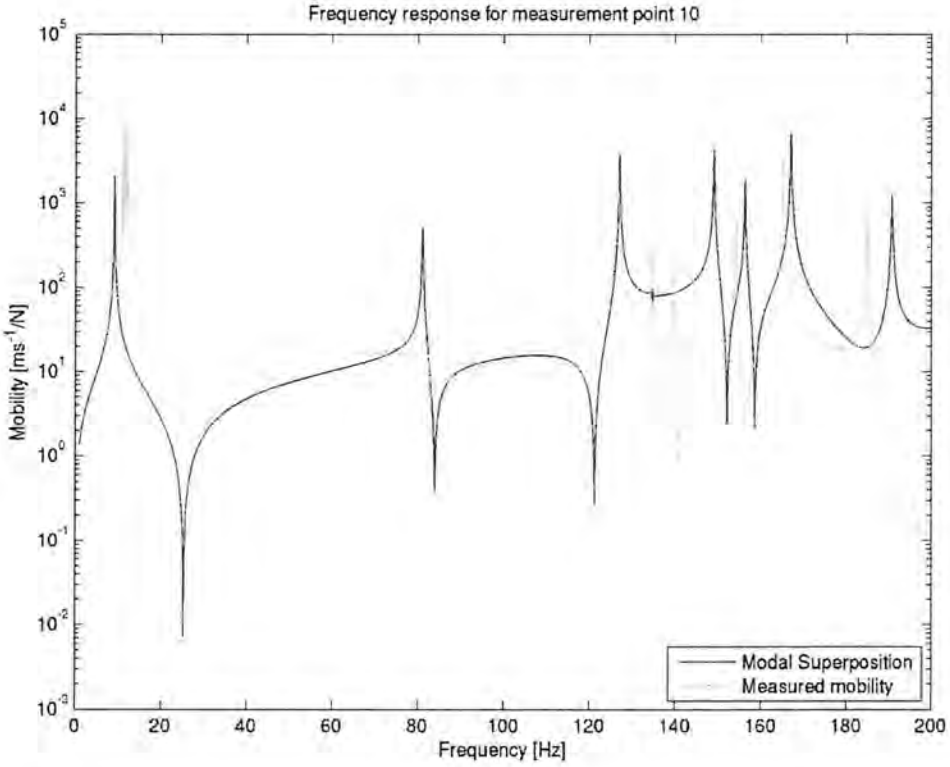

Figure E20: Frequency response for measurement point number ten for the upper front plate.

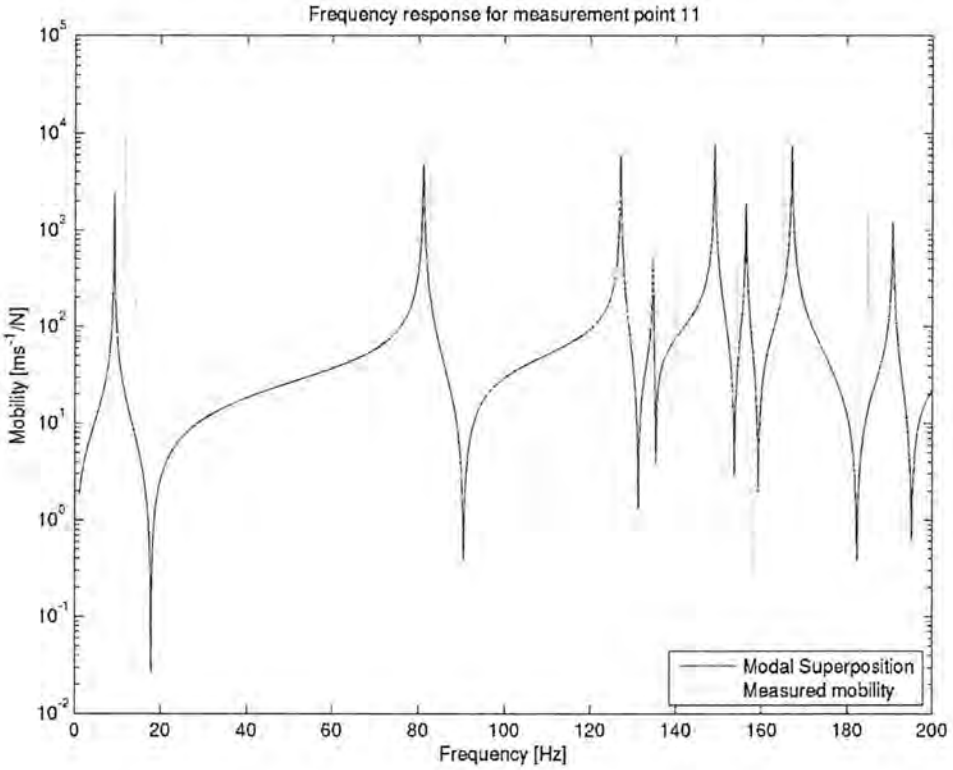

Figure E21: Frequency response for measurement point number eleven for the upper front plate.

E.3 – Lower front plate

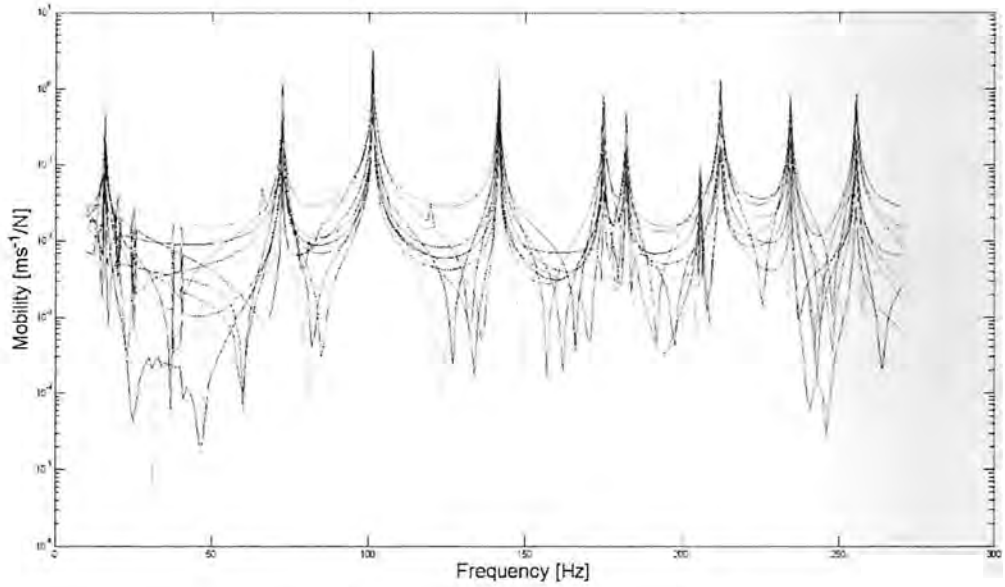

Figure E22: Frequency response function for the lower front plate.

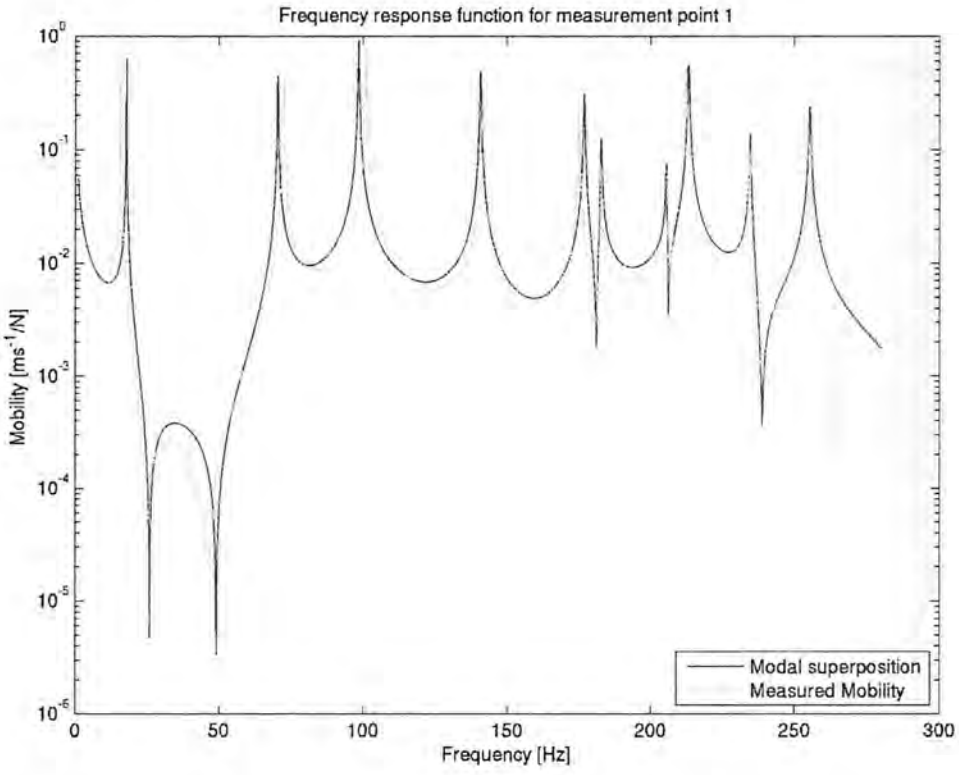

Figure E23: Frequency response for measurement point number one for the lower front plate.

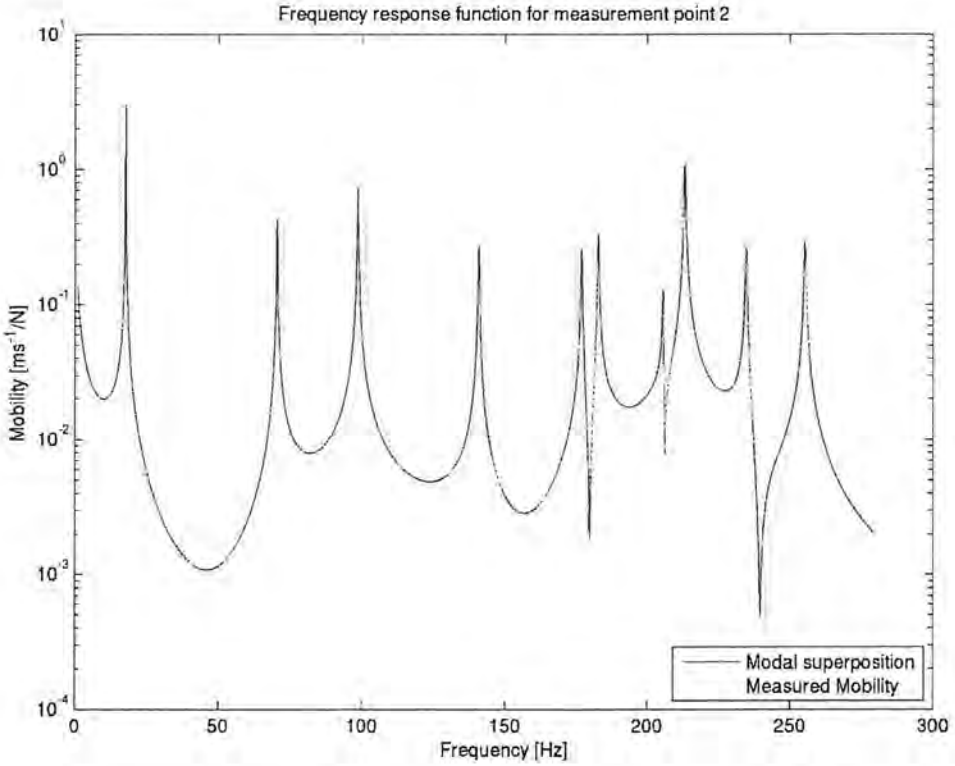

Figure E24: Frequency response for measurement point number two for the lower front plate.

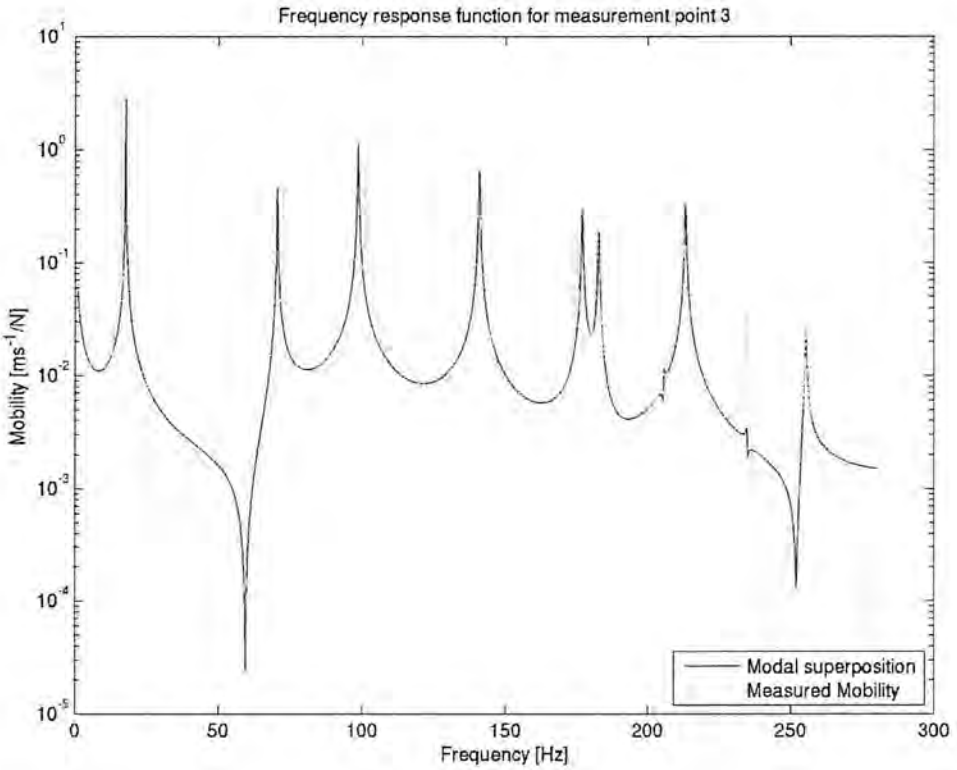

Figure E25: Frequency response for measurement point number three for the lower front plate.

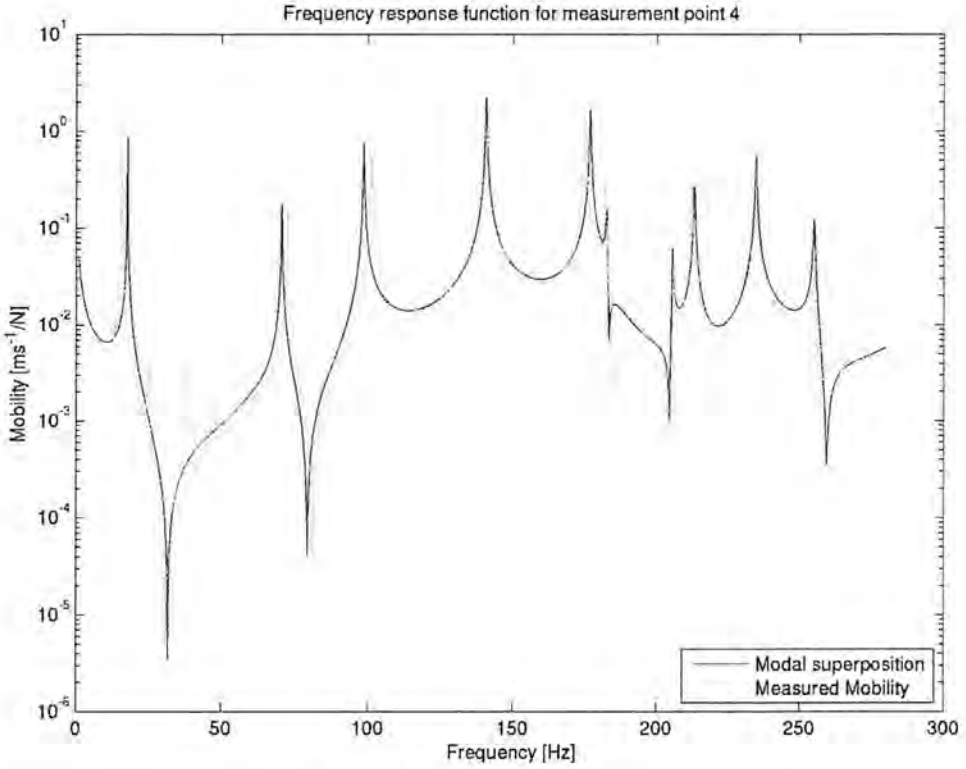

Figure E26: Frequency response for measurement point number four for the lower front plate.

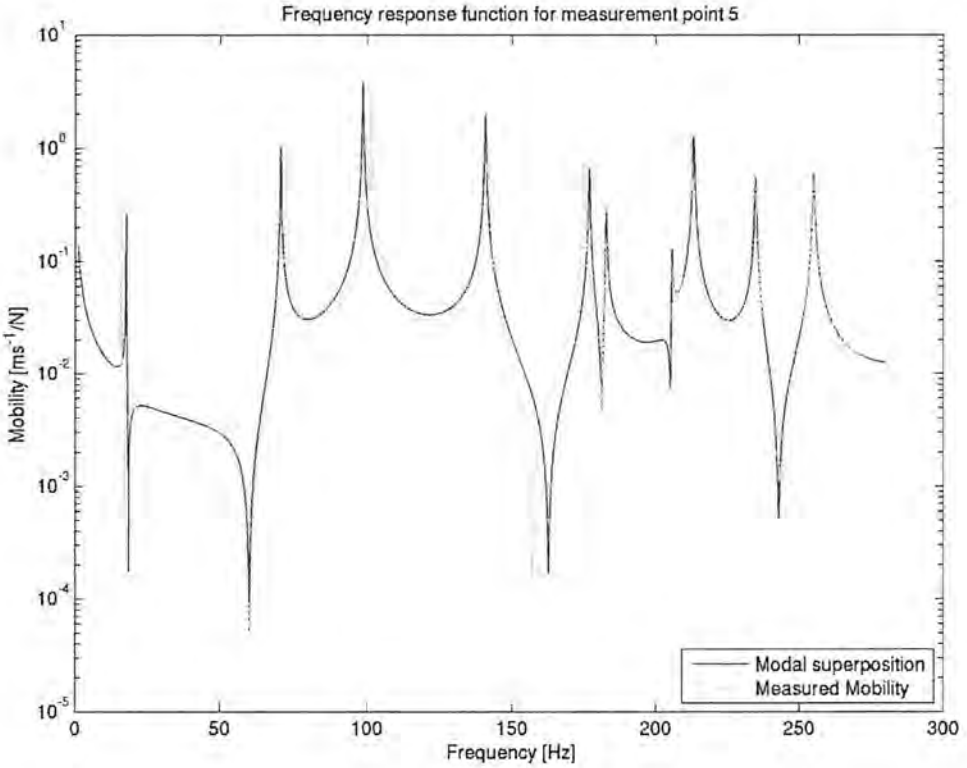

Figure E27: Frequency response for measurement point number five for the lower front plate.

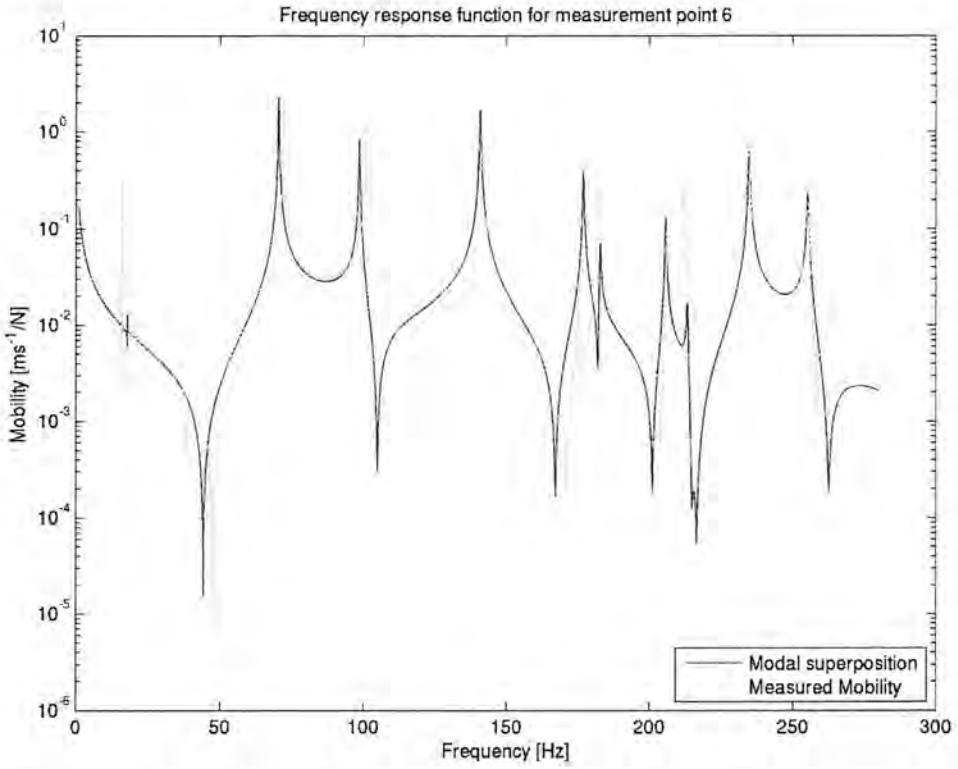

Figure E28: Frequency response for measurement point number six for the lower front plate.

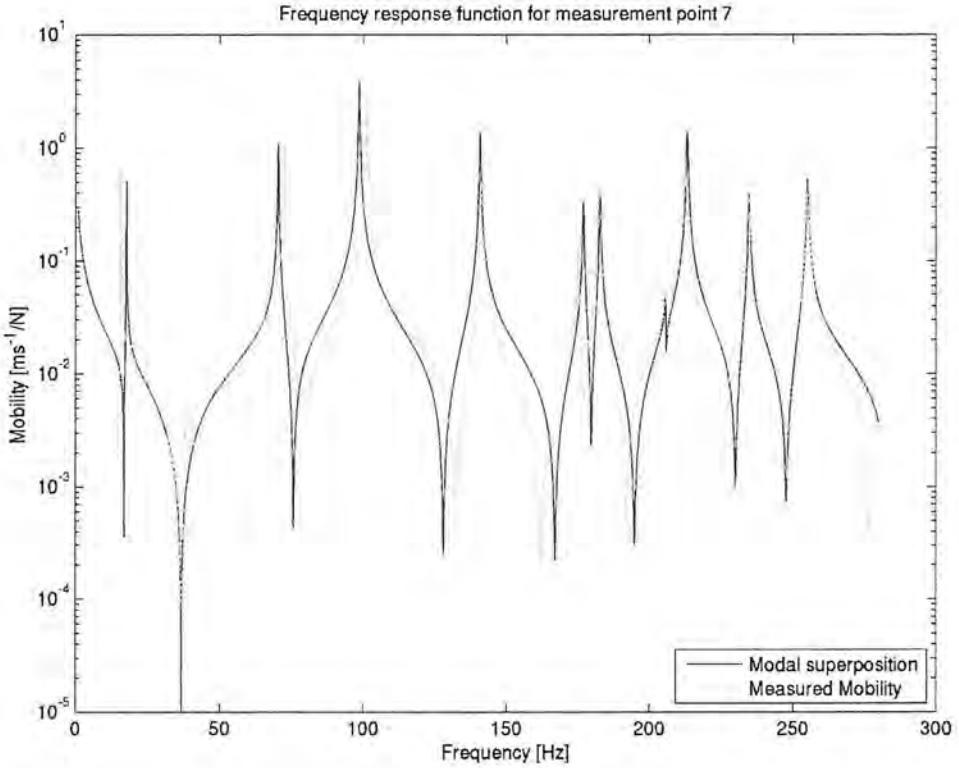

Figure E29: Frequency response for measurement point number seven for the lower front plate.

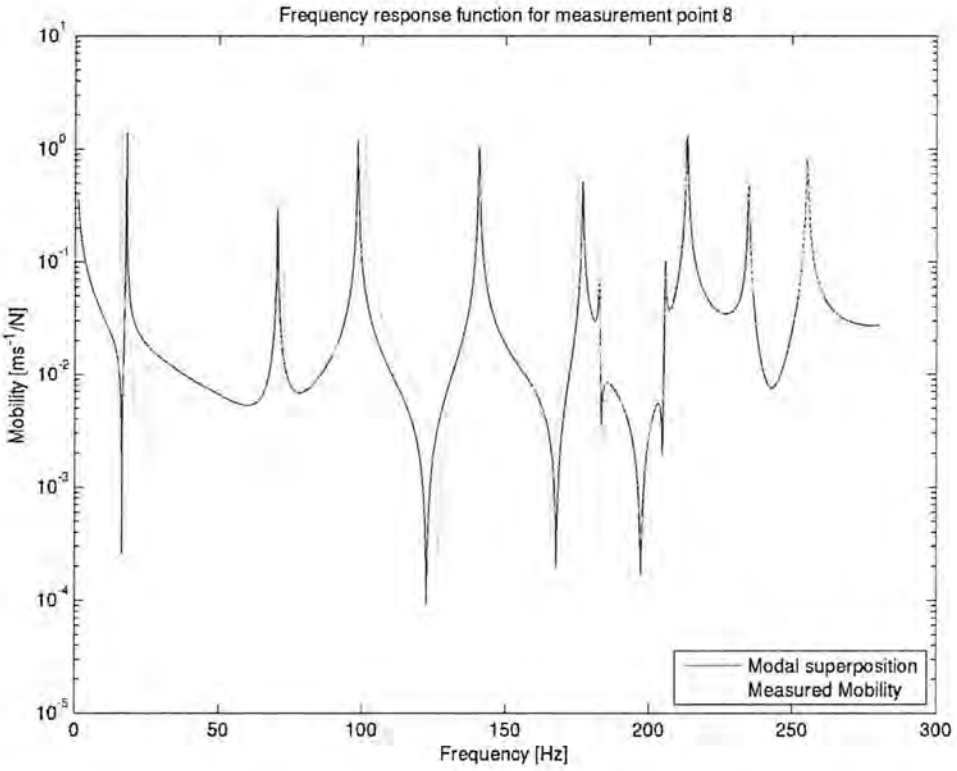

Figure E30: Frequency response for measurement point number eight for the lower front plate.

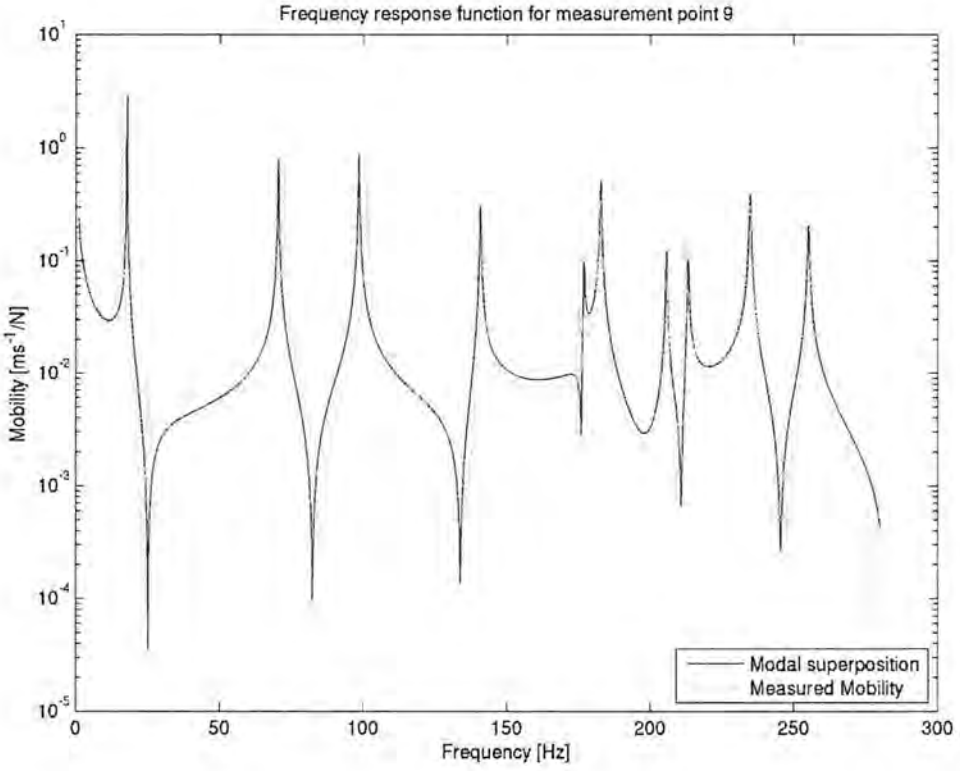

Figure E31: Frequency response for measurement point number nine for the lower front plate.

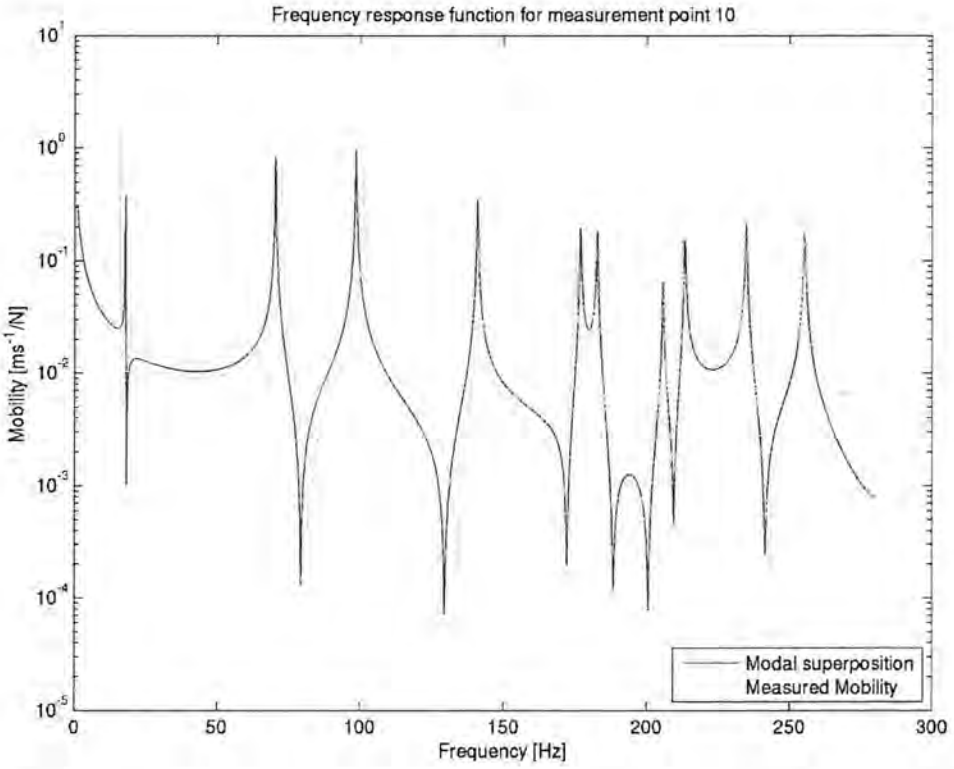

Figure E32: Frequency response for measurement point number ten for the lower front plate.

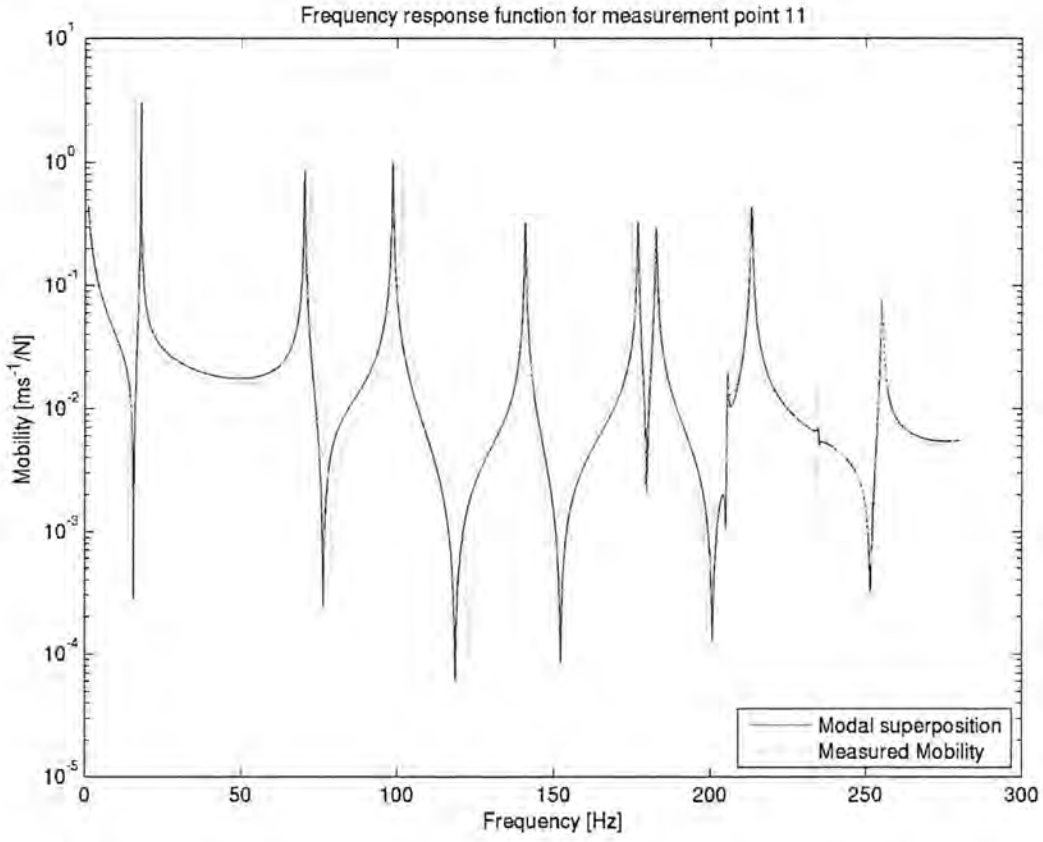

Figure E33: Frequency response for measurement point number eleven for the lower front plate.

E.4 – Electric bridge

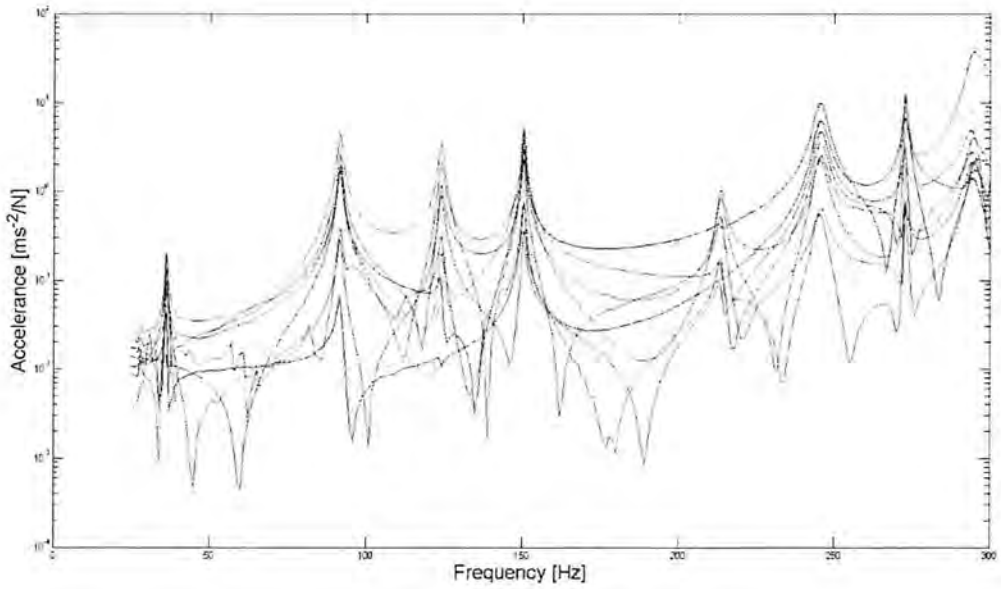

Figure E34: Frequency response function number one for the electric bridge.

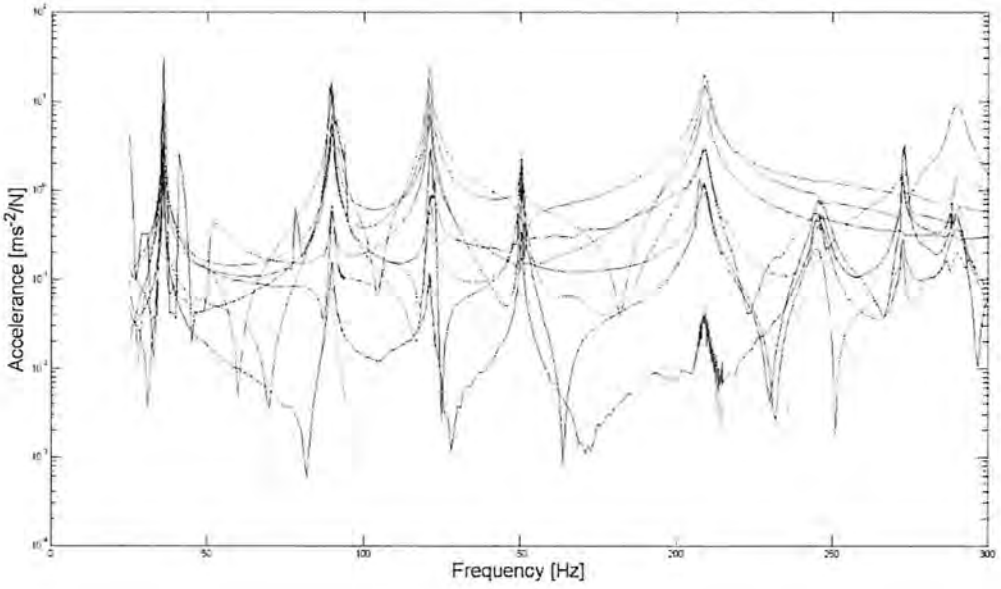

Figure E35: Frequency response function number two for the electric bridge.

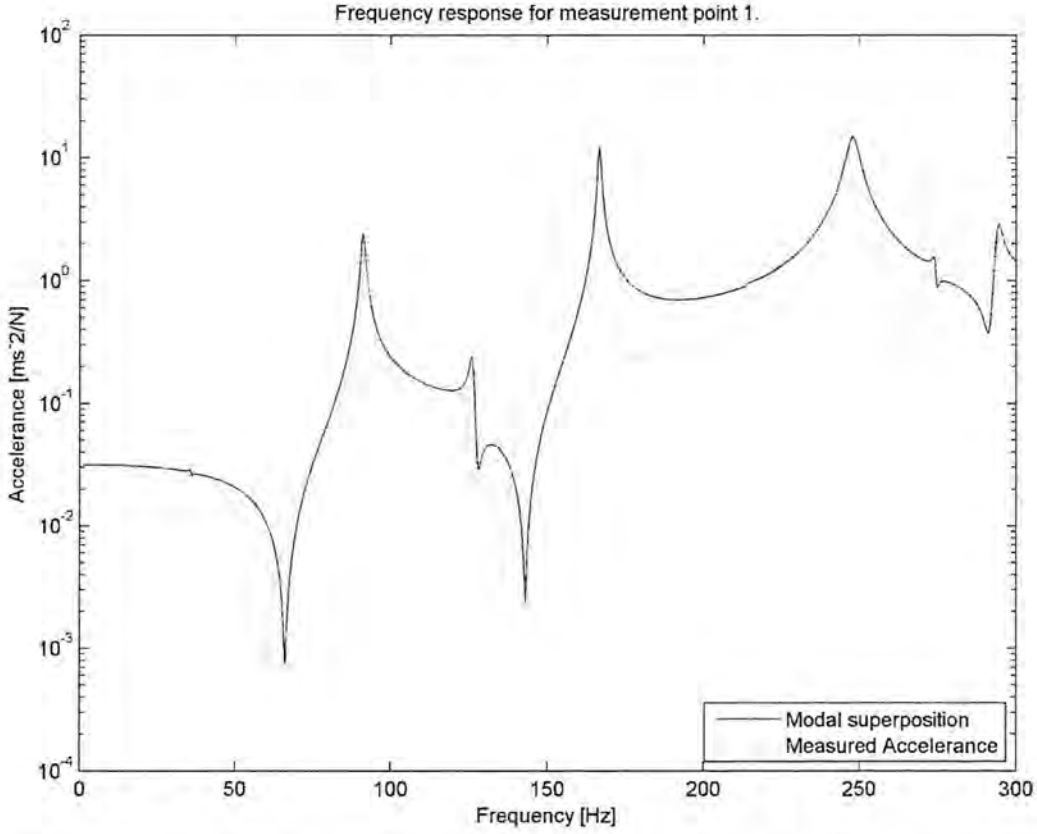

Figure E36: Frequency response for measurement point number one for the electric bridge.

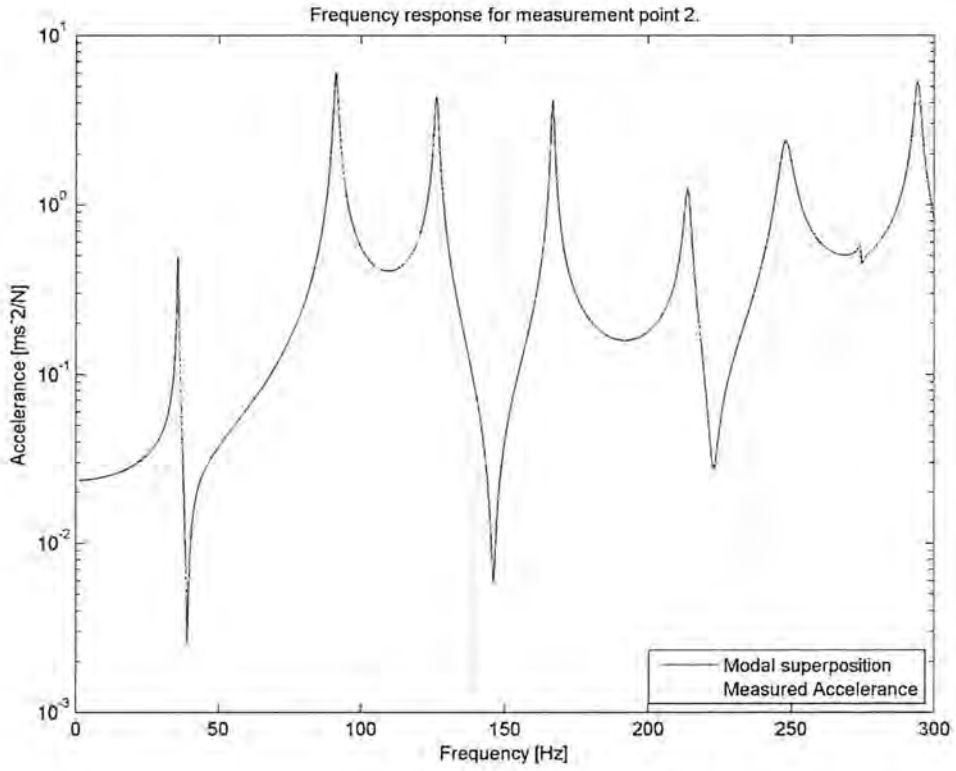

Figure E37: Frequency response for measurement point number two for the electric bridge.

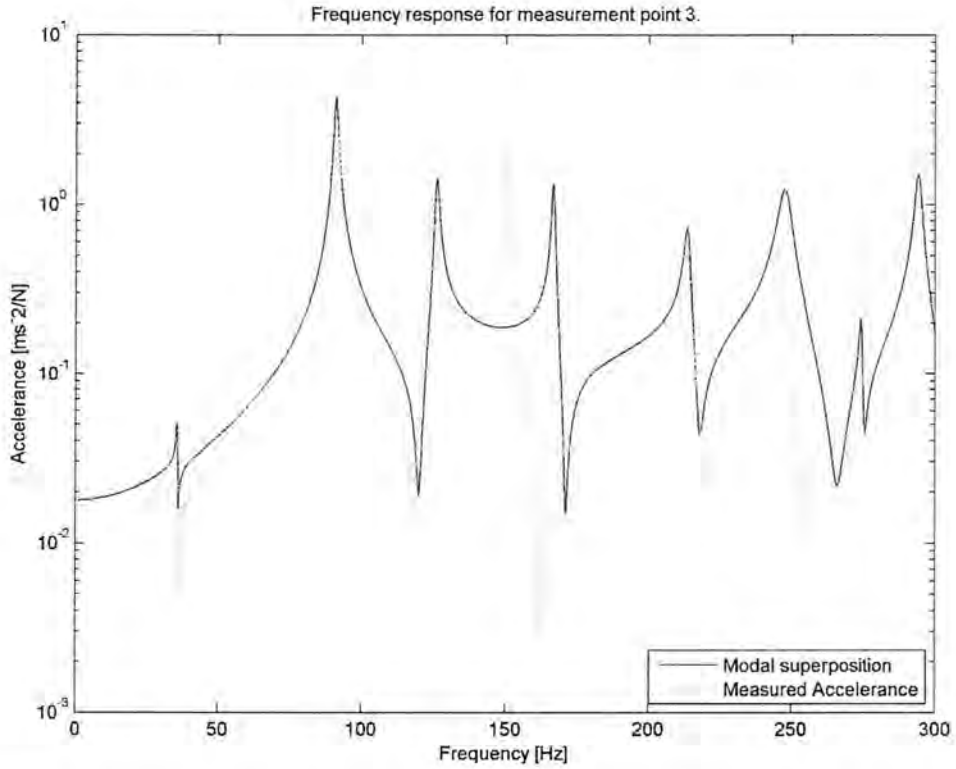

Figure E38: Frequency response for measurement point number three for the electric bridge.

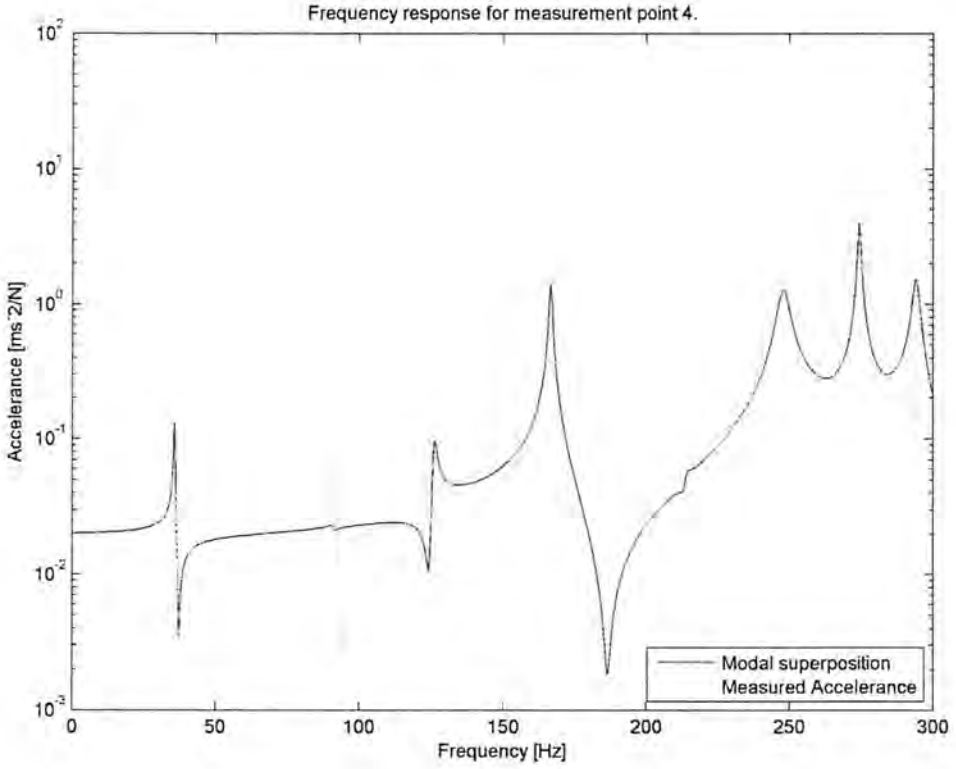

Figure E39: Frequency response for measurement point number four for the electric bridge.

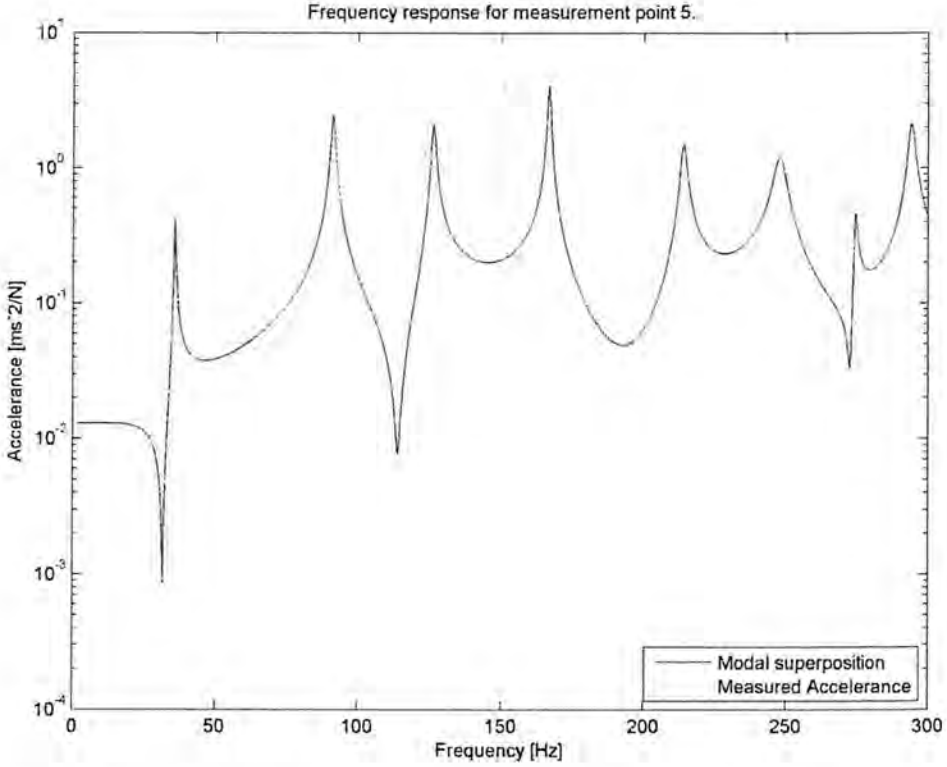

Figure E40: Frequency response for measurement point number five for the electric bridge.

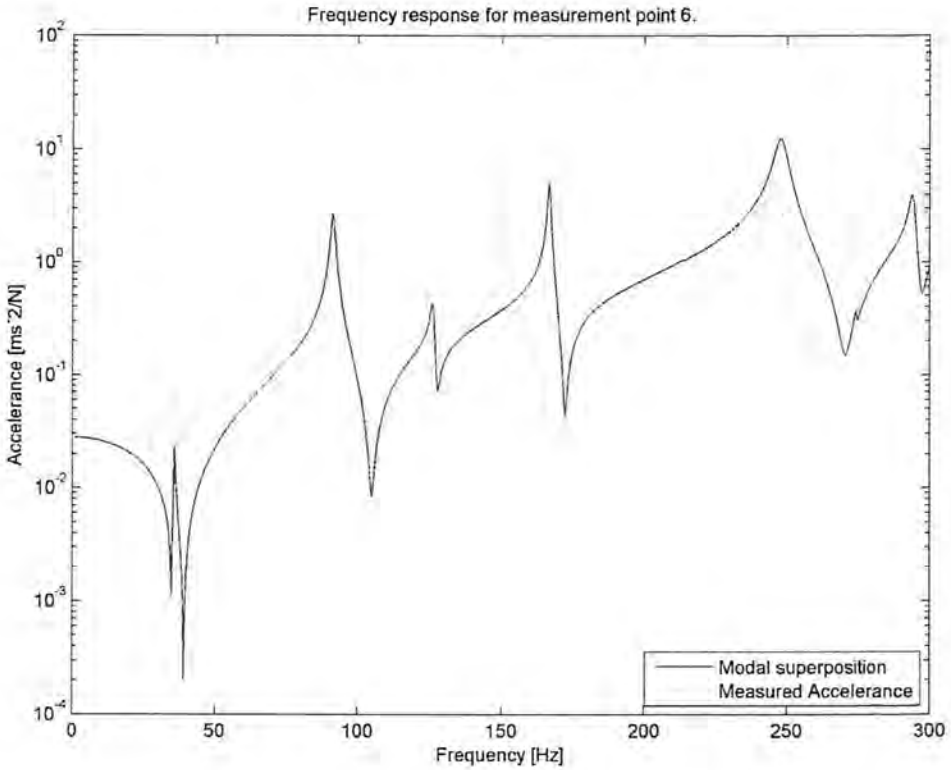

Figure E41: Frequency response for measurement point number six for the electric bridge.

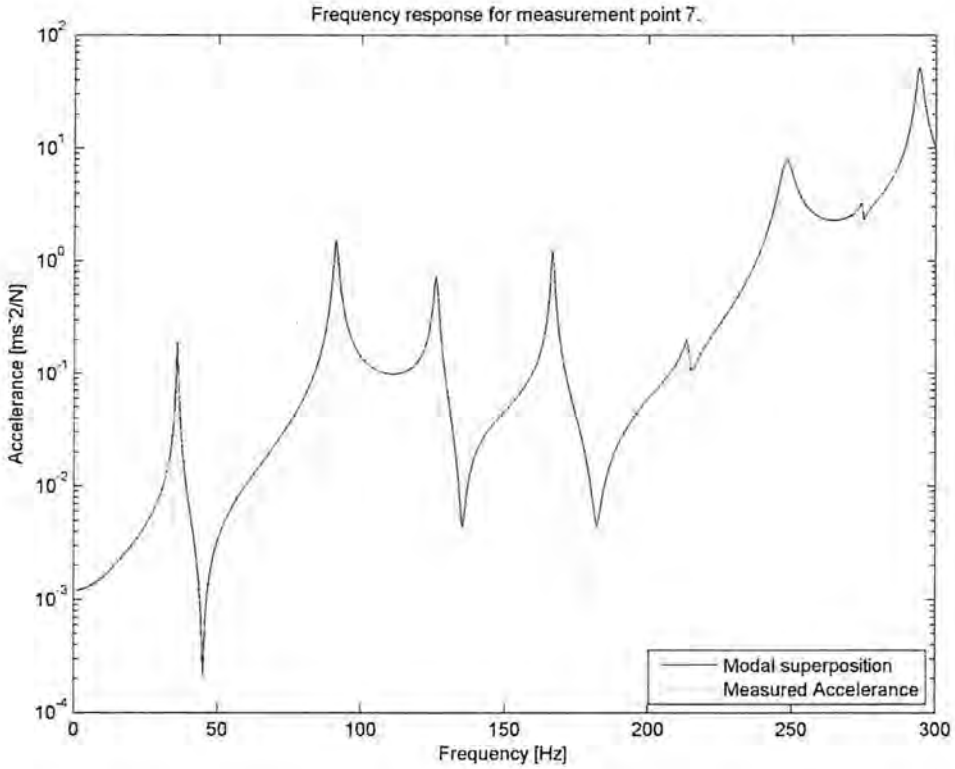

Figure E42: Frequency response for measurement point number seven for the electric bridge.

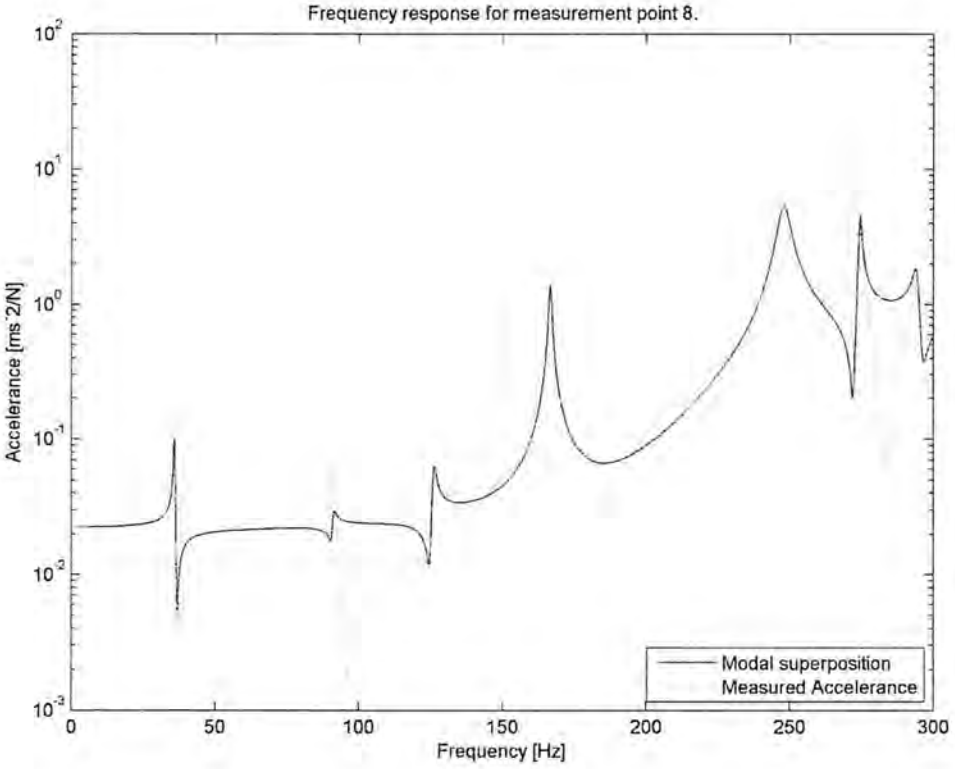

Figure E43: Frequency response for measurement point number eight for the electric bridge.

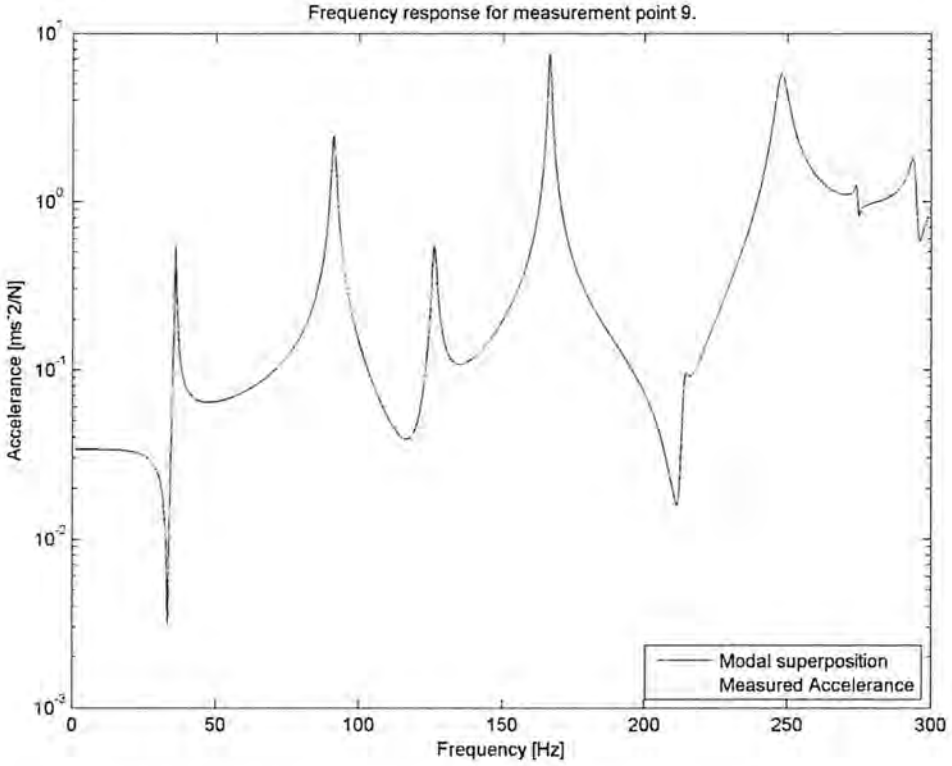

Figure E44: Frequency response for measurement point number nine for the electric bridge.

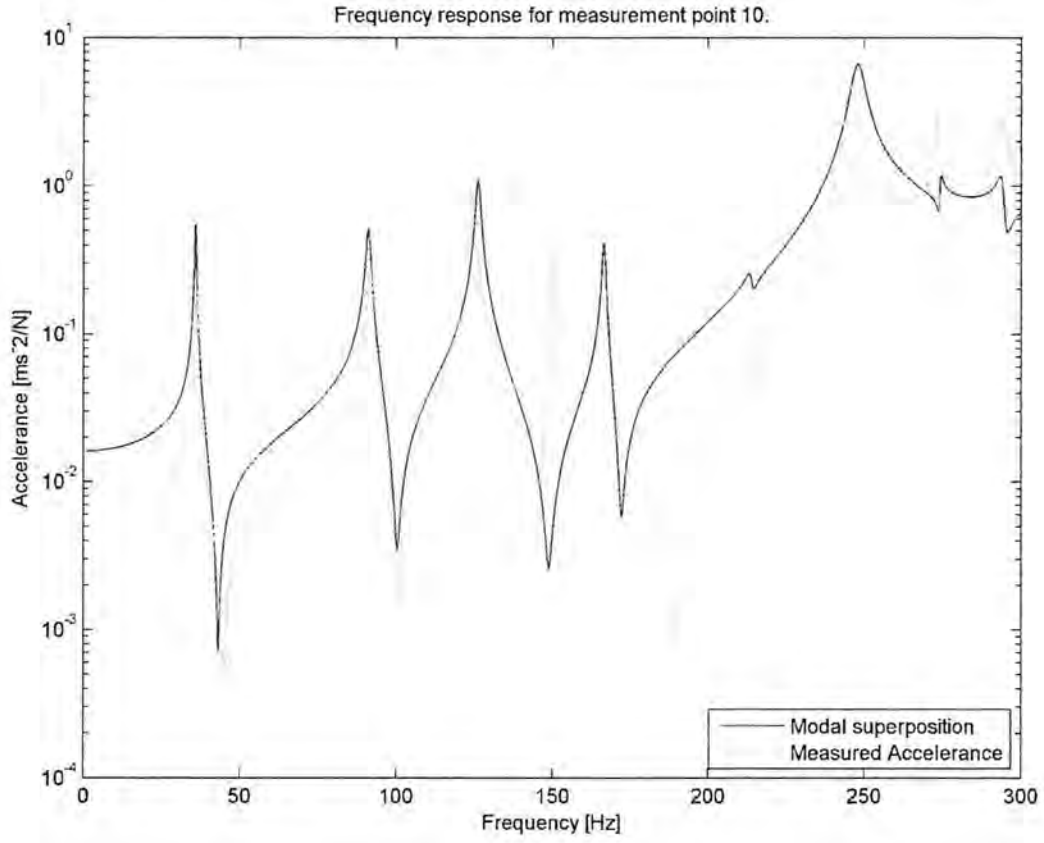

Figure E45: Frequency response for measurement point number ten for the electric bridge.

E.5 – Back plate

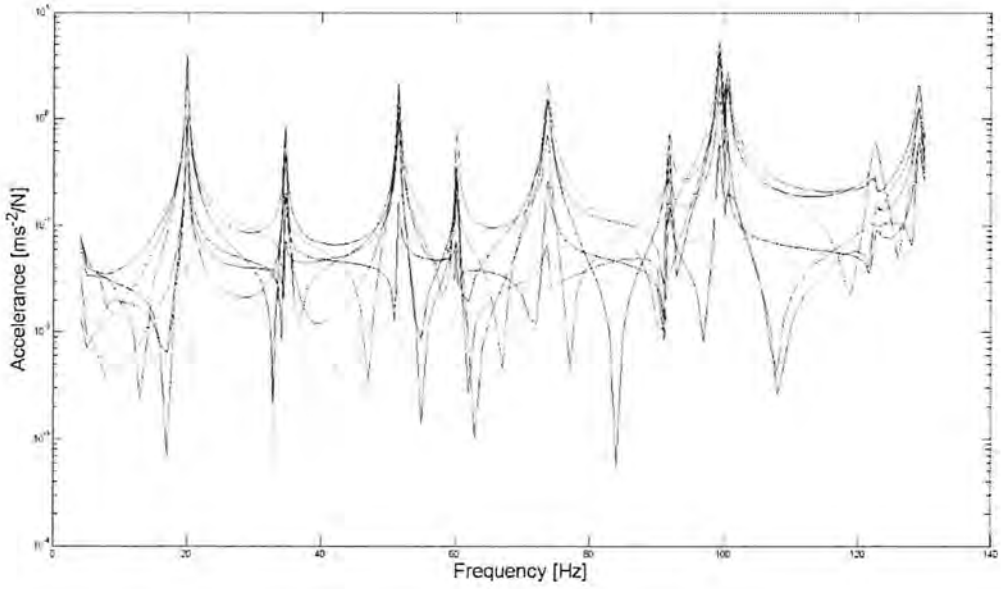

Figure E46: Frequency response function number one for the back plate.

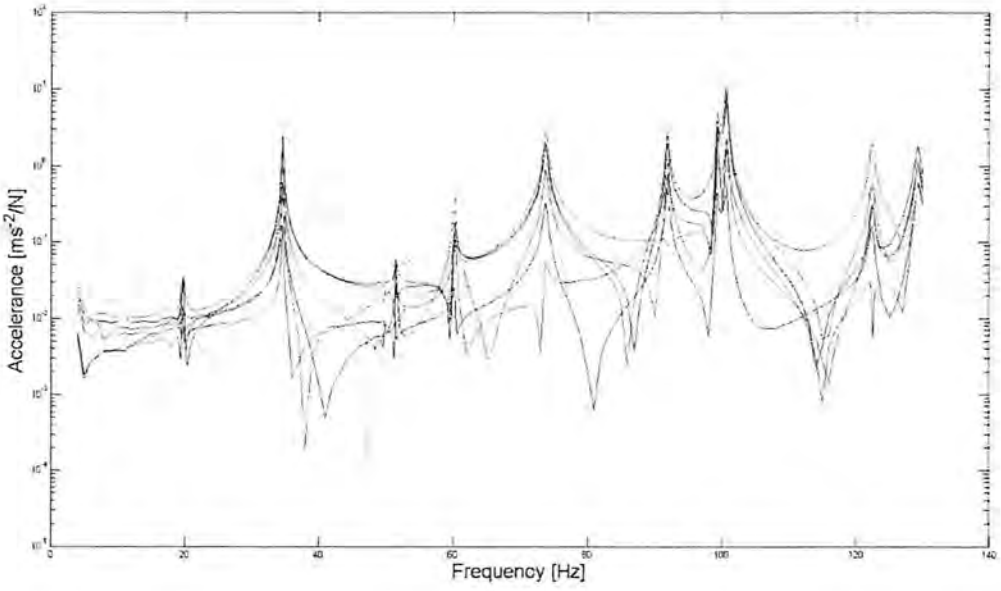

Figure E47: Frequency response function number two for the back plate.

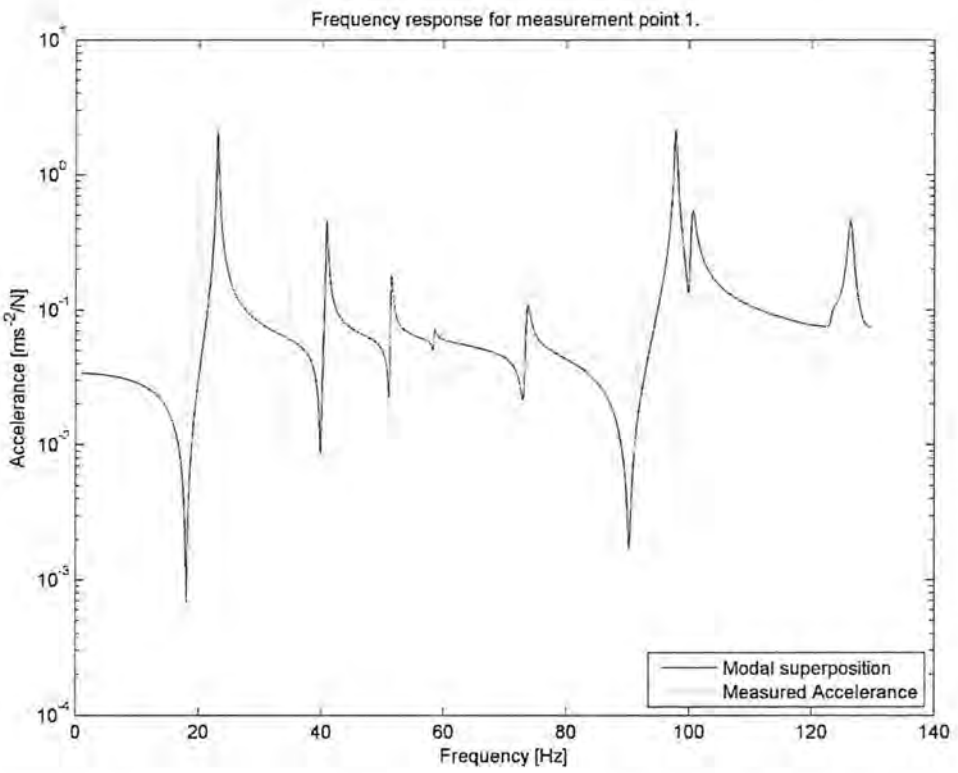

Figure E48: Frequency response for measurement point number one for the back plate.

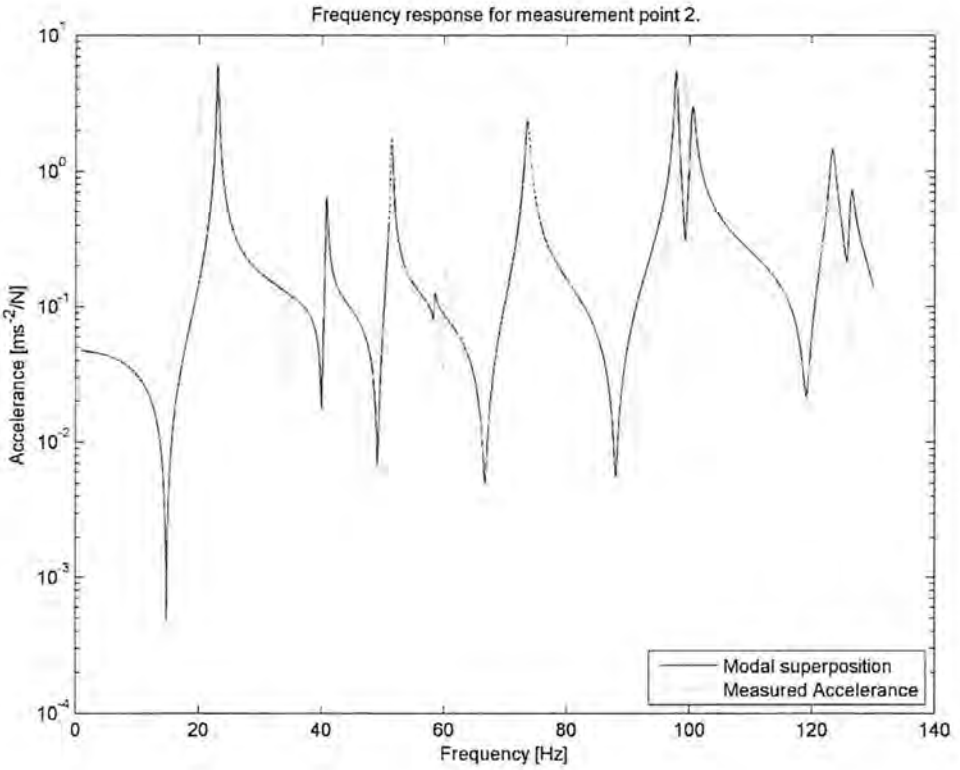

Figure E49: Frequency response for measurement point number two for the back plate.

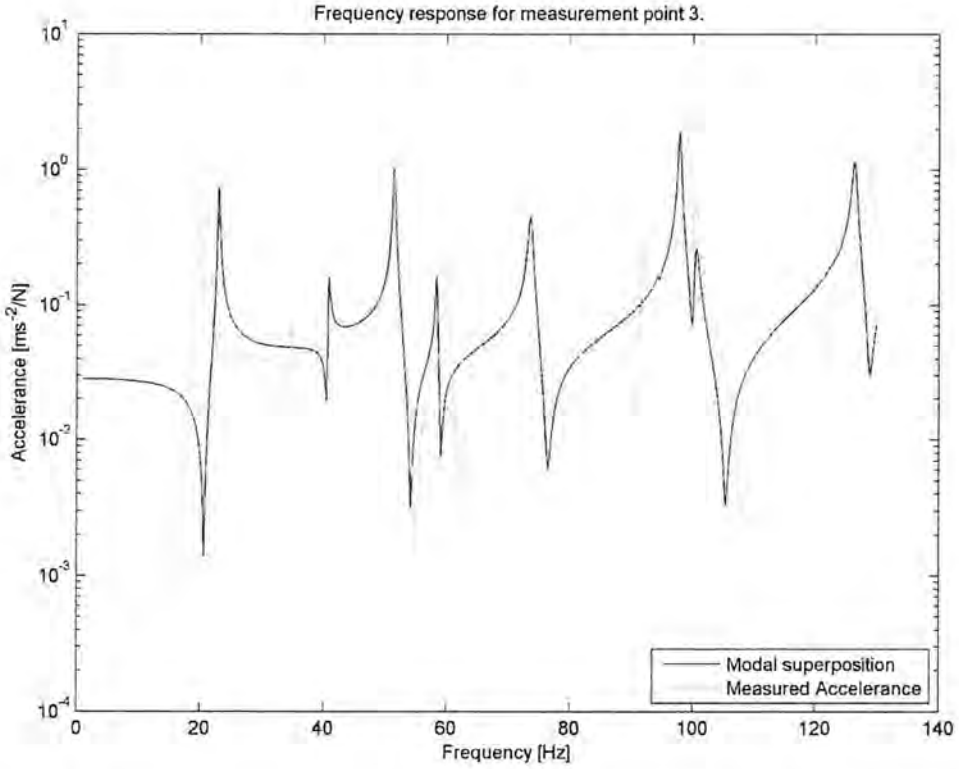

Figure E50: Frequency response for measurement point number three for the back plate.

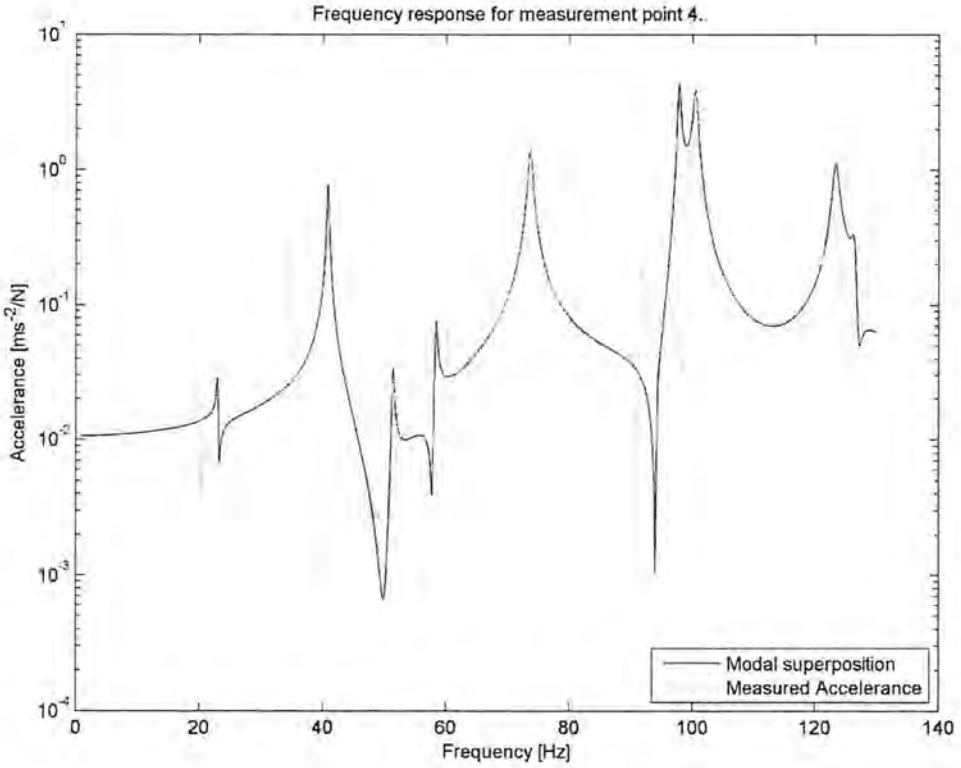

Figure E51: Frequency response for measurement point number four for the back plate.

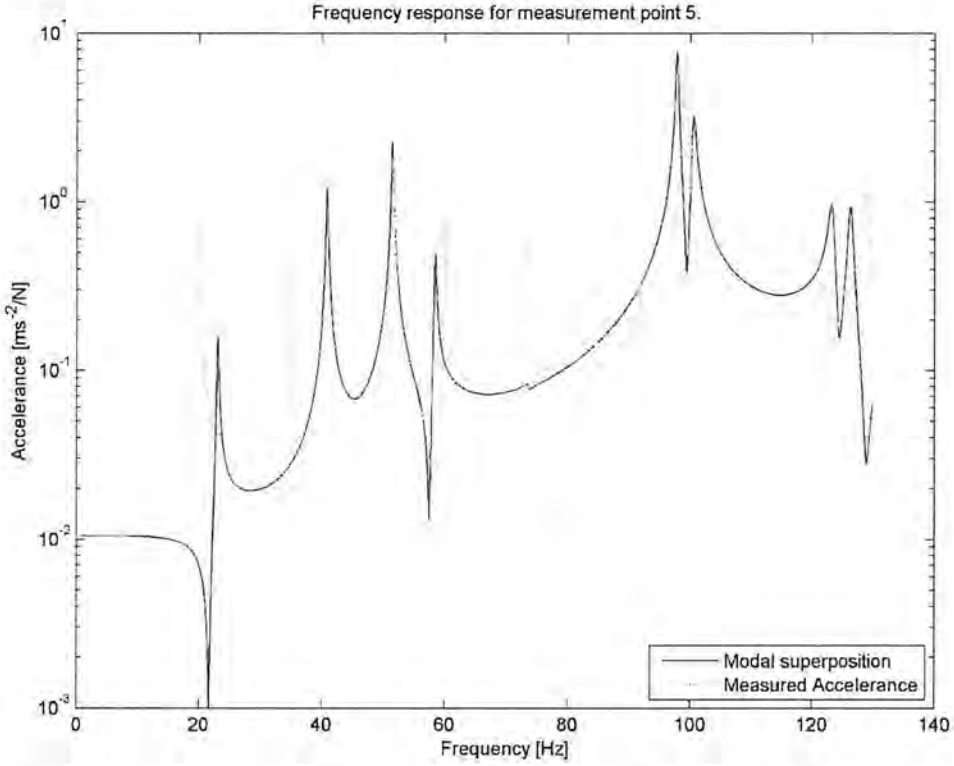

Figure E52: Frequency response for measurement point number five for the back plate.

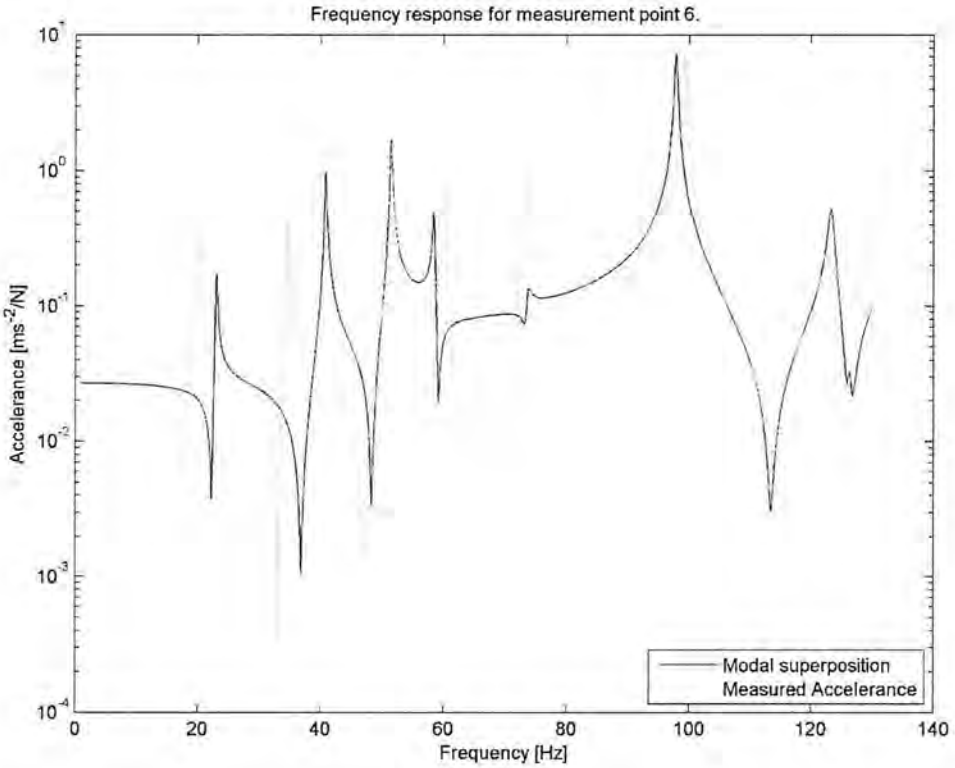

Figure E53: Frequency response for measurement point number six for the back plate.

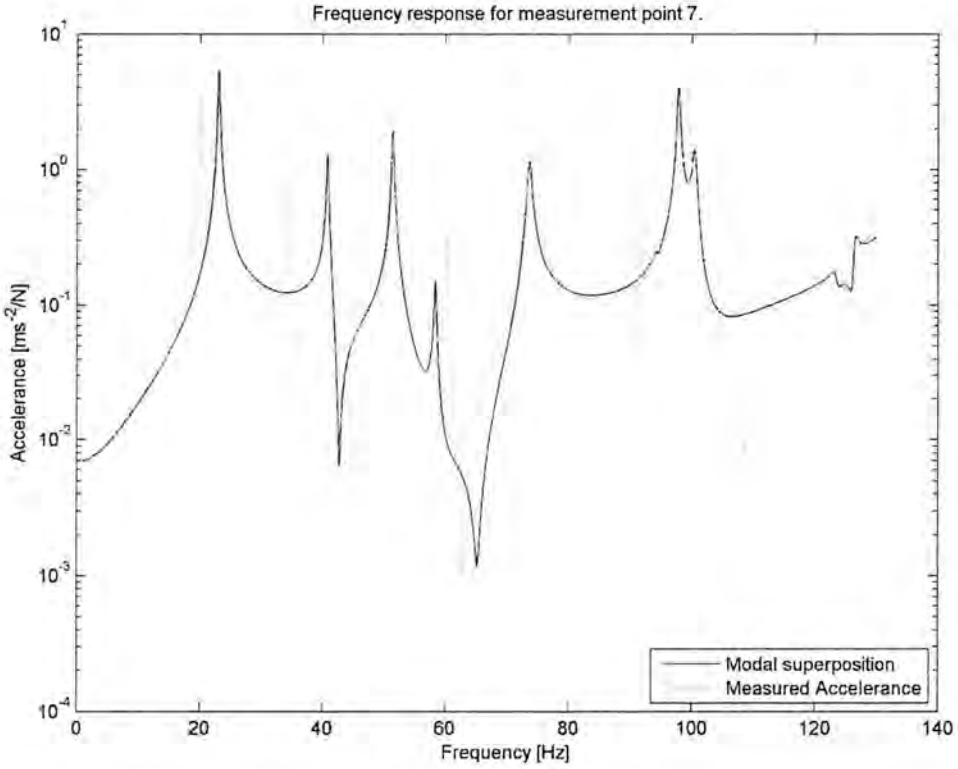

Figure E54: Frequency response for measurement point number seven for the back plate.

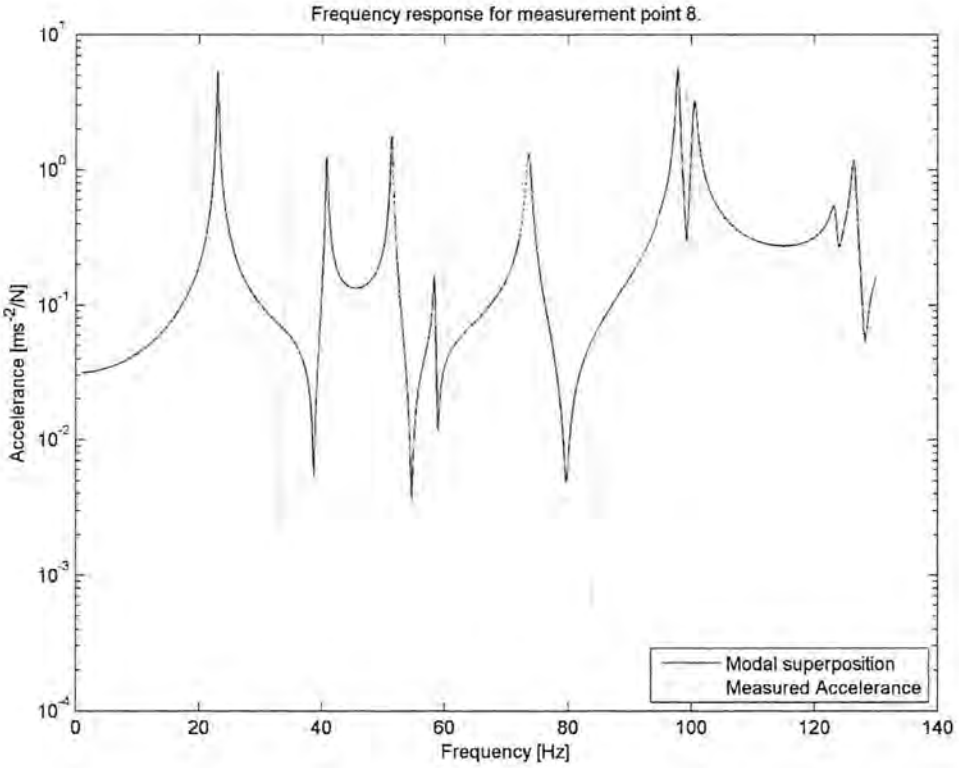

Figure E55: Frequency response for measurement point number eight for the back plate.

E.6 – Assembled steel shell

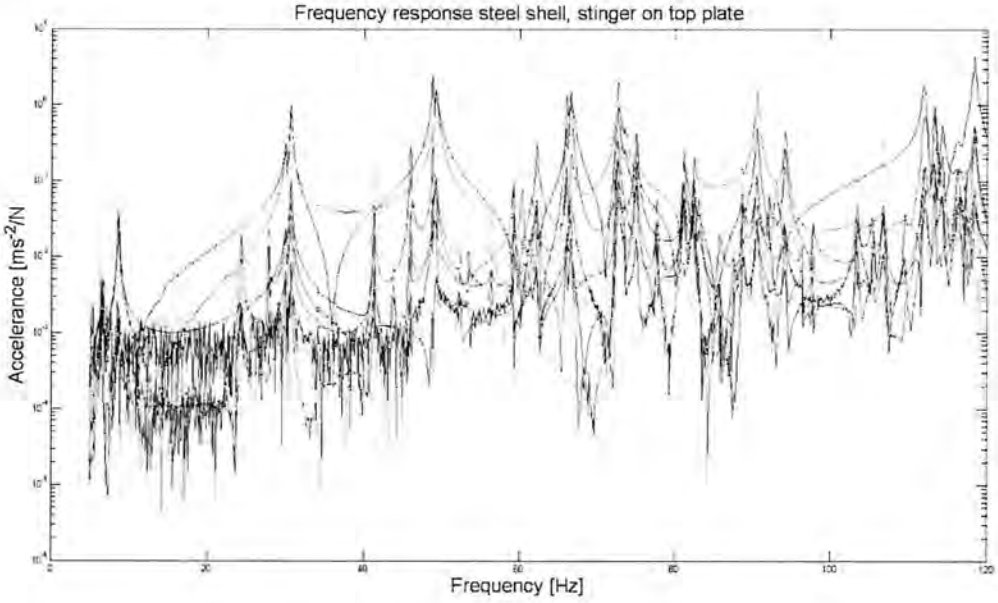

Figure E56: Frequency response function number one for the steel shell.

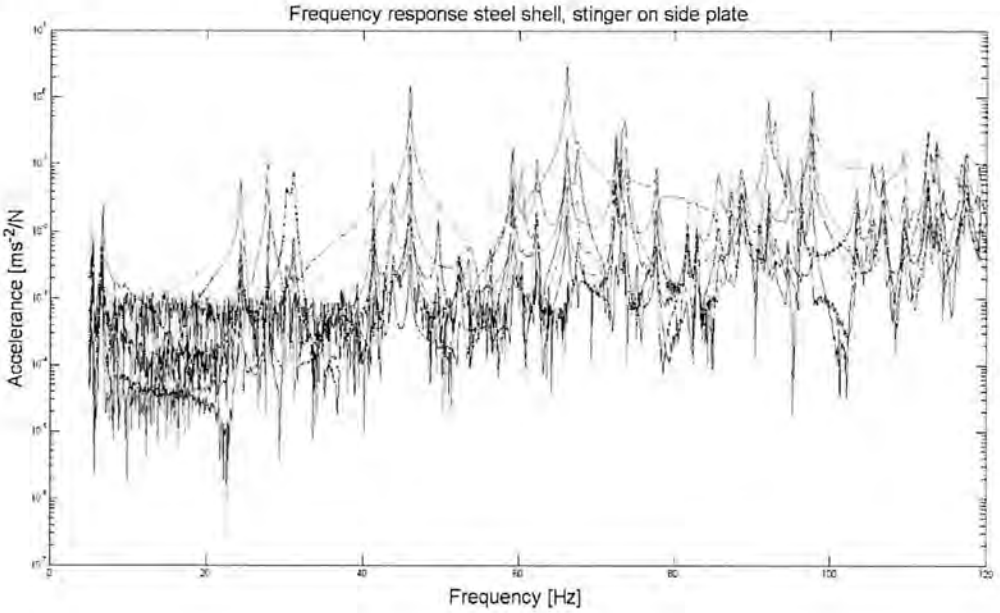

Figure E57: Frequency response function number two for the steel shell.

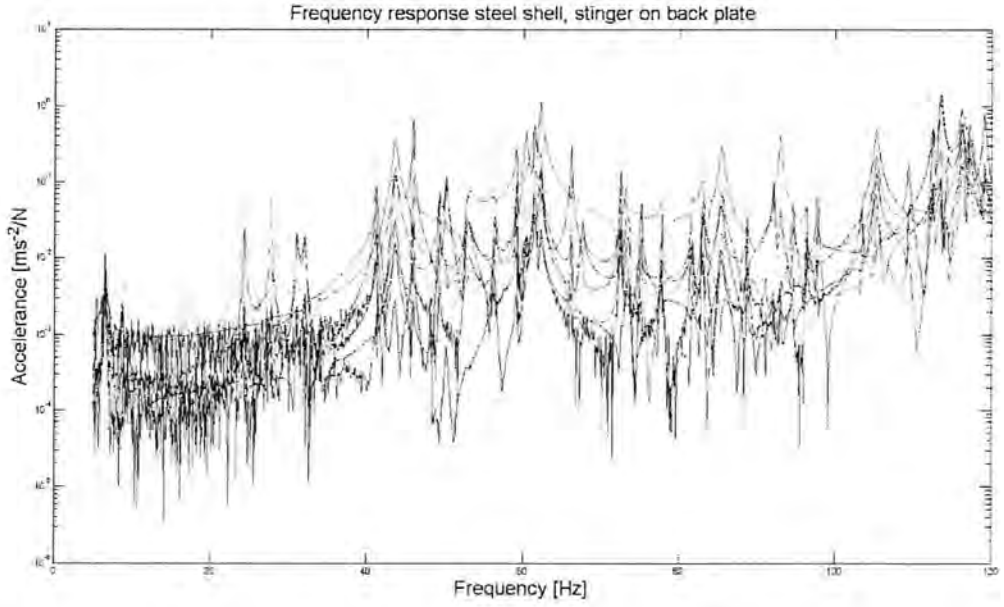

Figure E58: Frequency response function number three for the steel shell.

Appendix F – Mode shapes of steel shell

Here are the first eight mode shapes for the steel shell presented.

Figure F1: Mode 1 of the steel shell.

Figure F2: Mode 2 of the steel shell.

Figure F3: Mode 3 of the steel shell.

Figure F4: Mode 4 of the steel shell.

Figure F5: Mode 5 of the steel shell.

Figure F6: Mode 6 of the steel shell.

Figure F7: Mode 7 of the steel shell.

Figure F8: Mode 8 of the steel shell.

Appendix G – Spin up tests

Here results from measurements are presented against each other together with mode shapes.

G.1 – Modal analysis

Figure G1: Mode 1 of entire washing machine.

Figure G2: Mode 2 of entire washing machine.

Figure G3: Mode 3 of entire washing machine

Figure G4: Mode 4 of entire washing machine.

Figure G5: Mode 5 of entire washing machine.

Figure G6: Mode 6 of entire washing machine.

Figure G7: Mode 7 of entire washing machine.

Figure G8: Mode 8 of entire washing machine.

Figure G9: Mode 9 of entire washing machine.

Figure G10: Mode 10 of entire washing machine.

G.2 - Comparison between experiment one and two

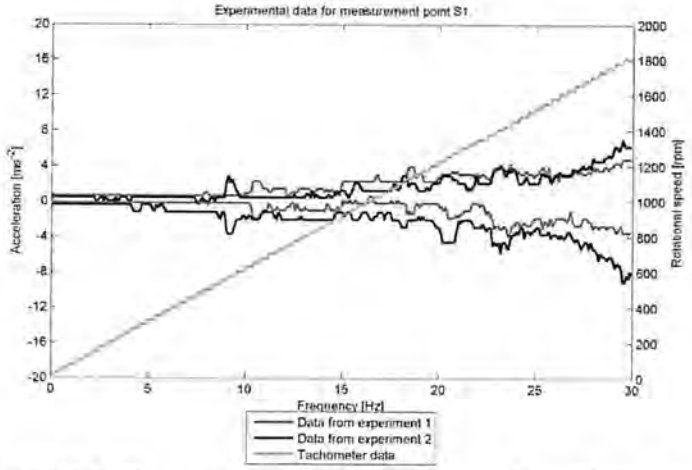

Figure G11: Comparison between measured accelerations for experiment one and two for measurement point S1.

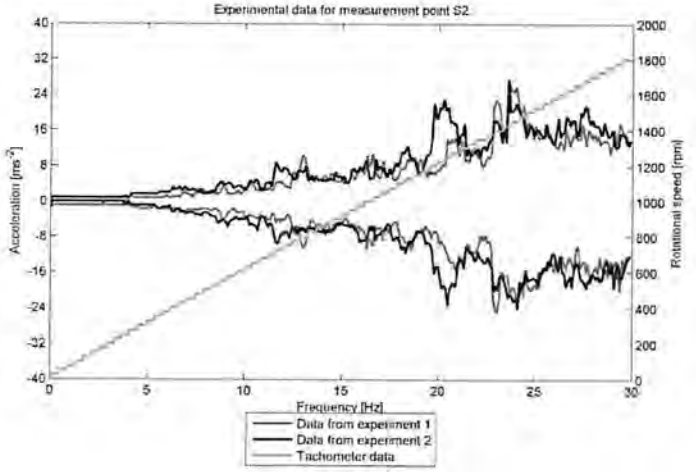

Figure G12: Comparison between measured accelerations for experiment one and two for measurement point S2.

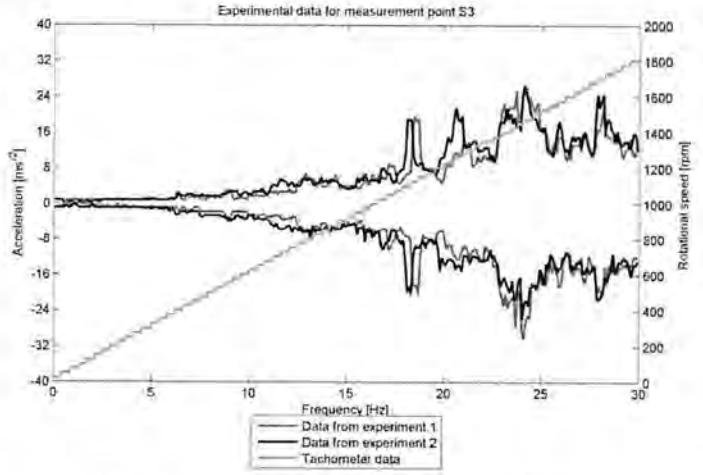

Figure G13: Comparison between measured accelerations for experiment one and two for measurement point S3.

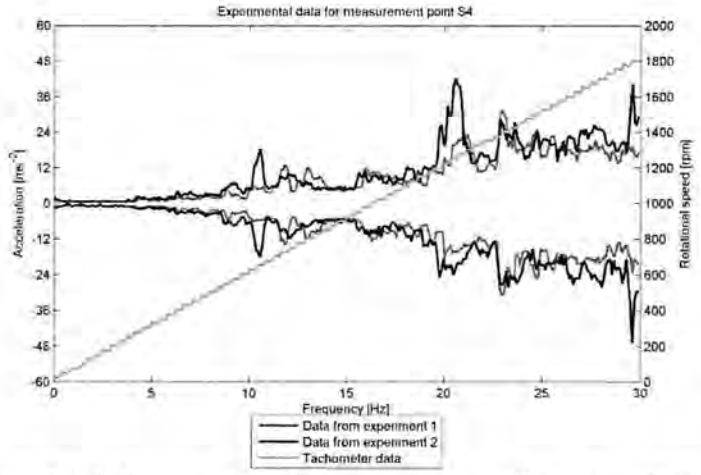

Figure G14: Comparison between measured accelerations for experiment one and two for measurement point S4.

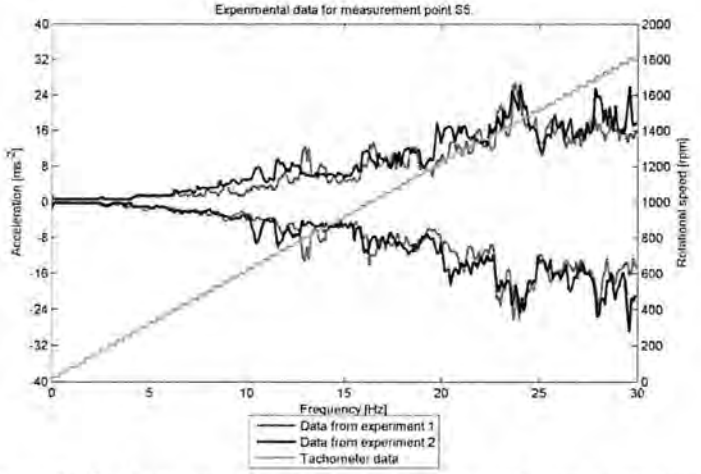

Figure G15: Comparison between measured accelerations for experiment one and two for measurement point S5

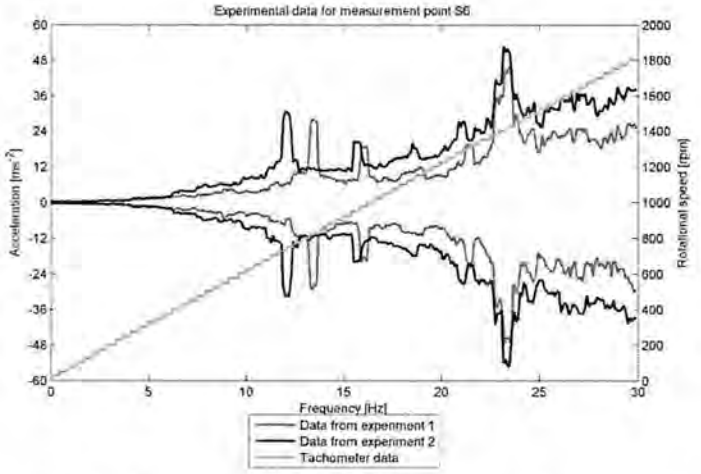

Figure G16: Comparison between measured accelerations for experiment one and two for measurement point S6

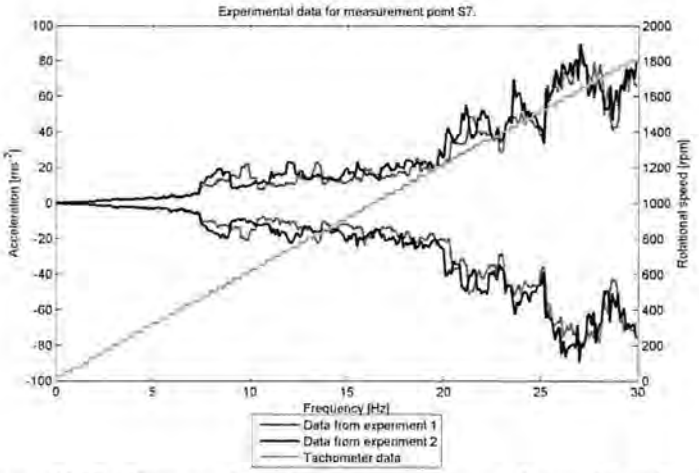

Figure G17: Comparison between measured accelerations for experiment one and two for measurement point S7.

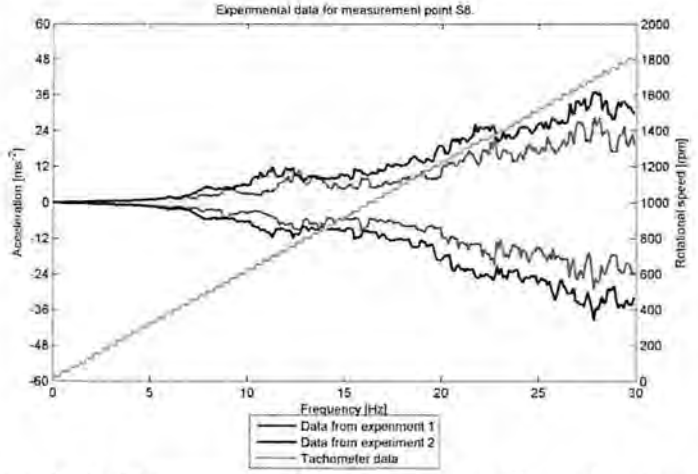

Figure G18: Comparison between measured accelerations for experiment one and two for measurement point S8.

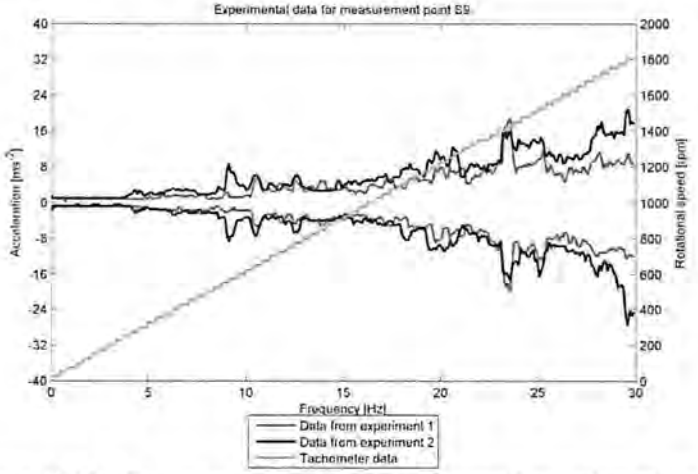

Figure G19: Comparison between measured accelerations for experiment one and two for measurement point S9.

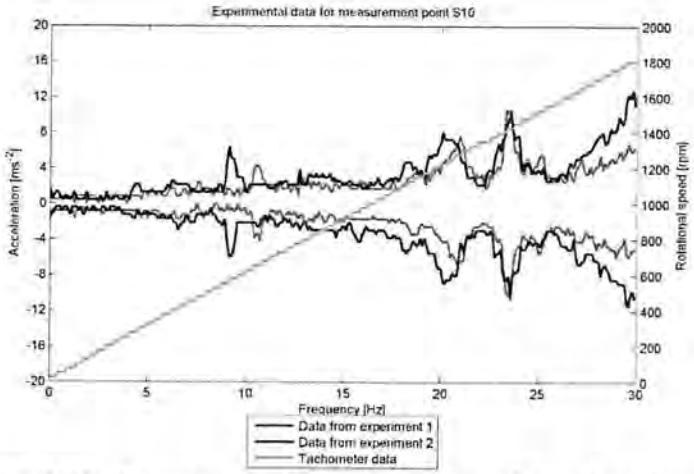

Figure G20: Comparison between measured accelerations for experiment one and two for measurement point S10.

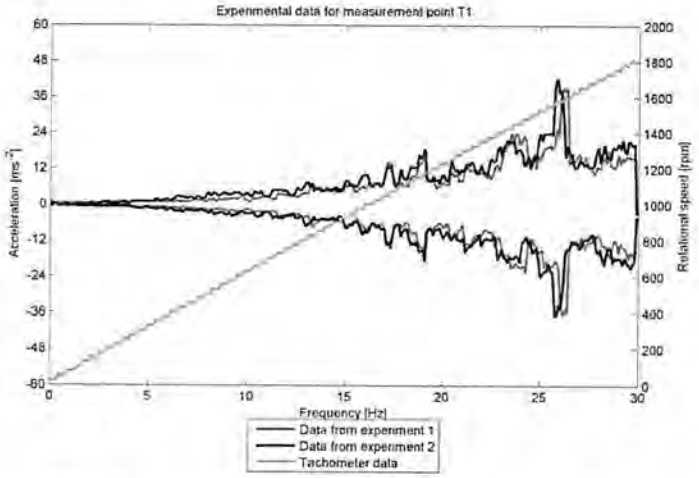

Figure G21: Comparison between measured accelerations for experiment one and two for measurement point T1.

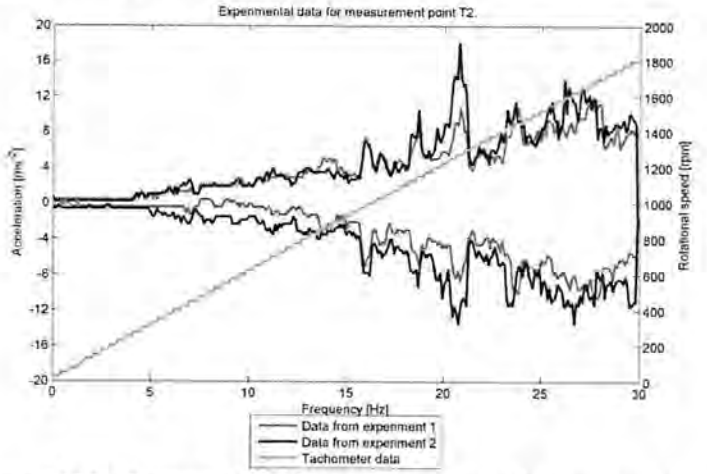

Figure G22: Comparison between measured accelerations for experiment one and two for measurement point T2.

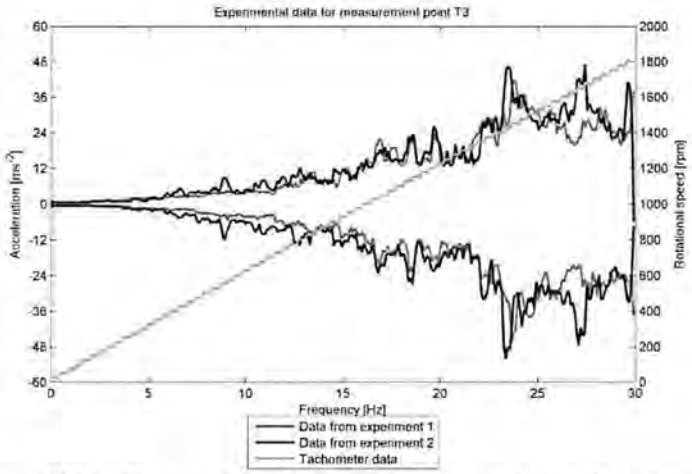

Figure G23: Comparison between measured accelerations for experiment one and two for measurement point T3.

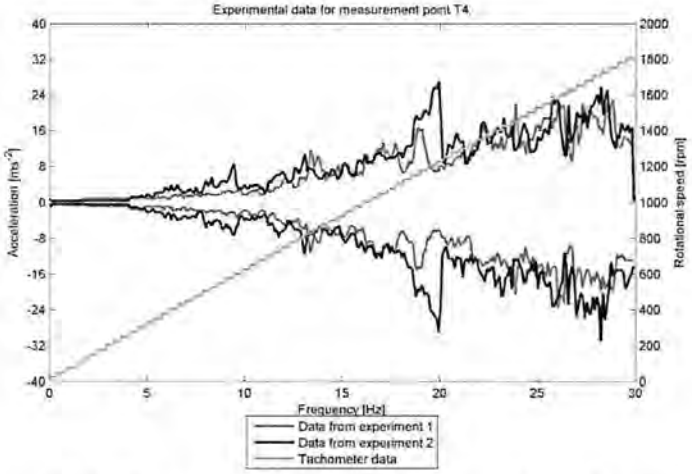

Figure G24: Comparison between measured accelerations for experiment one and two for measurement point T4.

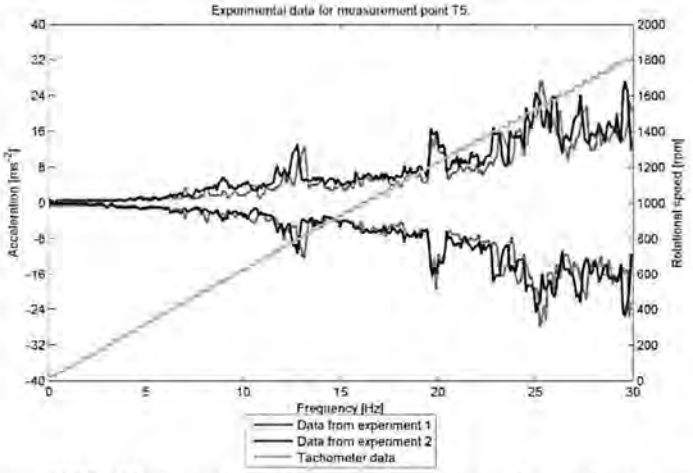

Figure G25: Comparison between measured accelerations for experiment one and two for measurement point T5.

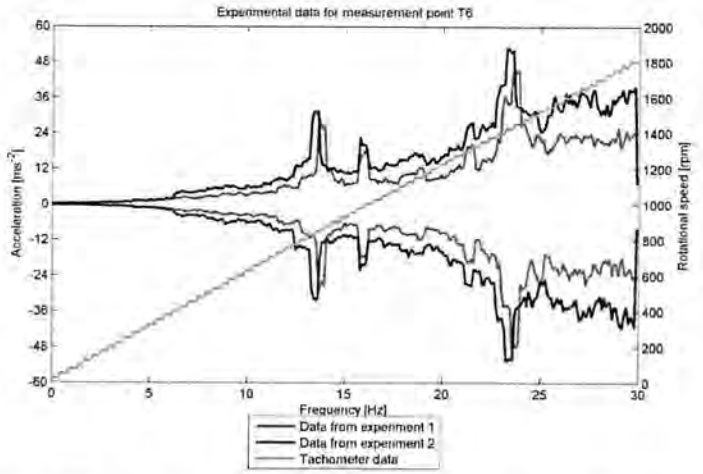

Figure G26: Comparison between measured accelerations for experiment one and two for measurement point T6.

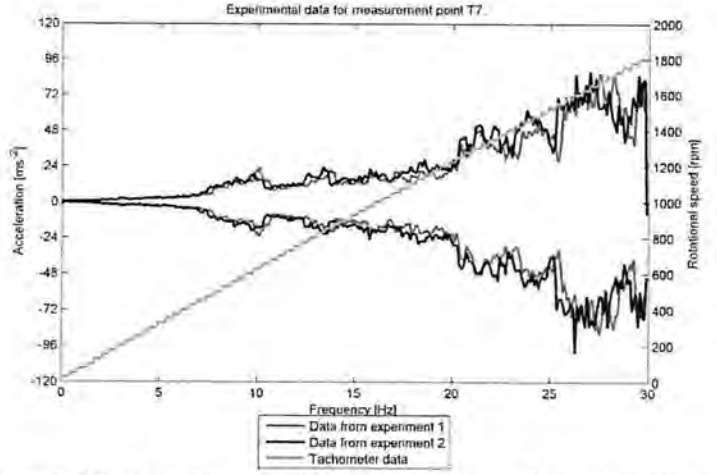

Figure G27: Comparison between measured accelerations for experiment one and two for measurement point T7.

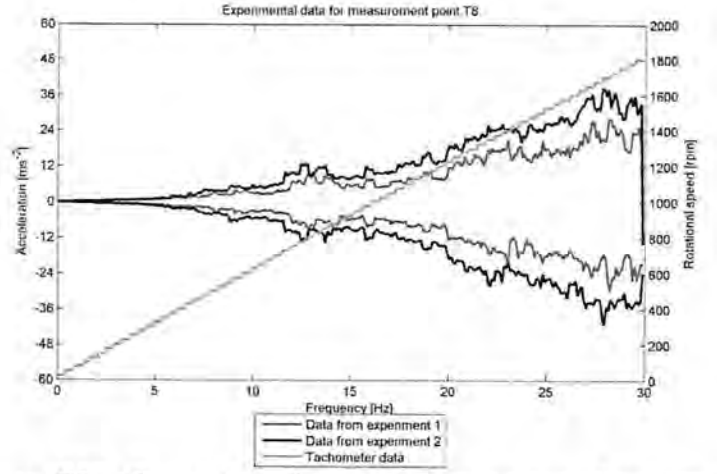

Figure G28: Comparison between measured accelerations for experiment one and two for measurement point T8.

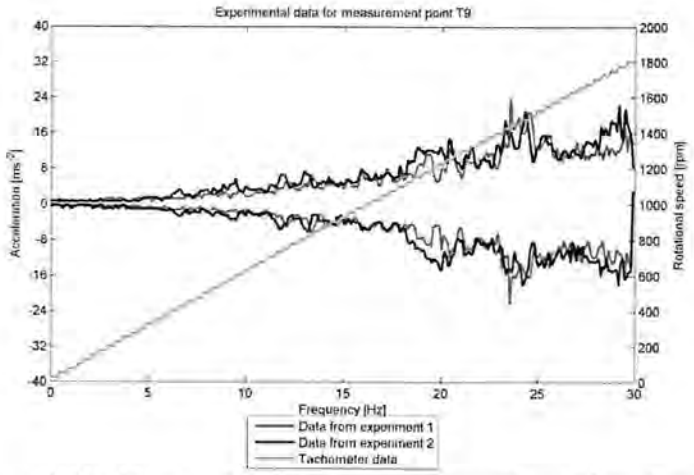

Figure G29: Comparison between measured accelerations for experiment one and two for measurement point T9.

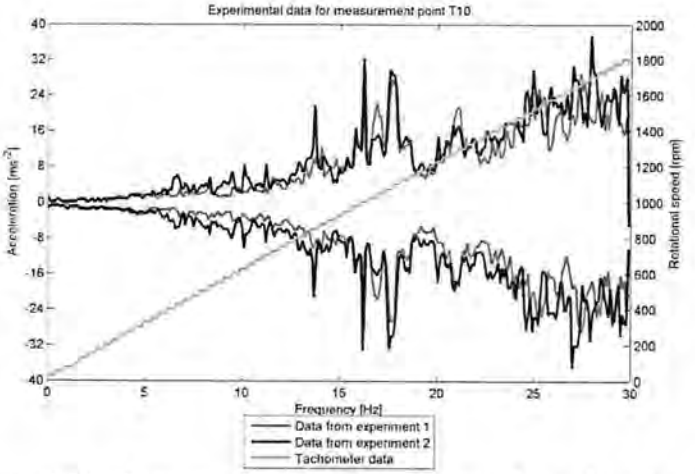

Figure G30: Comparison between measured accelerations for experiment one and two for measurement point T10.

G.3 - Comparison between experiment two and five

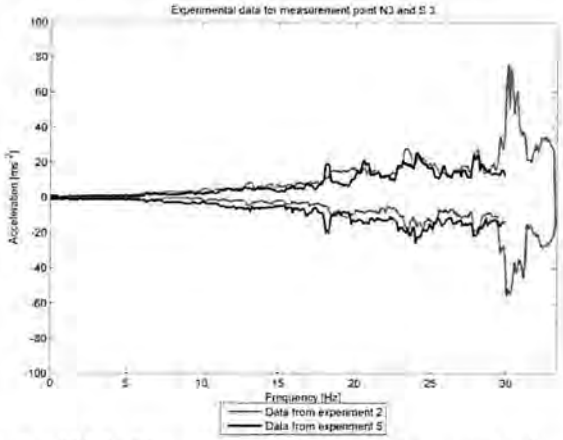

Figure G31: Comparison between measured accelerations for experiment two and five for measurement point N3 and S3.

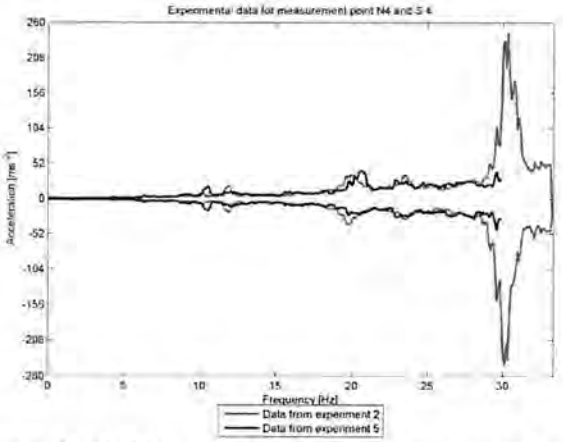

Figure G32: Comparison between measured accelerations for experiment two and five for measurement point N4 and S4.

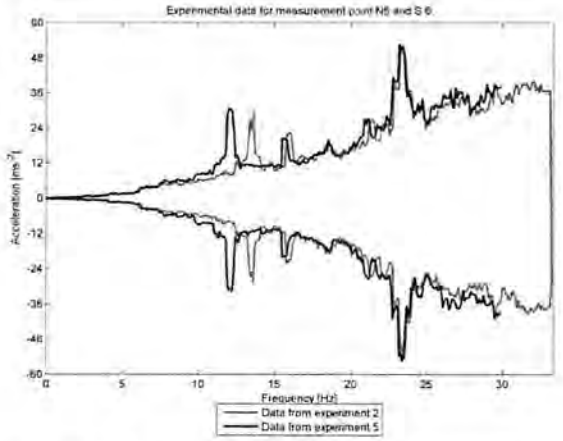

Figure G33: Comparison between measured accelerations for experiment two and five for measurement point N6 and S6.

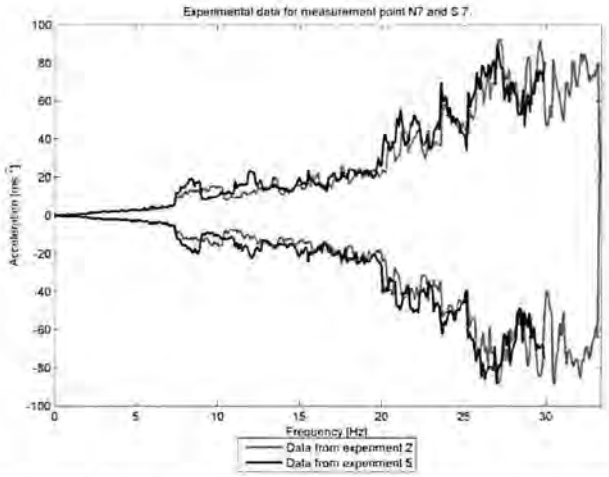

Figure G34: Comparison between measured accelerations for experiment two and five for measurement point N7 and S7.

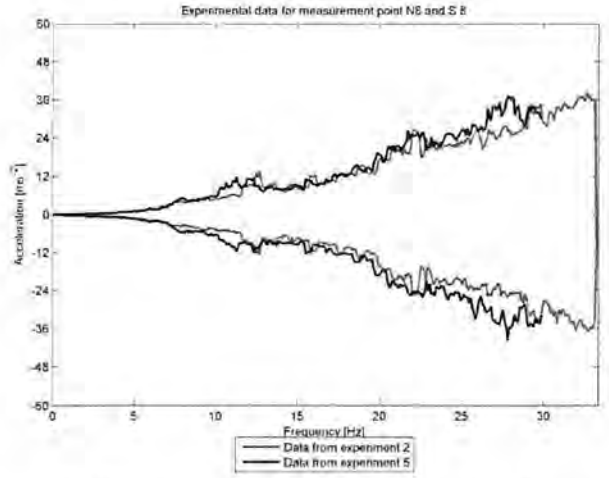

Figure G35: Comparison between measured accelerations for experiment two and five for measurement point N8 and S8.

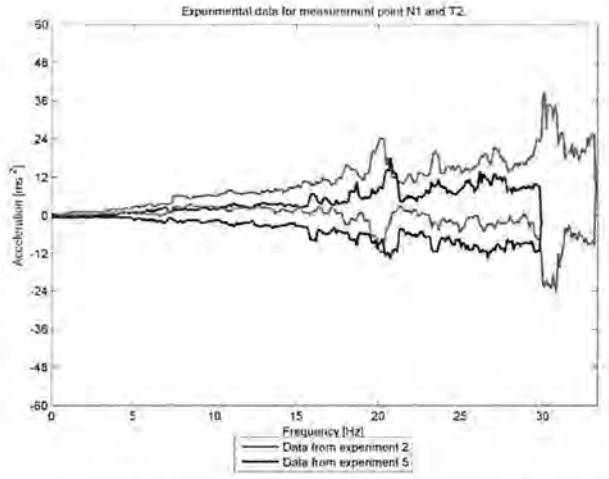

Figure G36: Comparison between measured accelerations for experiment two and five for measurement point N1 and T2.

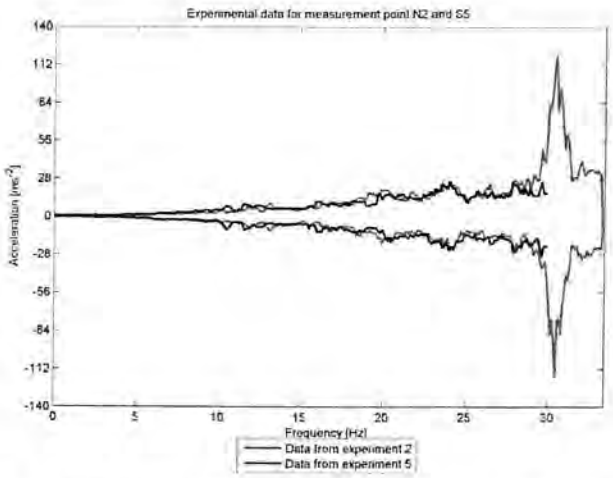

Figure G37: Comparison between measured accelerations for experiment two and five for measurement point N2 and S5.

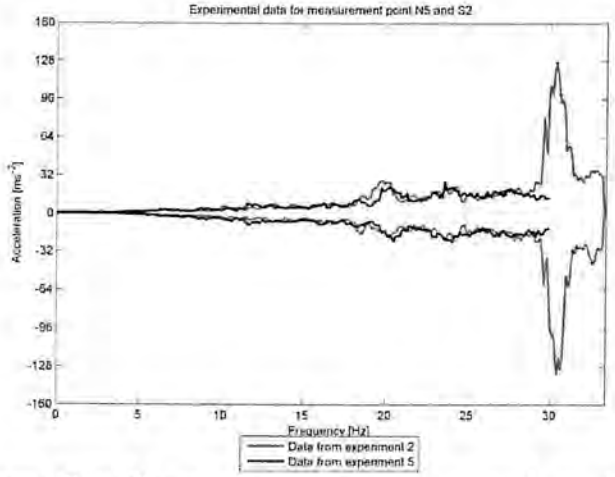

Figure G38: Comparison between measured accelerations for experiment two and five for measurement point N5 and S2.

G.4 - Comparison between experiment five and six

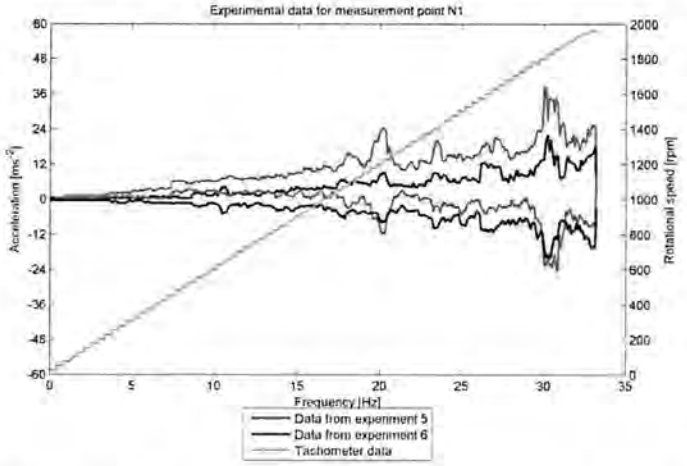

Figure G39: Comparison between measured accelerations for experiment five and six for measurement point N1.

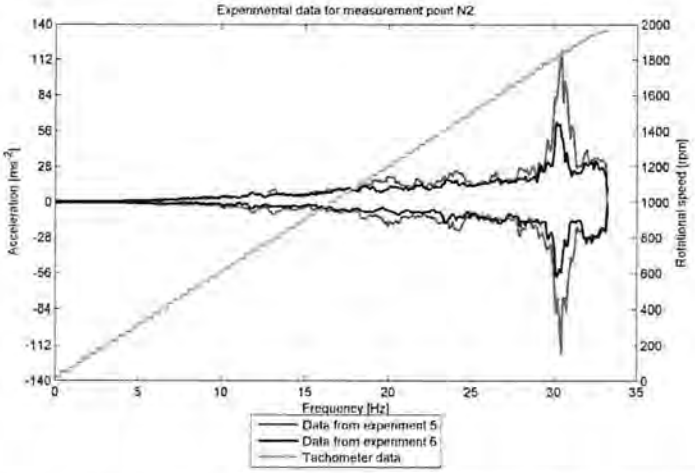

Figure G40: Comparison between measured accelerations for experiment five and six for measurement point N2.

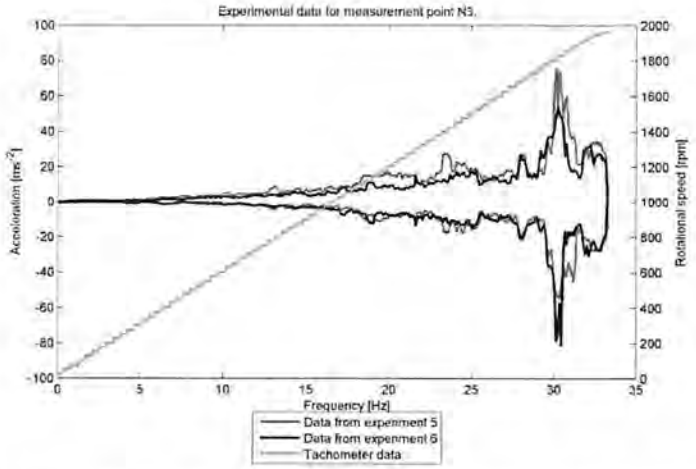

Figure G41: Comparison between measured accelerations for experiment five and six for measurement point N3.

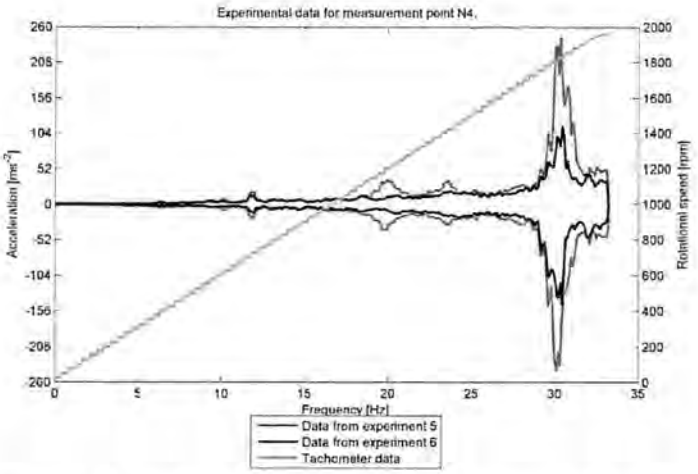

Figure G42: Comparison between measured accelerations for experiment five and six for measurement point N4.

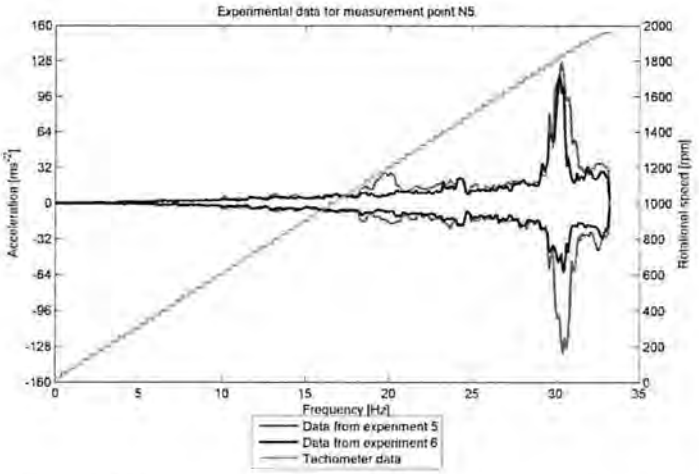

Figure G43: Comparison between measured accelerations for experiment five and six for measurement point N5.

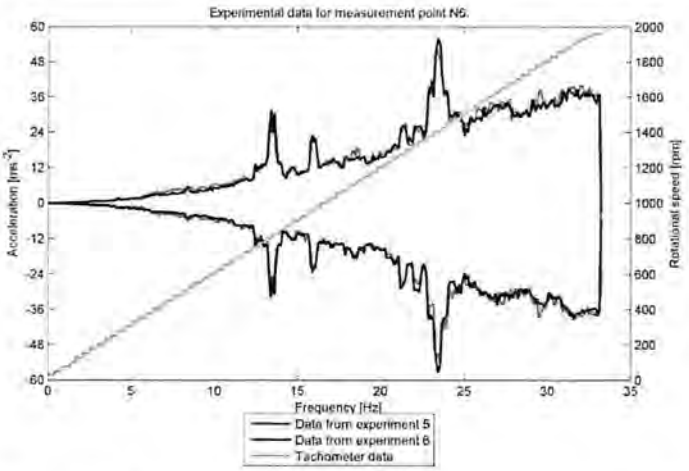

Figure G44: Comparison between measured accelerations for experiment five and six for measurement point N6.

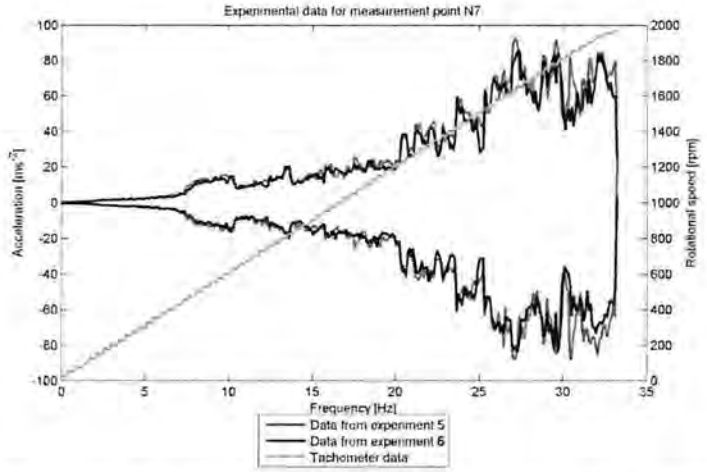

Figure G45: Comparison between measured accelerations for experiment five and six for measurement point N7.

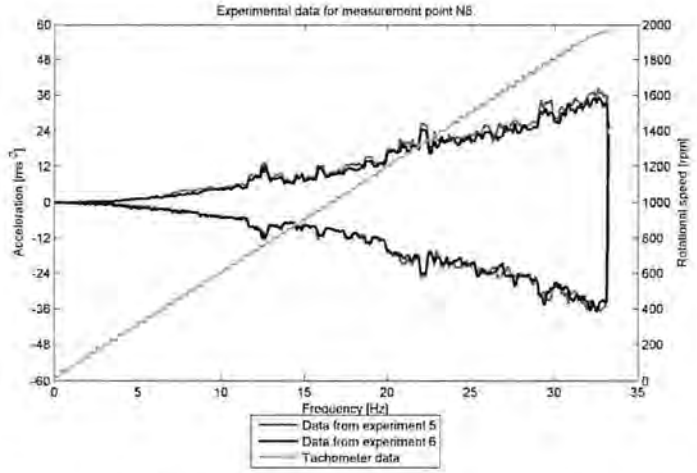

Figure G46: Comparison between measured accelerations for experiment five and six for measurement point N8.

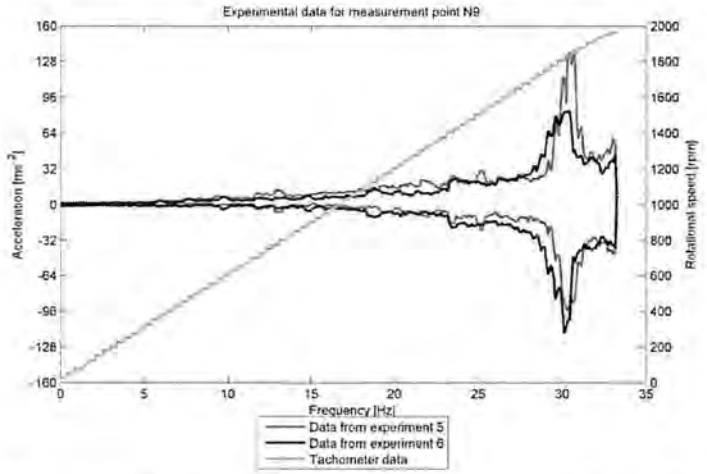

Figure G47: Comparison between measured accelerations for experiment five and six for measurement point N9.

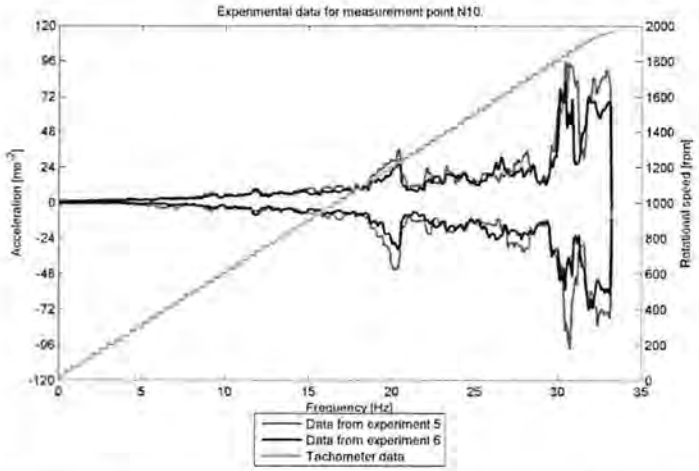

Figure G48: Comparison between measured accelerations for experiment five and six for measurement point N10.

G.5 - Comparison between experiment five and simulation

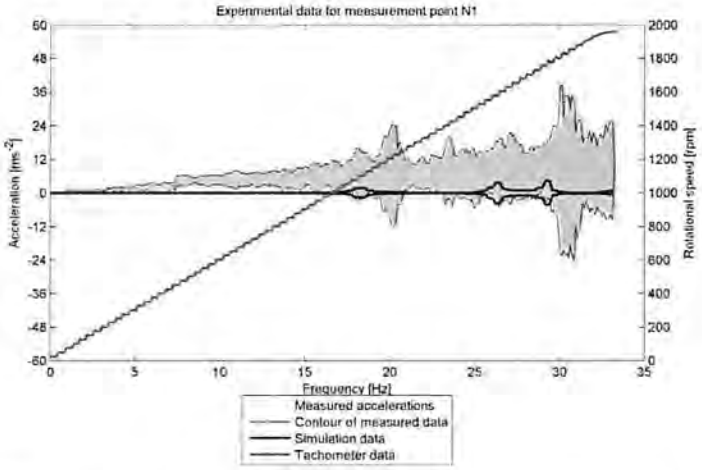

Figure G49: Comparison between measured acceleration for experiment five and simulation for measurement point N1.

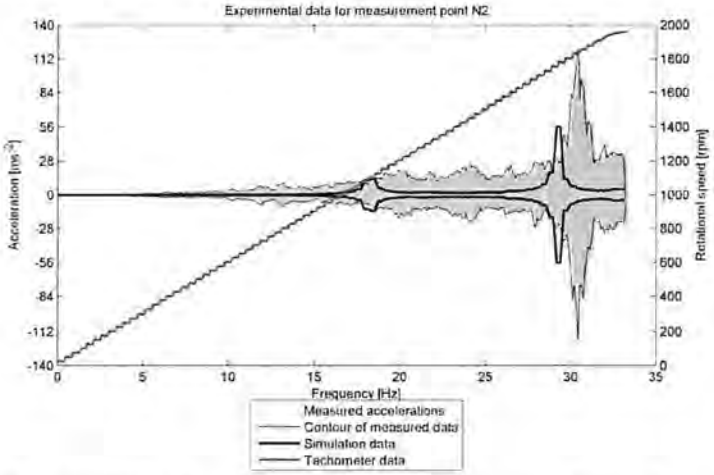

Figure G50: Comparison between measured acceleration for experiment five and simulation for measurement point N2.

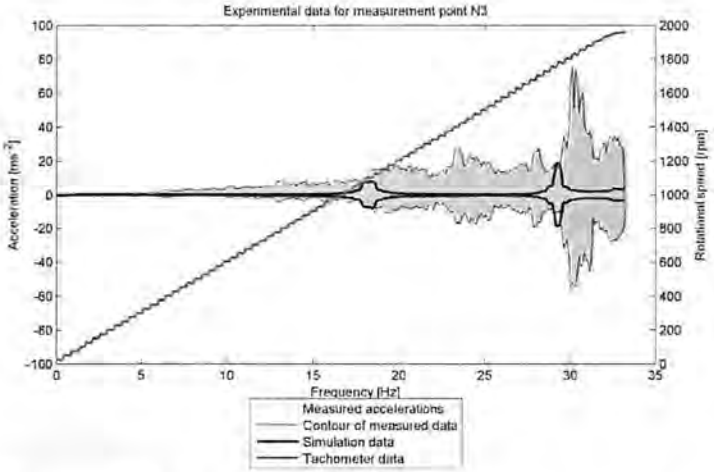

Figure G51: Comparison between measured acceleration for experiment five and simulation for measurement point N3.

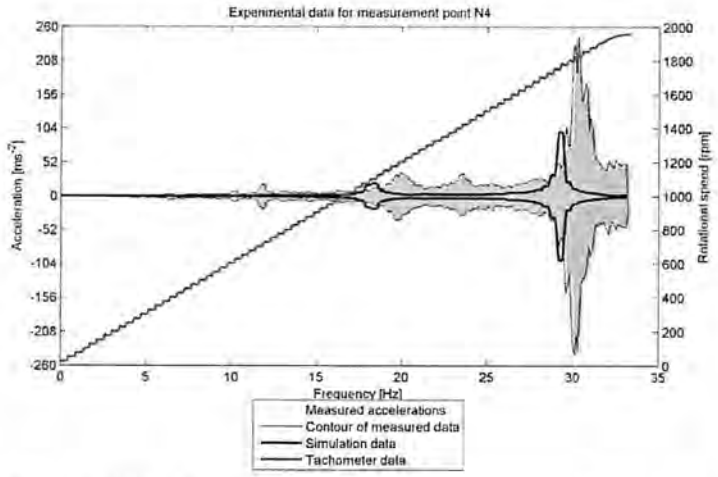

Figure G52: Comparison between measured acceleration for experiment five and simulation for measurement point N4.

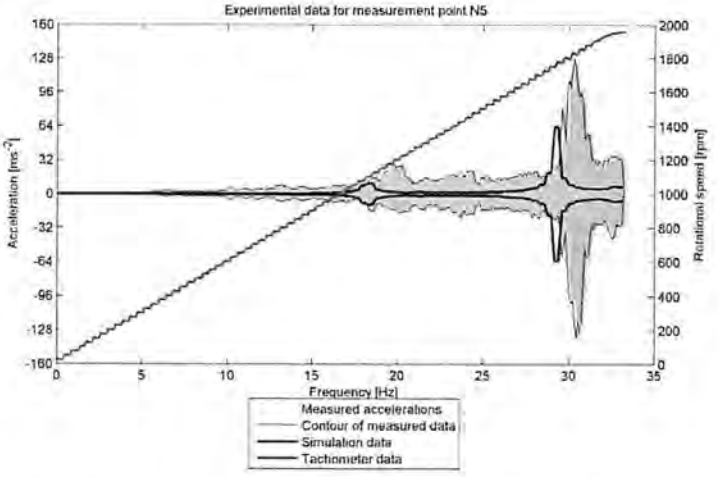

Figure G53: Comparison between measured acceleration for experiment five and simulation for measurement point N5.

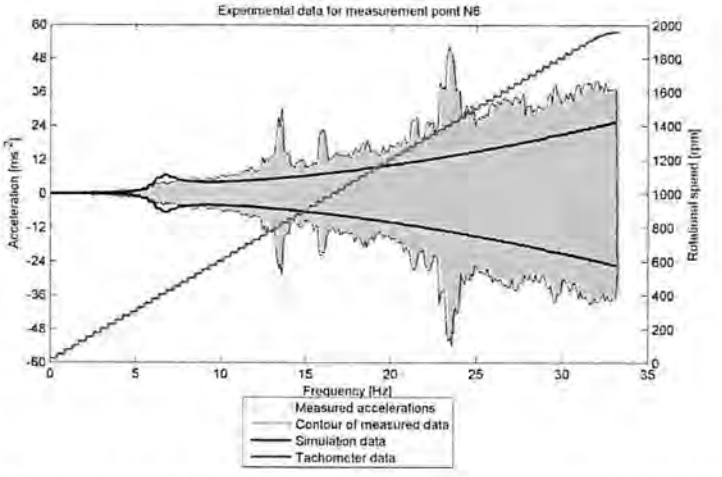

Figure G54: Comparison between measured acceleration for experiment five and simulation for measurement point N6.

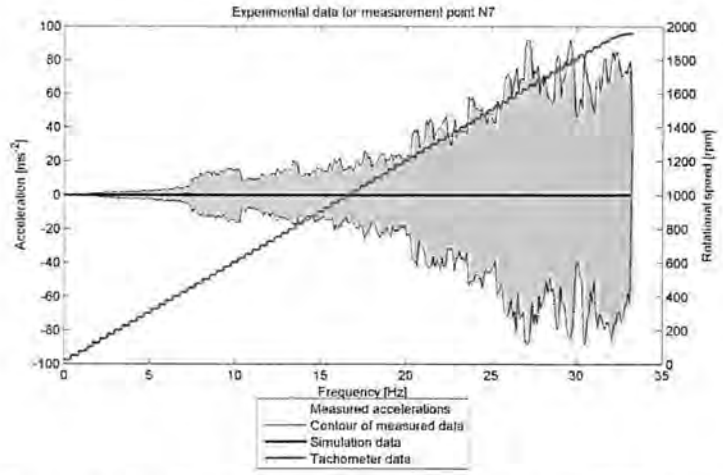

Figure G55: Comparison between measured acceleration for experiment five and simulation for measurement point N7.

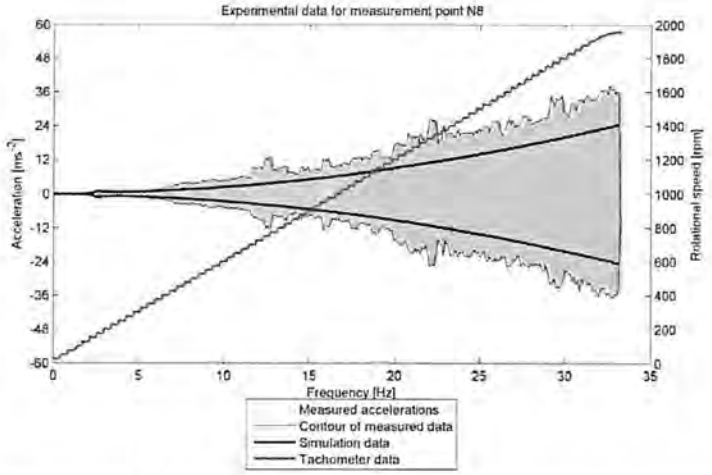

Figure G56: Comparison between measured acceleration for experiment five and simulation for measurement point N8.

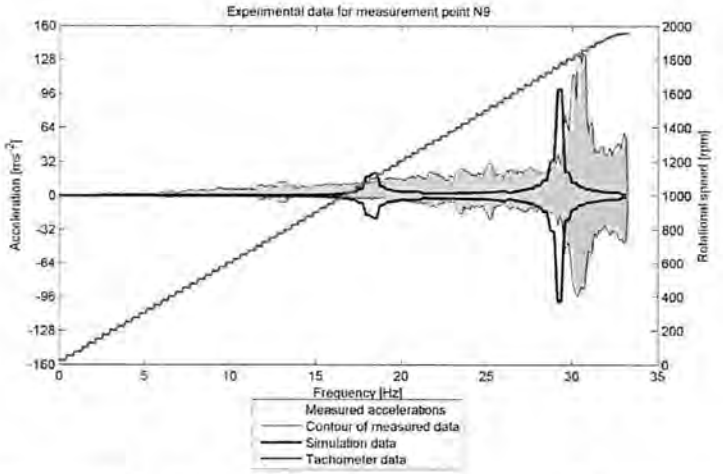

Figure G57: Comparison between measured acceleration for experiment five and simulation for measurement point N9.

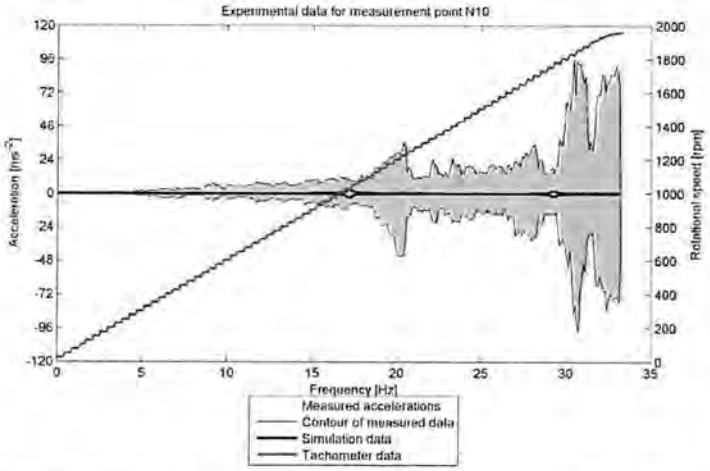

Figure G58: Comparison between measured acceleration for experiment five and simulation for measurement point N10.

G.6 - Comparison between experiment six and simulation

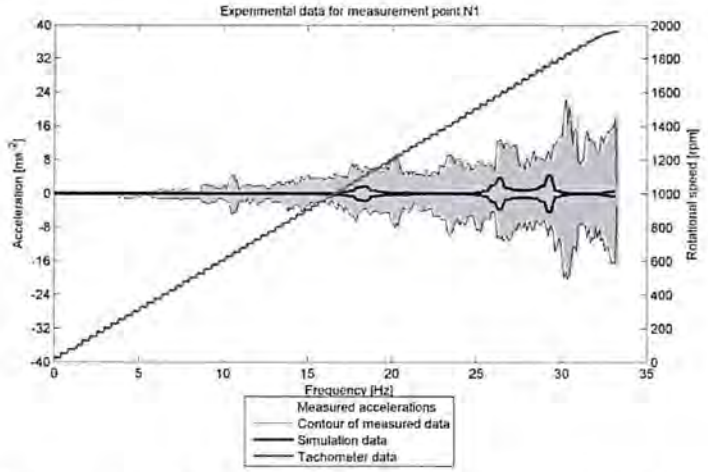

Figure G59: Comparison between measured acceleration for experiment six and simulation for measurement point N1.

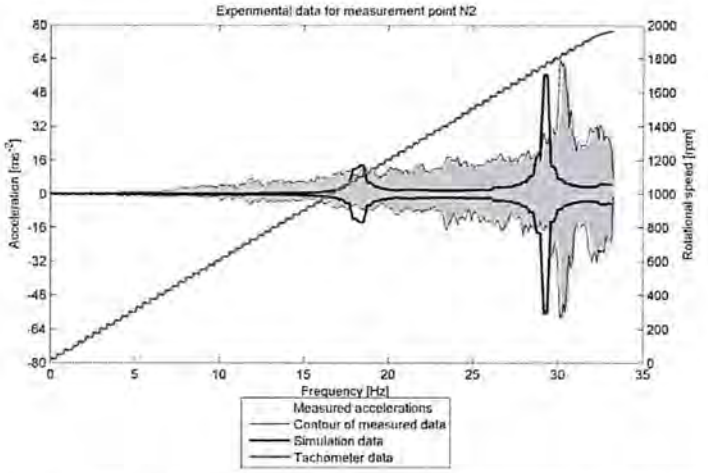

Figure G60: Comparison between measured acceleration for experiment six and simulation for measurement point N2.

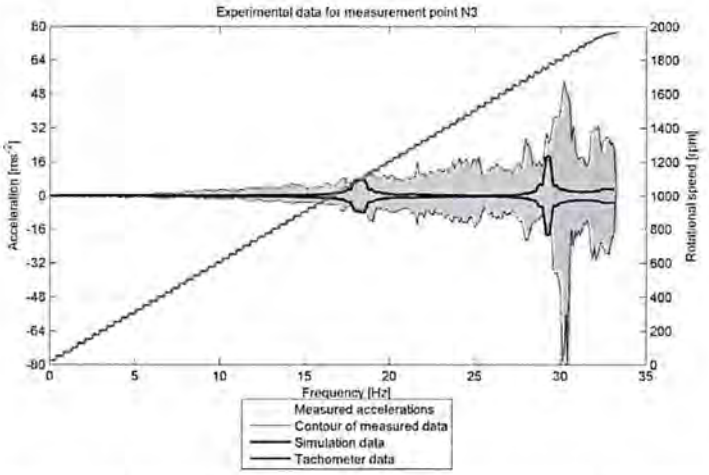

Figure G61: Comparison between measured acceleration for experiment six and simulation for measurement point N3.

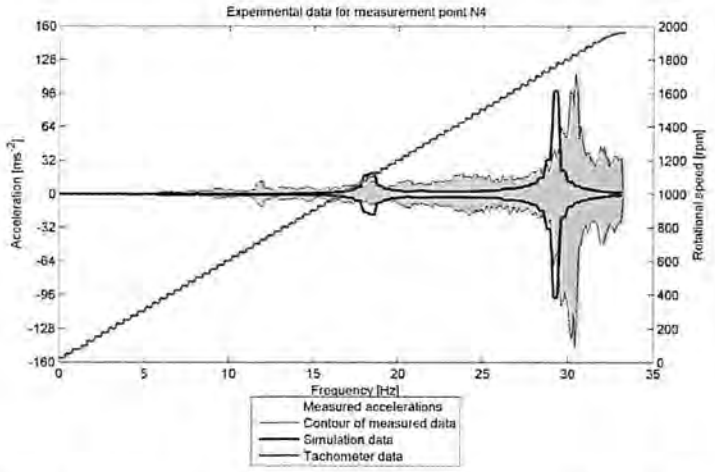

Figure G62: Comparison between measured acceleration for experiment six and simulation for measurement point N4.

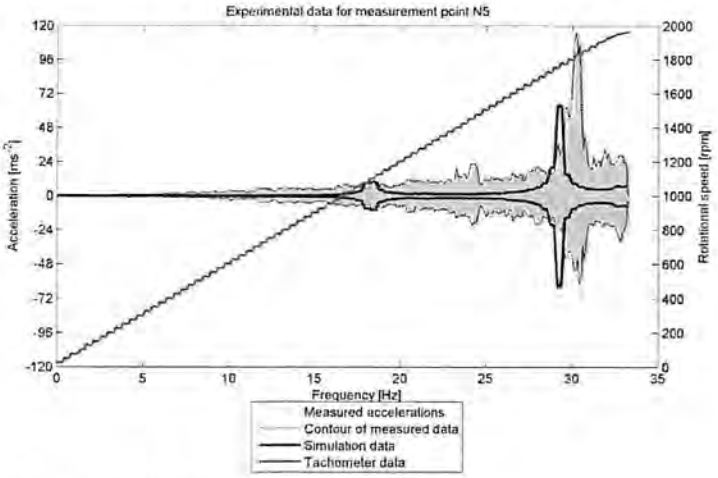

Figure G63: Comparison between measured acceleration for experiment six and simulation for measurement point N5.

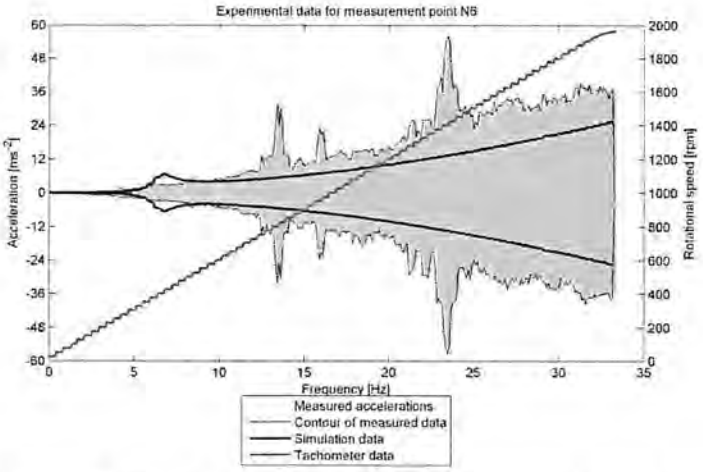

Figure G64: Comparison between measured acceleration for experiment six and simulation for measurement point N6.

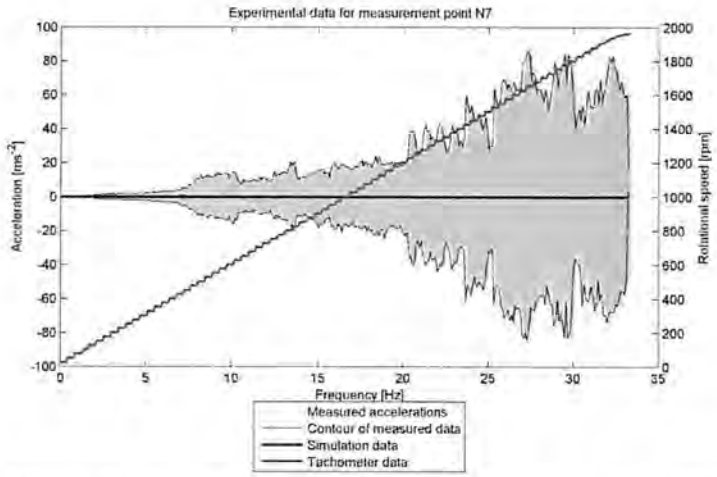

Figure G65: Comparison between measured acceleration for experiment six and simulation for measurement point N7.

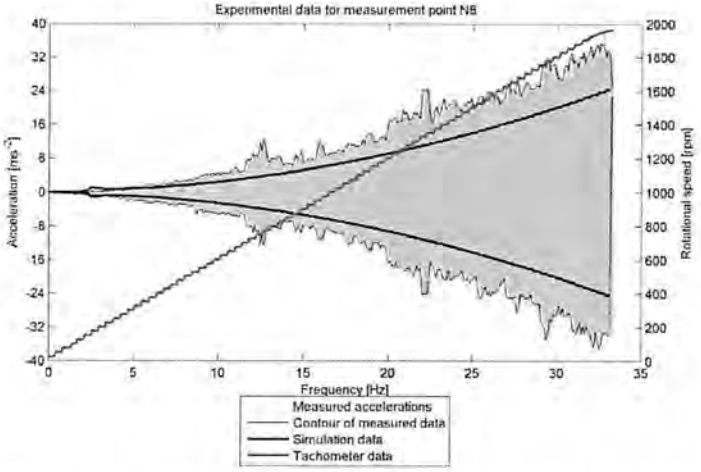

Figure G66: Comparison between measured acceleration for experiment six and simulation for measurement point N8.

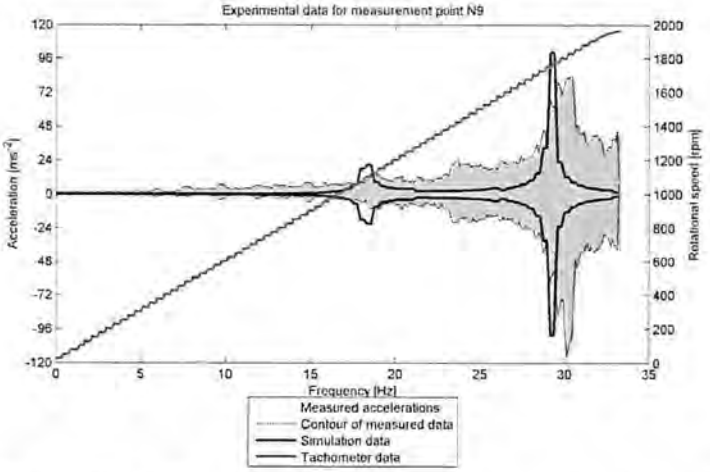

Figure G67: Comparison between measured acceleration for experiment six and simulation for measurement point N9.

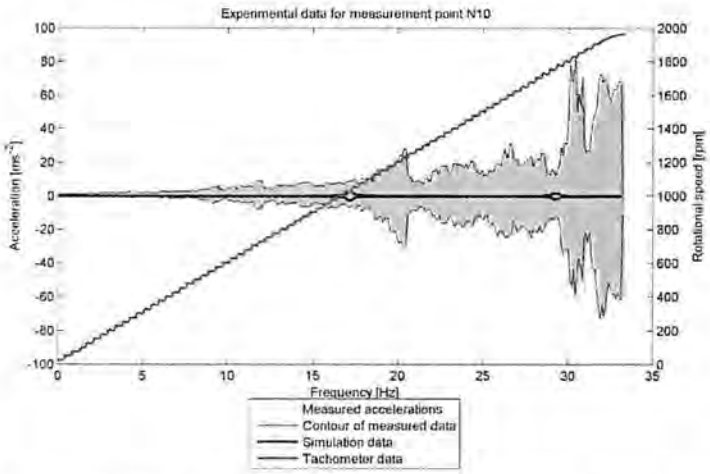

Figure G68: Comparison between measured acceleration for experiment six and simulation for measurement point N10.

Appendix H – Campbell diagrams

Here Campbell diagrams are presented for accelerations from experiment six and forces from experiment three, which acts as examples since the diagrams looks rather similar for all experiments.

H.1 – Acceleration

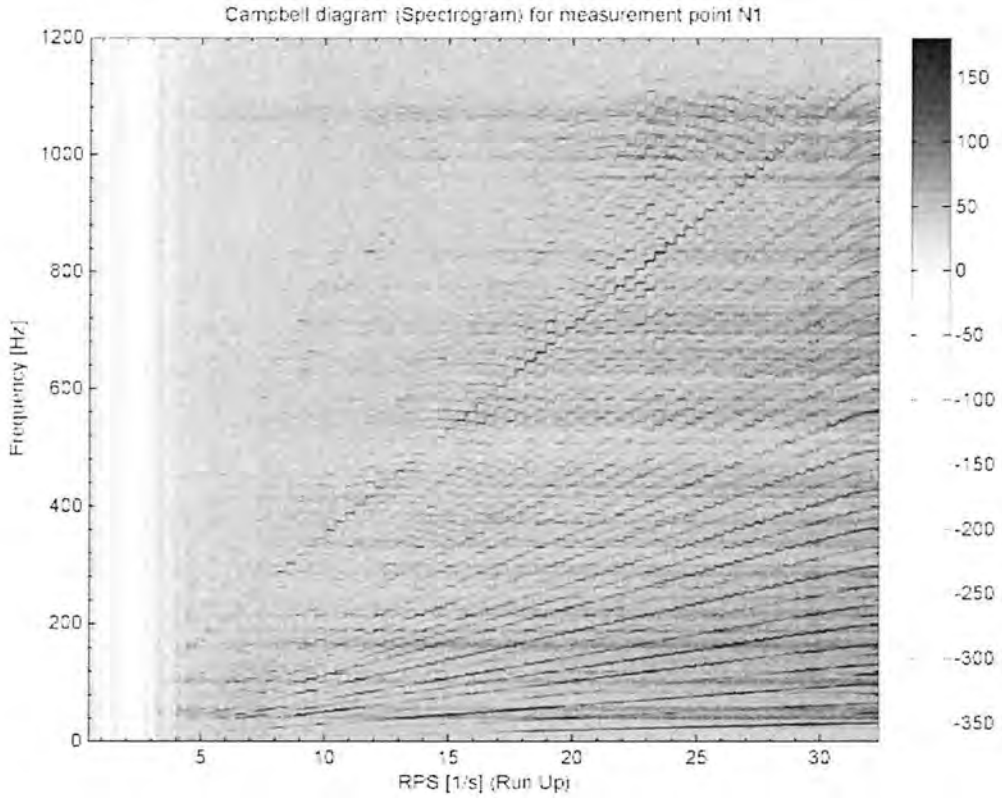

Figure H1: Campbell diagram for the acceleration signal in measurement point N1 for experiment six.

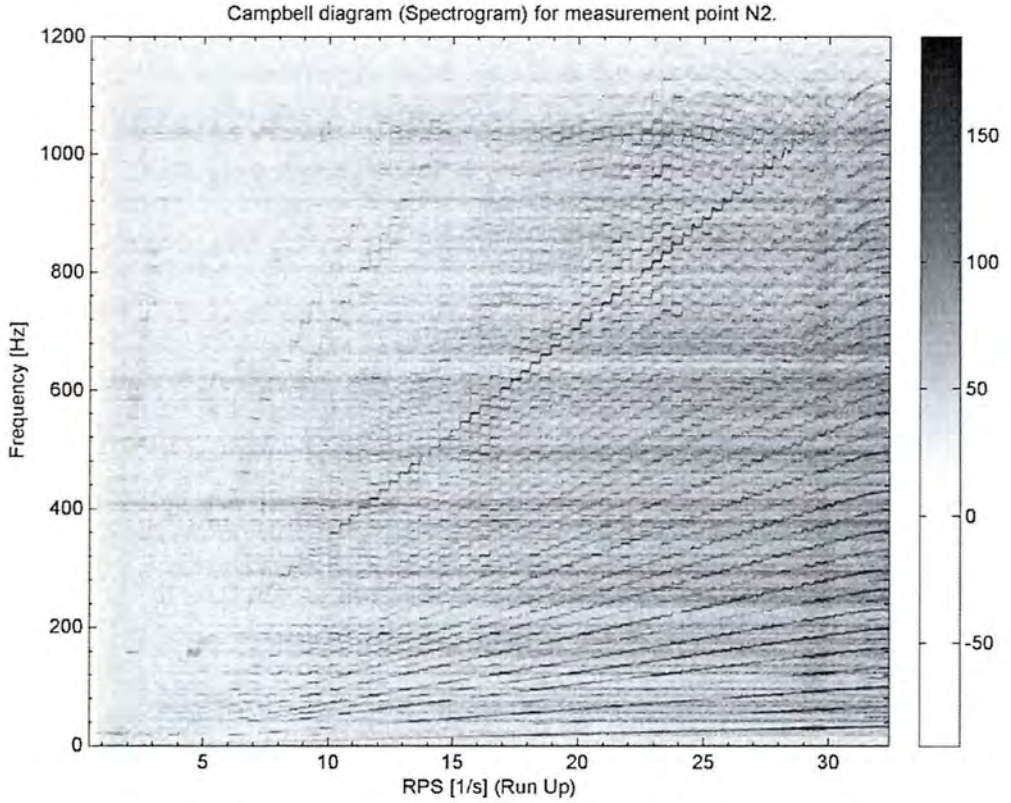

Figure H2: Campbell diagram for the acceleration signal in measurement point N2 for experiment six.

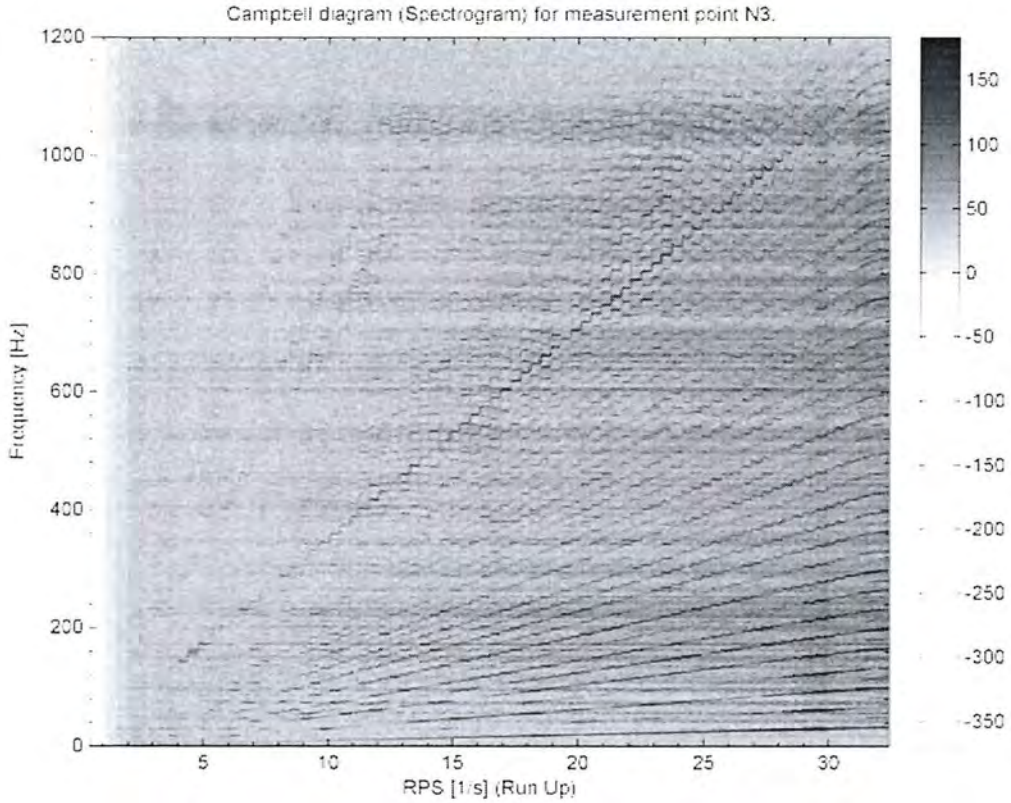

Figure H3: Campbell diagram for the acceleration signal in measurement point N3 for experiment six.

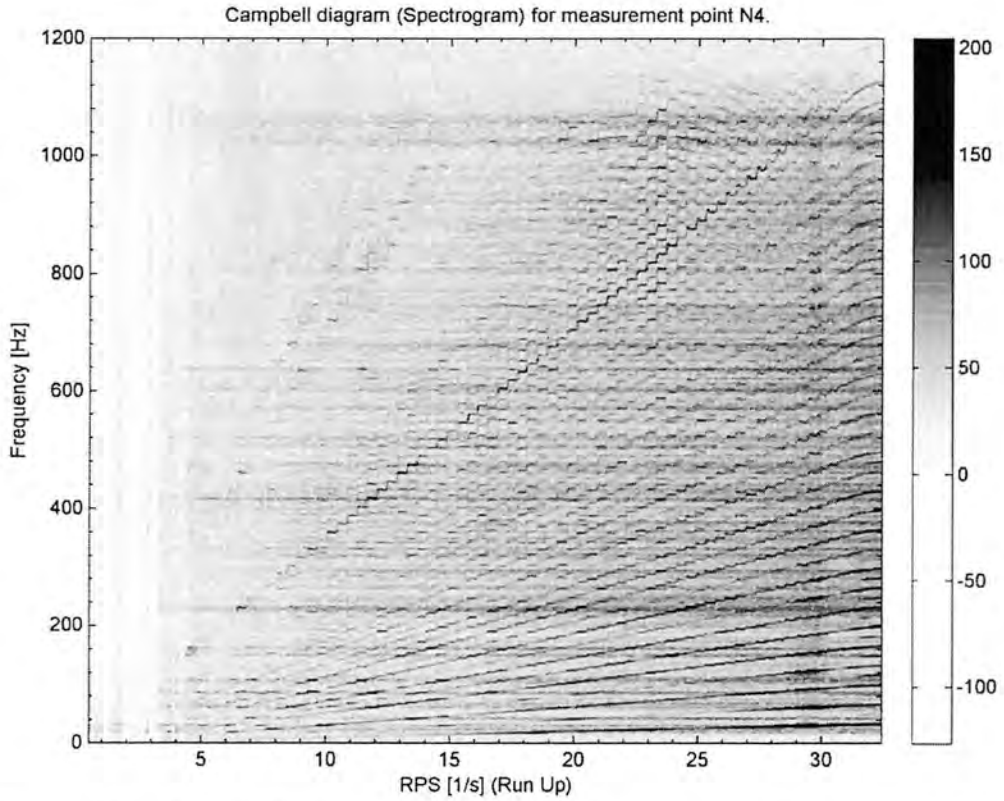

Figure H3: Campbell diagram for the acceleration signal in measurement point N4 for experiment six.

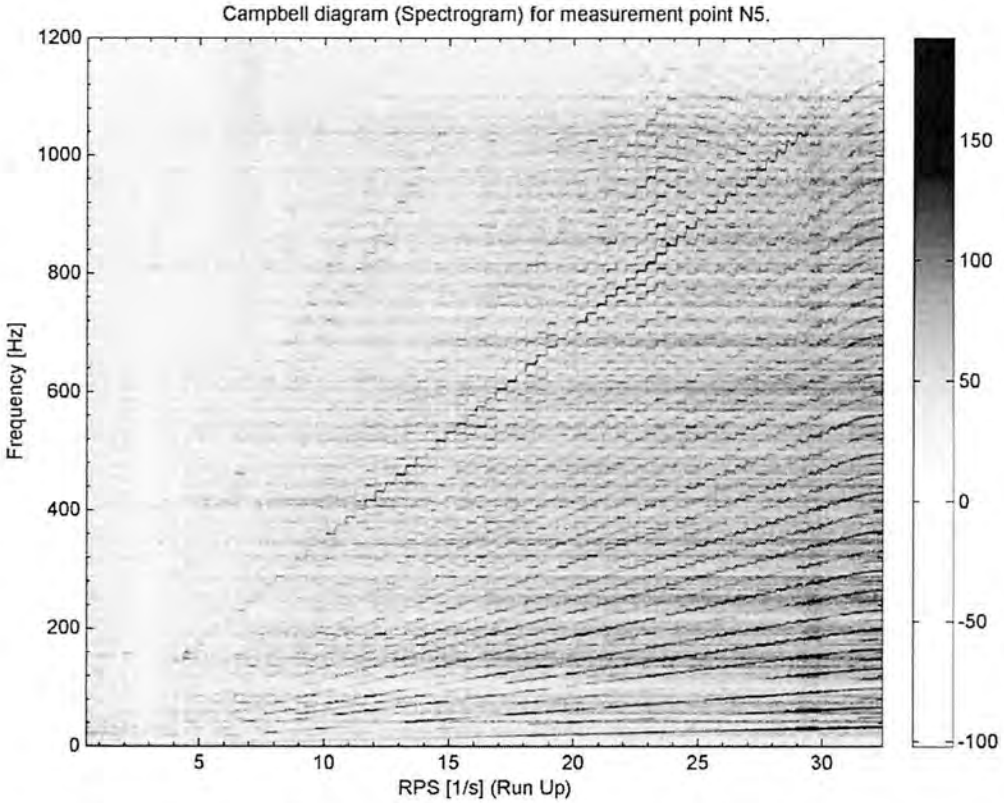

Figure H4: Campbell diagram for the acceleration signal in measurement point N5 for experiment six.

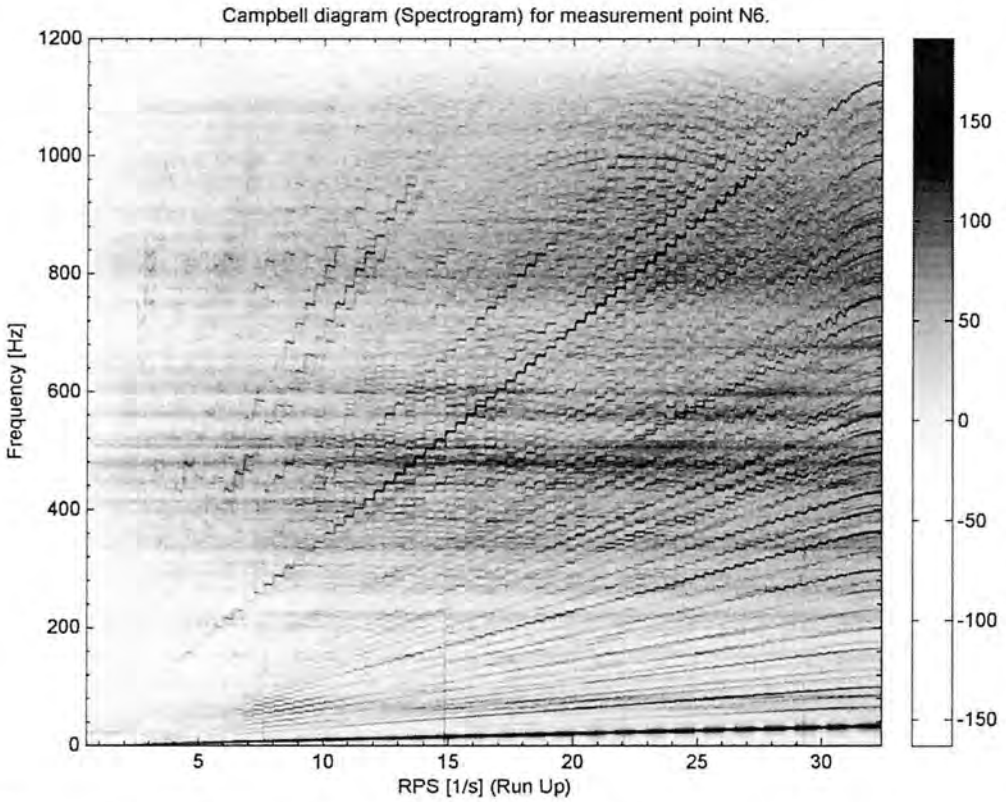

Figure H5: Campbell diagram for the acceleration signal in measurement point N6 for experiment six.

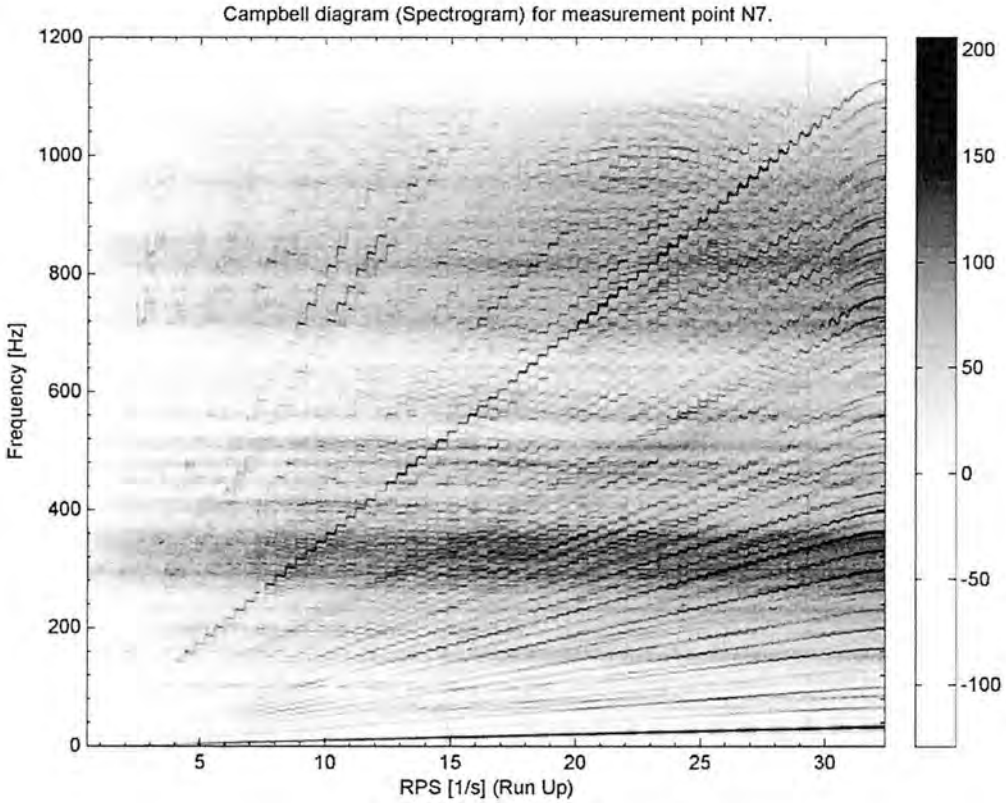

Figure H6: Campbell diagram for the acceleration signal in measurement point N7 for experiment six.

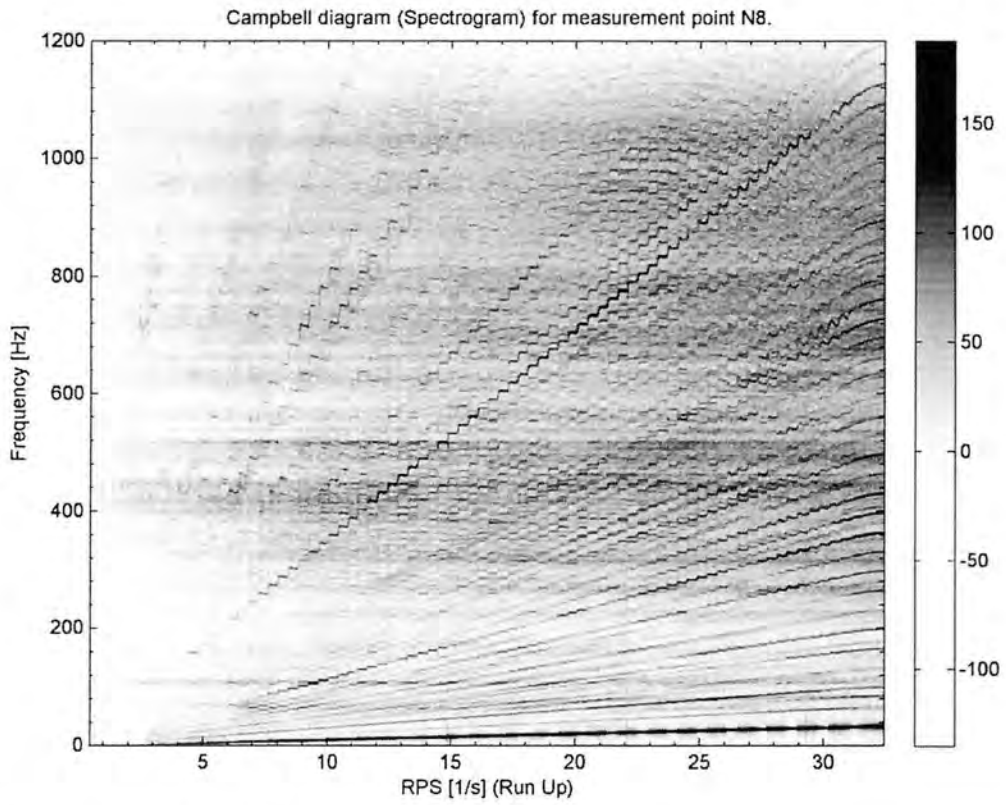

Figure H7: Campbell diagram for the acceleration signal in measurement point N8 for experiment six.

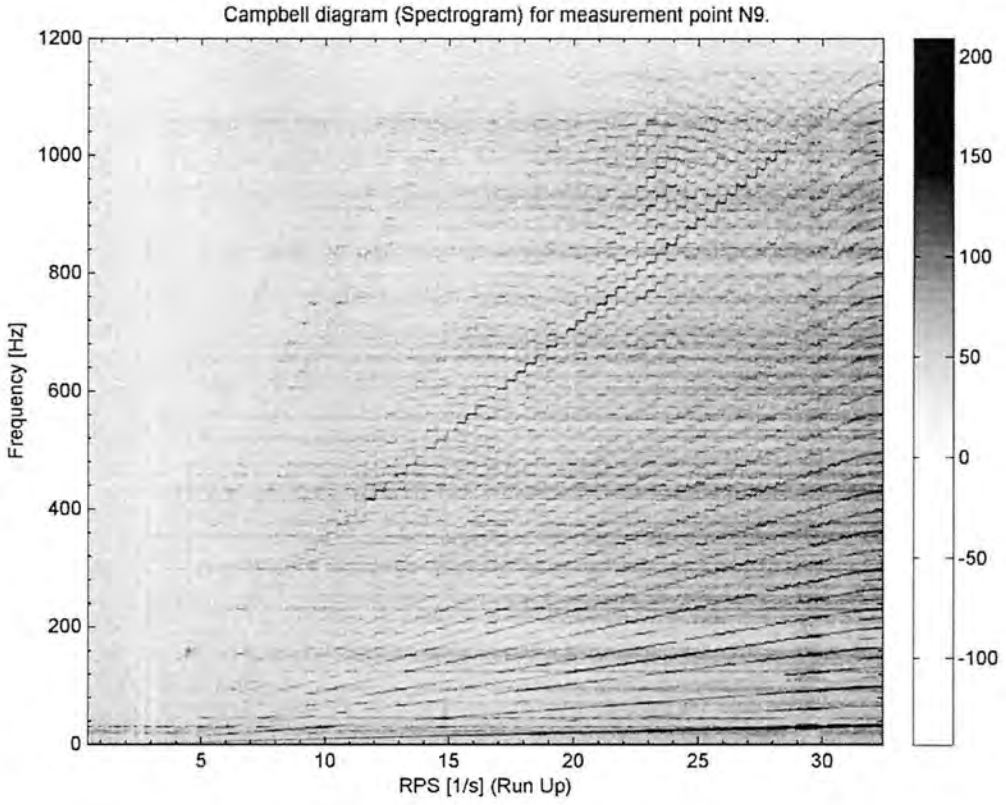

Figure H8: Campbell diagram for the acceleration signal in measurement point N9 for experiment six.

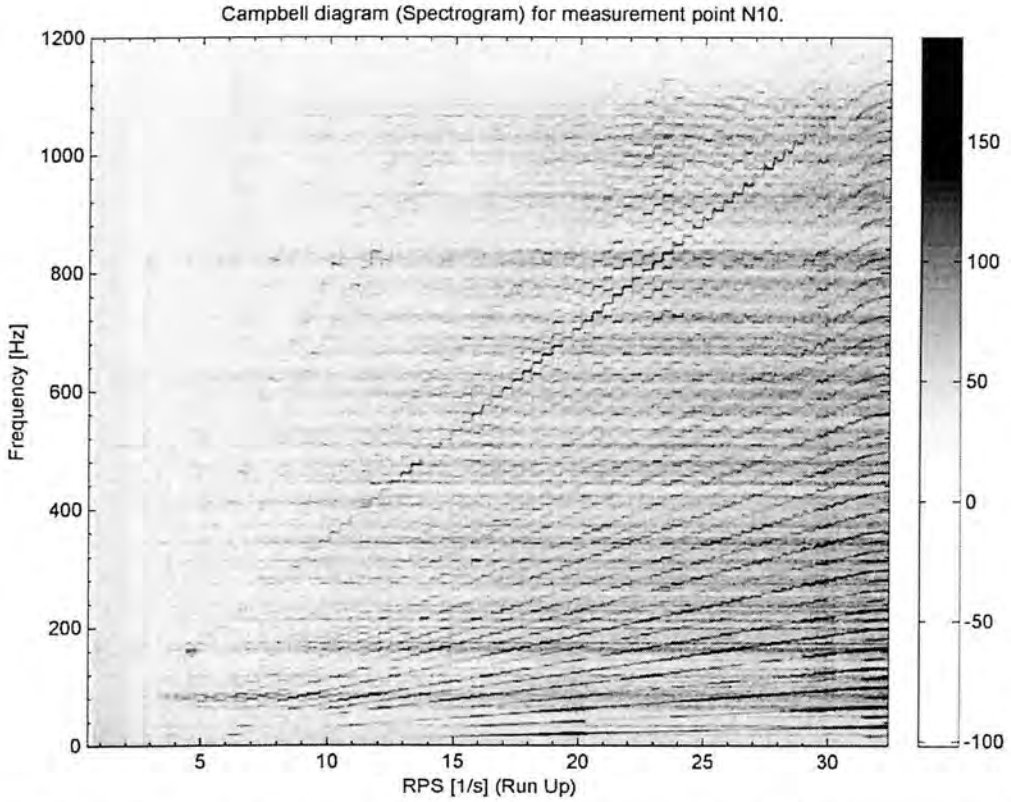

Figure H9: Campbell diagram for the acceleration signal in measurement point N10 for experiment six.

H.2 – Force

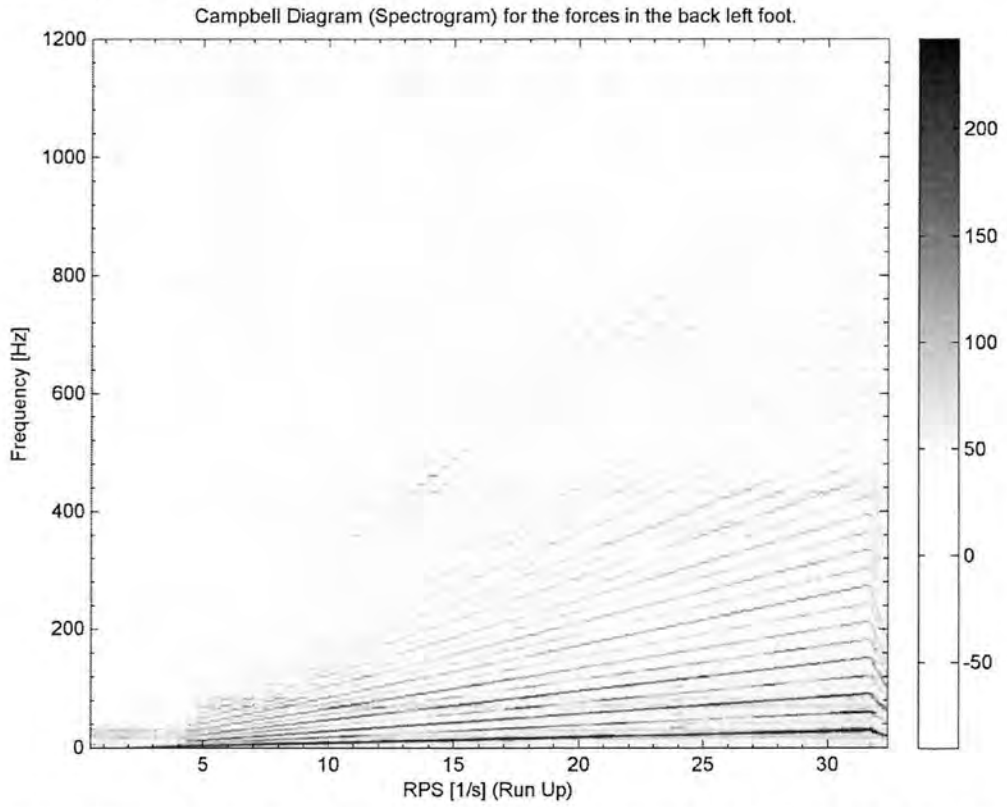

Figure H10: Campbell diagram for the force signal under the back left foot in experiment three.

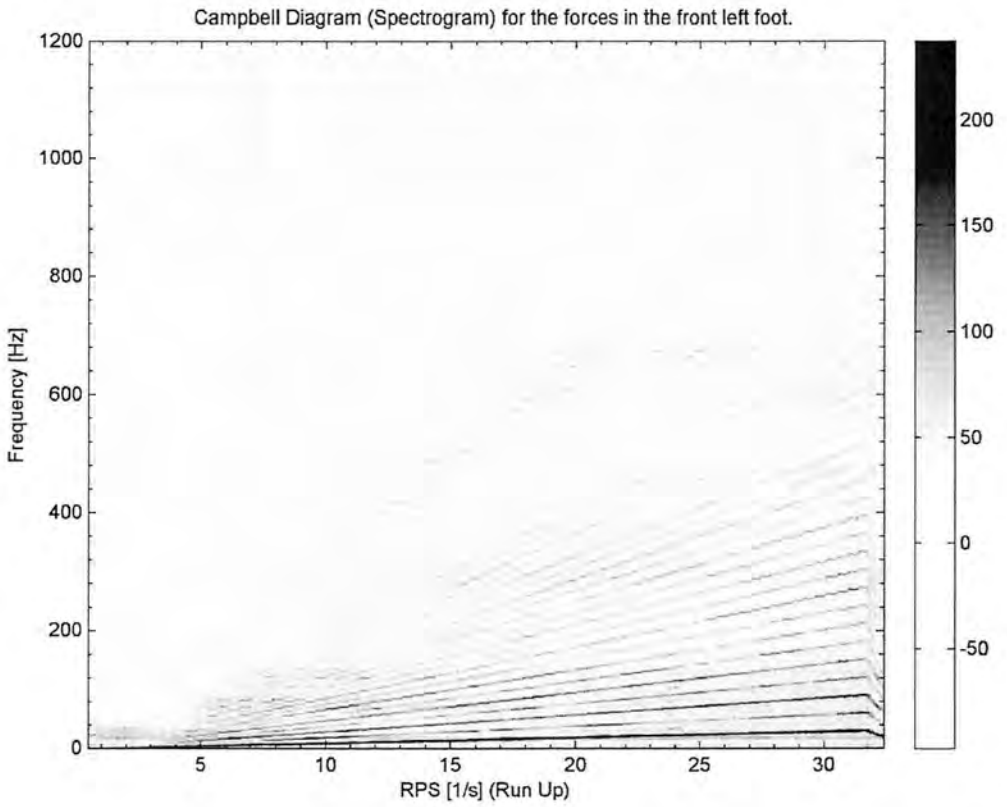

Figure H11: Campbell diagram for the force signal under the front left foot in experiment three.

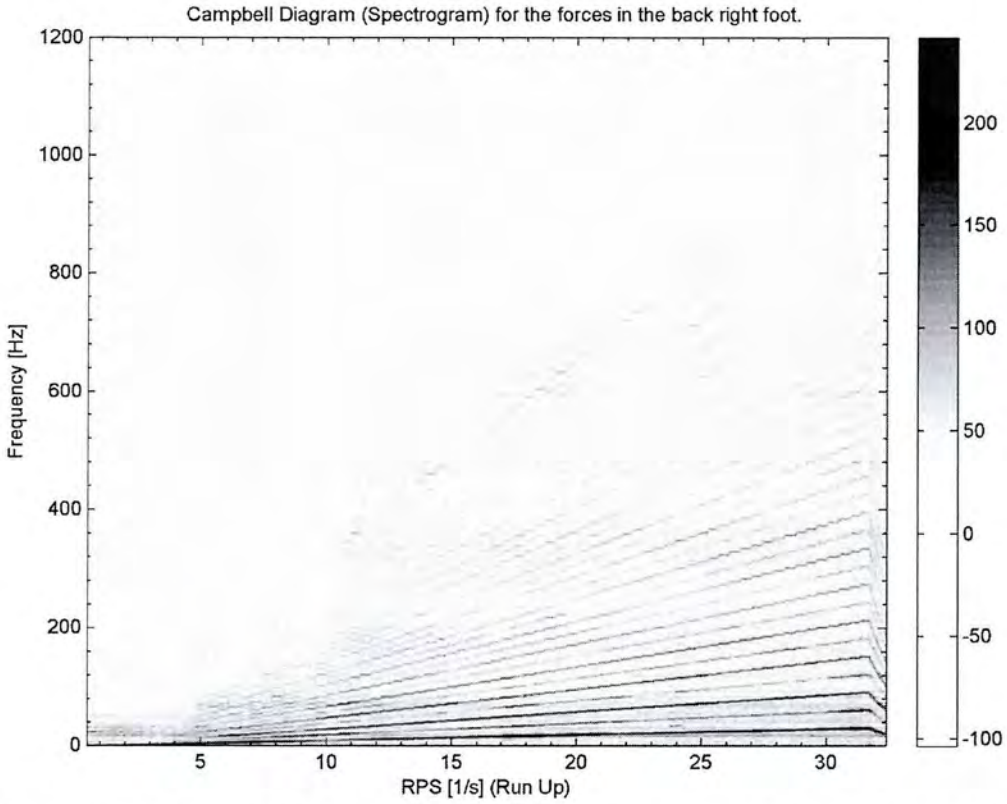

Figure H12: Campbell diagram for the force signal under the back right foot in experiment three.

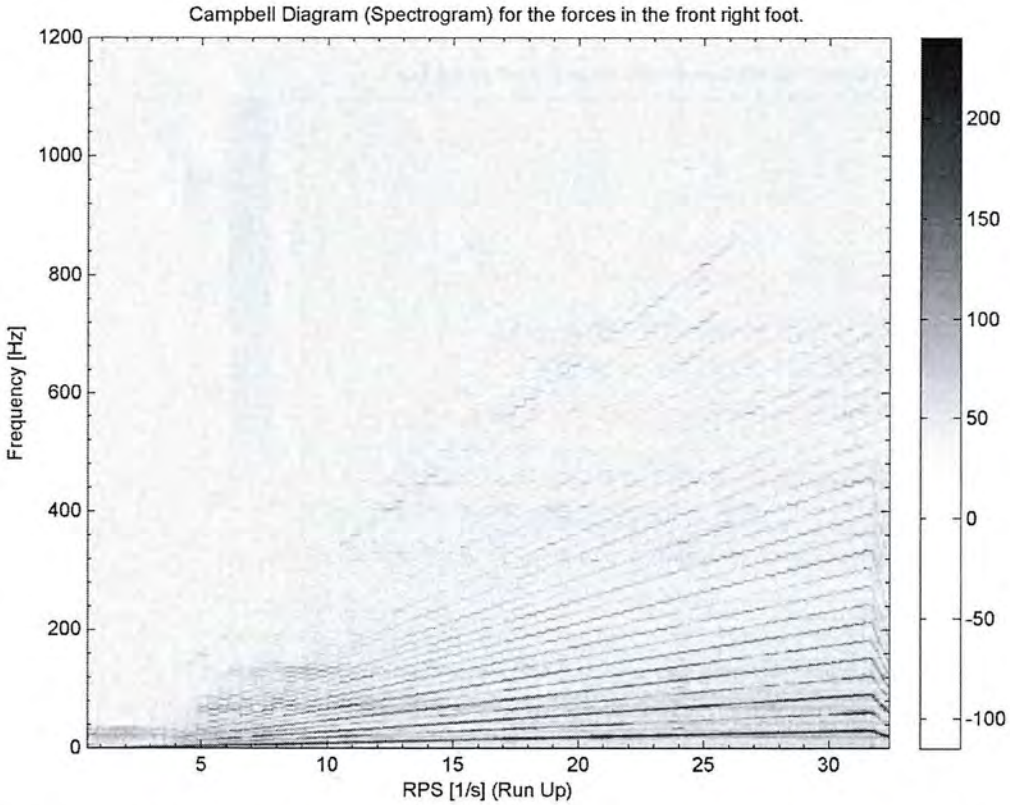

Figure H13: Campbell diagram for the force signal under the front right foot in experiment three.

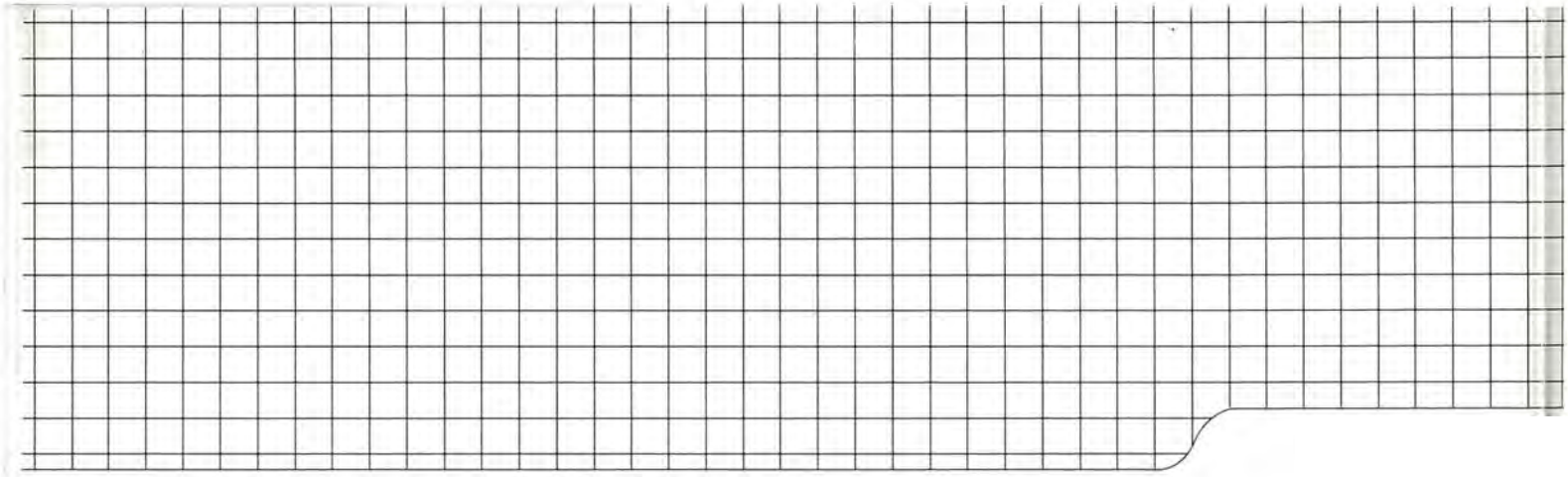

CHALMERS UNIVERSITY OF TECHNOLOGY
SE 412 96 Göteborg, Sweden
Phone: + 46 - (0)31 772 10 00
Web: www.chalmers.se